



David Novel

**Mechanical and physical  
characterization of graphene  
composites**







Doctoral School in Civil, Environmental and  
Mechanical Engineering

**Curriculum 3. Modelling and Simulations**  
**2019 - Doctoral Thesis**

David Novel

**Mechanical and physical characterization of  
graphene composites**

UNIVERSITY OF TRENTO



**Supervisors:**

Nicola Pugno, UNITN  
Giorgio Speranza, FBK

**Co-advisor:**

Maria Pantano, UNITN



Except where otherwise noted, contents on this book are licensed under a Creative  
Common Attribution - Non Commercial - No Derivatives  
4.0 International License

University of Trento  
Doctoral School in Civil, Environmental and Mechanical Engineering  
*<http://web.unitn.it/en/dricam>*  
Via Mesiano 77, I-38123 Trento  
Tel. +39 0461 282670 / 2611 - *[dicamphd@unitn.it](mailto:dicamphd@unitn.it)*

## Doctoral Thesis Summary

<b>1. Abstract .....</b>	<b>3</b>
<b>2. Microfibres .....</b>	<b>4</b>
<b>2.1. Electrospun composite fibres .....</b>	<b>4</b>
<b>2.2. Introduction .....</b>	<b>4</b>
<b>2.3. Materials .....</b>	<b>6</b>
2.3.1. Polymer composites preparation .....	6
2.3.2. Electrospinning and isolation of single fibres .....	7
2.3.3. Mechanical testing .....	8
2.3.4. Thermogravimetric analysis .....	8
<b>2.4. Mechanical tests .....</b>	<b>8</b>
<b>2.5. Morphological analysis .....</b>	<b>11</b>
<b>2.6. Toughening mechanisms and microcracking .....</b>	<b>13</b>
<b>2.7. Mechanical models .....</b>	<b>18</b>
<b>2.8. Comparison with straws .....</b>	<b>26</b>
<b>3. Composites from natural structures .....</b>	<b>31</b>
<b>3.1. Brief history of the modification on cellulose-based materials .....</b>	<b>31</b>
<b>3.2. Natural cellulose fibres &amp; functionalizations .....</b>	<b>32</b>
3.2.1. All-cellulose composites .....	36
3.2.2. Transparent cellulose paper .....	36
3.2.3. Transparency in wood .....	37
<b>3.3. Recent advancements on wood modifications .....</b>	<b>39</b>
3.3.1. Nanoparticles in wood and cellulose-based materials .....	42
<b>4. Nanoparticles in natural cellulose-based composites .....</b>	<b>44</b>

<b>4.1.</b>	<b>Materials .....</b>	<b>46</b>
<b>4.2.</b>	<b>Structural modifications .....</b>	<b>47</b>
<b>4.3.</b>	<b>Nanoparticles inside cellulose-based structures &amp; Chemical analysis.....</b>	<b>50</b>
<b>4.4.</b>	<b>Mechanical properties.....</b>	<b>54</b>
<b>4.5.</b>	<b>Burning, thermo-indentation and water absorption .....</b>	<b>61</b>
<b>5.</b>	<b>Wood transparency &amp; conductivity .....</b>	<b>66</b>
<b>5.1.</b>	<b>Materials .....</b>	<b>67</b>
<b>5.2.</b>	<b>Wood transparency .....</b>	<b>69</b>
5.2.1.	Bleaching and impregnation with polymers.....	69
<b>5.3.</b>	<b>Wood conductivity .....</b>	<b>70</b>
5.3.1.	Treatment of the internal structure & CNT vacuum impregnation .....	70
5.3.2.	Variation of conductivity during cyclic flexural testing....	74
<b>6.</b>	<b>Final Remarks .....</b>	<b>79</b>
<b>7.</b>	<b>Other PhD Projects.....</b>	<b>82</b>
<b>8.</b>	<b>Acknowledgements .....</b>	<b>83</b>
<b>9.</b>	<b>References .....</b>	<b>83</b>



## 1. Abstract

During my PhD activities, I studied the introduction of carbon-based nanofillers in materials at different scales, while focusing primarily on fibres and fibrillar materials. Several production techniques were exploited.

Little is known about the interaction of graphene with electrospun polymeric fibres. Manufacturing composite fibres is complex since fillers have lateral sizes nearing that of the embedding fibre. Indeed, graphene has a direct effect in both the assembly of the electrospun composite fibres and their mechanical performance. Moreover, the tensile behaviour of hollow micrometric electrospun fibres was compared with macroscopic hollow structures such as drinking straws. The acquired insights helped to explain the toughening mechanisms at the micro-scale and develop a model capable of predicting the stress-strain response of such structures.

Among natural materials, wood has the most relevant structural applications even at large scales. Its main structural component is cellulose that has a high resistance and a low light absorption. Several structural modifications of wood derived materials were recently investigated in order to enhance the mechanical and optical properties of cellulose. These enhancements can take place after the internal structure is chemically modified with the removal of lignin and after a structural densification. Potentially, any type of wood-like materials, such as giant reed (that is a fast-growing and invasive species), can be turned into a strong structural composite. Such modifications lead to an open and interconnected internal structure that is the ideal scaffold for nanoparticle intercalation. Graphene oxide and silicon carbide nanoparticles were intercalated into densified reed. They produced an even stiffer, stronger and tougher composite compared to the best up-to-date process available. Moreover, its capabilities to resist fire and water-absorption were tested.

Finally, the previous process was further developed on wood to achieve a combination of improved transparency and electrical conductivity. Graphene and carbon nanotubes were introduced into the structure of wood to foster conductivity and explore the viability of its application as a self-strain sensor.

## 2. Microfibres

### 2.1. Electrospun composite fibres

In this work, poly-vinylidene fluoride (PVDF) nanocomposite fibres filled with graphene (G) and graphene oxide (GO) were obtained by electrospinning. Single nanocomposite PVDF fibres were carefully isolated and characterized with a nanotensile machine. Results showed that, with the addition of 0.5 wt% of graphene oxide, Young's modulus and yield stress are improved and the specific toughness is higher than most polymeric fibres. The mechanical properties were analysed in light of the structure and peculiar morphologies of the nanocomposite fibres. The mechanisms of plastic deformation and energy dissipation are correlated to the characteristics of two different fillers: G and GO. A description of the toughening mechanisms involved is proposed, based on the observation of the morphological modification that occurred on fibres during the tensile testing. The structure of these fibres is also discussed in relation to their hollow nature, which holds an interesting comparison at a higher scale with experiments performed on plastic drinking straws. The analogy of the mechanical behaviour is reflected in the observed multiple necking propagation mechanism. Based on the experimental observations, a novel constitutive model is introduced to describe the performance of hollow PVDF fibres.

### 2.2. Introduction

Similarly to carbon nanotubes [1], graphene is a highly promising material in the field of polymer nano-composites due to its very high stiffness [2] and high aspect ratio. Graphene can potentially do on a nano-scale what carbon fibres do at micro-scale, i.e. improving the properties of the polymer matrices. Since the discovery of graphene [3], studies have flourished on the impact of graphene and graphene oxide (GO) on polymers and many of them focused on the mechanical properties of the composites [4-8]. Over the last few years, by extending the principles of short fibre composites to graphene fillers, graphene-polymer interactions have been studied in depth [9-12]. It was demonstrated that the optimal stress transfer is achieved if graphene flakes have controlled lateral dimensions. The critical size has been found to be around 4  $\mu\text{m}$  [10]: if the flakes are bigger, then the polymer

matrix, upon loading, will be able to transfer all the stress that graphene can withstand. If flakes are smaller, graphene still reinforces the polymer but not to its maximum extent. The production of very thin fibres presents a compromise from this point of view as we are investigating the smallest hierarchical level possible but aware that the maximum reinforcement cannot be achieved if composite fibres, and the flakes embedded, are too thin. Large graphene flakes cause a discontinuity in the fibre's morphology, leading to debonding and fibre opening, whereas large GO flakes remain embedded within the fibre. Moreover, Ramanathan et al. [13] reported that the oxygen functionalities of GO are beneficial in nanocomposites as they enhance the adhesion with polymers. Thus, mechanical properties can be improved dramatically even at very low loadings.

In most natural organisms, fibres and fibrils form the lowest hierarchical level and the most important structural block of their load-bearing units [14, 15]. By the electrospinning technique, fibres with diameters in the range  $100 \text{ nm} \div 10 \text{ }\mu\text{m}$  can be obtained [16]. Furthermore, electrospinning has already proven to be successful in the production of carbon nanotube based composites [17]. Isolation and direct mechanical tests of single electrospun fibres [18] opened a wide field for the investigation of very thin fibres. In fact, up to that moment, most studies on electrospun fibres had been limited to the mechanical testing of electrospun films, yarns and bundles [19] or to the extrapolation of mechanical properties from superficial nanoindentation of electrospun fibres [17, 20, 21].

The polymer chosen in this work for the preparation of the composite fibres is PVDF, a strong thermoplastic polymer and highly anhygroscopic. Therefore, the mechanical properties of PVDF are not significantly affected by changes in humidity as it happens for other polymers. Moreover, there are previous works analysing PVDF fibres which will be used as a comparison. These studies regard PVDF fibres [22] and PVDF+GO composites [23, 24].

In the present work, graphene-based PVDF composite hollow fibres were obtained by electrospinning. The mechanisms controlling their behaviour at large-deformations are discussed through an analogy with the mechanical behaviour of a macroscopic hollow structure represented by poly-propylene (PP) straws.

Hollow fibres are not new to research [25-27] and industry [28, 29]. For example, in this century they have started to be employed in swimwear (by four Japanese companies: Teijing, Unitika, Kanebo Gohsen and

Toyobo) because they are lightweight, thermally insulating and the lower apparent density provides a higher lift in water to professional swimmers. However, as it will be shown, there is still room to exploit the large-deformation capabilities and toughening mechanisms that these structures allow.

## 2.3. Materials

Graphene in powder form (Graphene Pure G+) was provided by Directa Plus (Lomazzo, Italy) whereas graphene oxide in water dispersion (4 mg/mL) was provided by Graphenea (San Sebastian, Spain). In order to find an appropriate oven treatment for the complete water removal of the GO water solution, a thermogravimetric analysis was performed. It was found that the weight loss starts to flatten at 83 °C since greatest part of the liquid has been removed. This temperature was then applied for 6 h in the oven at 400 mbar of pressure to remove all the water from the solution. The flakes measured under SEM had average lateral sizes of 0.87  $\mu\text{m}$  (G) and 1.18  $\mu\text{m}$  (GO) with maximum lateral sizes of 5.5  $\mu\text{m}$  (G) and 3.0  $\mu\text{m}$  (GO).

Poly-vinylidene-fluoride (PVDF) powder with a molar mass (MW) of about 534 kDa was supplied by Sigma Aldrich. Polyethylene oxide (PEO) powder with MW of about 34 kDa was supplied by Sigma Aldrich. N,N-dimethylformamide (DMF, from Merck, Purity > 99.5 %) and acetone (Sigma Aldrich, Purity > 99.5 %) were used as received.

### 2.3.1. Polymer composites preparation

Fillers were firstly dispersed in DMF to form stable dispersion [30]. A tip sonicator (Hielscher UP400S - H3 sonotrode) was used for sonication at 200 W under continuous duty cycle, cooled with an ice bath. The sonication time for graphene powder was 10 minutes, whereas GO was sonicated for 45 minutes as the starting material was a thin film resulting from drying in the oven. In a second stage, PVDF powder was added to these solutions to reach a concentration of 20 wt %, which was found to be optimal for the electrospinning process. They were sonicated and then brought to about 70 °C for 2 h, with the beaker in direct contact to the stirrer hot plate. When PVDF was completely dissolved into DMF, the solution was cooled down to room temperature and transferred to a stirred plate at room temperature. At this point acetone was added in a ratio 1:3 to the mass of DMF [31]. The purposes

of the second solvent are: i) to lower the solution viscosity, ii) to favour evaporation of the solvents during the fibres' spinning and iii) to limit the formation of beads [32]. The resulting solution was finally stirred for 30 minutes at room temperature. For both G and GO nanocomposites 0.5 wt% of filler was added.

### 2.3.2. Electrospinning and isolation of single fibres

The experimental apparatus consisted in a syringe pump (Harvard Apparatus 11 Plus) pushing the polymeric solution through a common 21G needle for hypodermic injections. It was previously machined with a bench grinder to remove the bevel and polished afterwards. This metallic needle was charged by a high voltage power supply (Spellman SL 30) to keep a constant potential difference between needle tip and a target. The target used for the fibres' collection was built in copper with a proper shape (Fig. 1a) to promote fibres' alignment, which is fundamental for the isolation of single fibres [18]. The initial trials to optimize the target geometry (Fig. 1a; Fig. 1b) were done with PEO [18], an easy to spin polymer, using a 6 wt% PEO in water solution that was stirred for 2 h at 50 °C before spinning. Optimization of electrospinning parameters lead to set: i) distance between needle and target of 30 cm, ii) applied voltage of 19.0 kV and iii) feed rate of 1.0 ml/h. For each experiment the electrospinning apparatus, with related syringe flow and electric field, was stopped after a couple of seconds. The density of the deposited fibres was lower in the lateral regions of the target (Fig. 1b), where it is possible to isolate even a single electrospun fibre by removing the excessive material with tweezers. Each fibre was collected on a different cardboard frame (Fig. 1c) with bi-adhesive tape on two sides, they were glued in place with a cyanoacrylic adhesive. The fibres were kept free standing with a gage length of 1 cm for testing with the nanotensile machine.

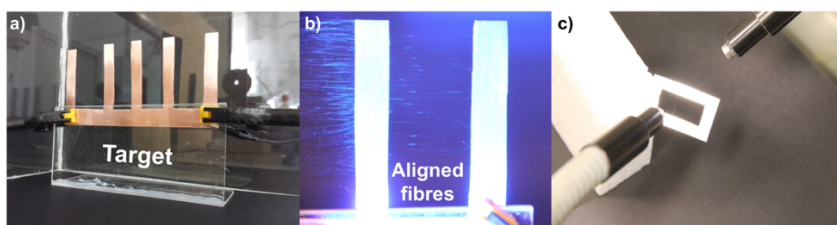


*Fig. 1 - a) Copper target for the electrospinning setup; b) Detail of the target. The most lateral region is on the right and it showed a lower number of aligned fibres collected; c) single fibre on cardboard support frame*

### 2.3.3. Mechanical testing

Tensile tests on electrospun fibres were made with a nanotensile machine T150 UTM (Agilent) equipped with a 500 mN load cell with a resolution of 50 nN. Each tensile test was carried out at room temperature with a strain rate of  $0.3 \text{ \%s}^{-1}$ . Five mechanical tests were carried out for each set of fibres. Experimental points were acquired with the software Agilent Nanosuite 6.2 Professional. Stress-strain curves were derived considering a full cross section for the fibres and the external diameters were measured with optical microscope and electron scanning microscope (SEM).

Tensile tests on PP straws were made with MIDI testing machine equipped with a load cell of 200 N. Each test was carried out at room temperature and mechanical properties were measured according to standard D638 - 02a [33]. They were performed at same strain rate ( $0.3 \text{ \%s}^{-1}$ ) of electrospun fibres. In addition, polypropylene straws were also tested at lower and higher strain rates ( $0.1 \text{ \%s}^{-1}$ ,  $1 \text{ \%s}^{-1}$  and  $3 \text{ \%s}^{-1}$ ) both in the cylindrical form and after they were longitudinally cut along the axis. The grip for testing of cylindrical straws was achieved by proving an internal support in the form of steel cylinders having the same diameters of the straw. The two cylinders were positioned one in each of the two grip regions and their extension was limited to the clamping contact length. Externally the straws were surrounded by a reinforced adhesive gasket to prevent premature clamping failures and tightly clamped. Stress-strain curves were derived considering the real cross section of the straws.

### 2.3.4. Thermogravimetric analysis

Thermogravimetric analysis (TGA) was performed by a Q5000 device by TA Instruments (New Castle, DE, United States of America) in platinum sample holders of 100  $\mu\text{L}$ ) under an air flow of 25 mL/min with and a heating rate of  $1 \text{ }^\circ\text{C}/\text{min}$ .

## 2.4. Mechanical tests

Three sets of electrospun fibres were produced. The first was a reference sample of neat PVDF fibres. The second and third were made of the same polymer and loaded with graphene (PVDF+G) and graphene oxide (PVDF+GO) respectively. Both had a filler content of 0.5 wt%, a concentration previously studied by Rahman et al. [24] who analysed the electrical properties of PVDF+GO nanocomposites. The

obtained stress-strain curves are reported in blue, black and red in Fig. 2, where a representative specimen for each sample is shown.

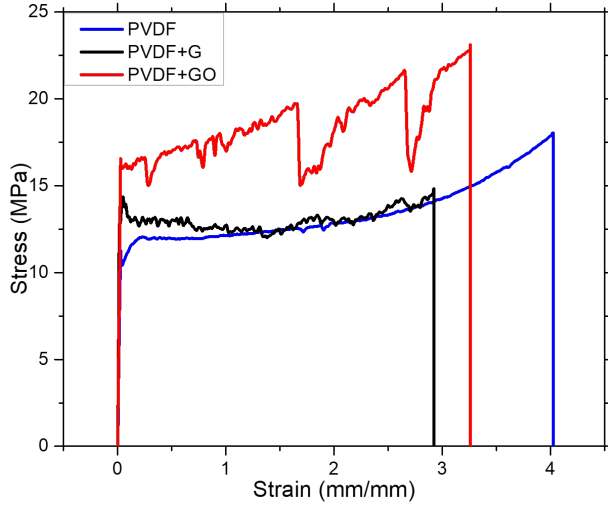


*Fig. 2 - Stress-strain curves up to failure for PVDF, PVDF+G, PVDF+GO fibres*

The main parameters obtained from the tensile test are summarized in Table 1 with standard deviation error bars showing the dispersion of the data. The values of specific toughness (J/g) in Table 1 were calculated with Equation 1 where the density of PVDF  $\rho$  is 1.74 g/cm<sup>3</sup> (source: the producer, Sigma Aldrich).

$$\text{Specific toughness} = \frac{\int_0^{\epsilon_B} \sigma \, d\epsilon}{\rho}$$

*Equation 1 - specific toughness*

The shape of the stress-strain curves shows an inclined plateau after yielding and is then followed by the strain-hardening at large deformations. The first plateau is linked to the plastic irreversible stretching and unfolding of the amorphous domains in the polymer [34]. Stiffening instead occurs when the load starts to be transferred to the crystalline domains and the covalent bonds of the polymeric backbone chains are stretched [35].

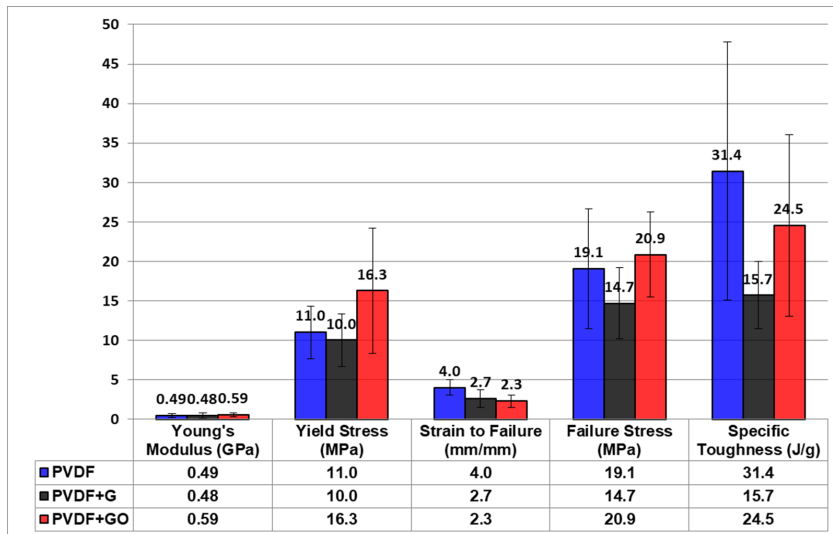


*Table 1 - Average values with standard deviation error bars*

The scatter has to be accounted for as an intrinsic factor of the electrospinning technique and defects play a critical role in the electrospun fibres. The results show that the addition of graphene (G, in black) reduces the average values of all the mechanical properties with respect to the reference PVDF fibres. The only exception is an unchanged Young's modulus. On the other hand, the addition of GO (curves in red) increased the average Young's modulus and failure strength with respect to PVDF reference, while there is a drop in the strain at break and a decrease in toughness.

It is worthwhile to note that the addition of GO causes a remarkable increment (by a factor of 1.5) of the yield stress. A similar behaviour was observed in PVDF films filled with GO as reported by El Achaby et al. [23]. This could be related with the improved interfacial adhesion between the polymer and GO that was reported for bulk composites [13]. Further insights will be analysed in the morphological section ahead.

The addition of GO diminished the average toughness modulus, the values are higher than PVDF+G but slightly lower than those of the PVDF reference. The highest recorded toughness modulus was 59 J/g for pure PVDF, which is close to the 78 J/g of Kevlar 49 fibres [36].

The graphs in Fig. 3 show a comparison of the properties of the fibres produced in literature data for the same materials: PVDF and



PVDF+GO. The superior properties obtained in terms of strain at break and toughness modulus, while having a lower failure stresses, might be an indication of a hollow nature of the fibres, which will be later analysed.

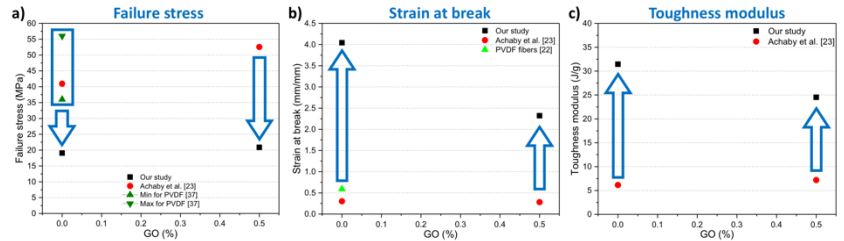


*Fig. 3 - Mechanical properties of PVDF and PVDF+GO nanocomposite fibres compared to the literature [22, 23, 37] a) Failure stress b) Strain at break c) Toughness modulus*

## 2.5. Morphological analysis

After the introduction of G flakes, all the mechanical properties decreased. Instead, GO shows more improvements in terms of yield stress, failure stress and toughness modulus. A possible explanation for the different behaviours of G and GO flakes inside PVDF fibres can be understood by observing the SEM images in Fig. 4a,b and 5).

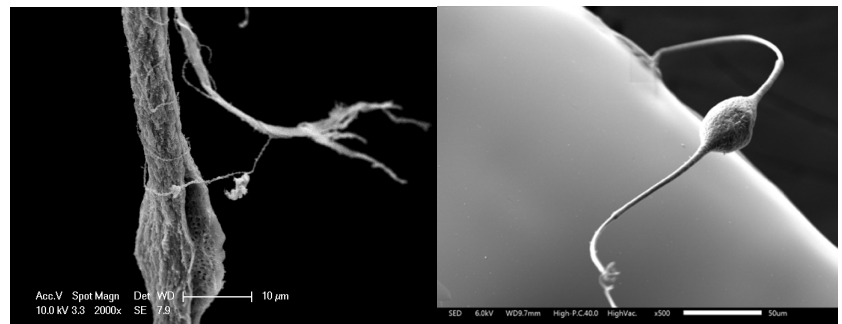


*Fig. 4 - a) morphology of the fibre with G flakes and b) with GO flakes*

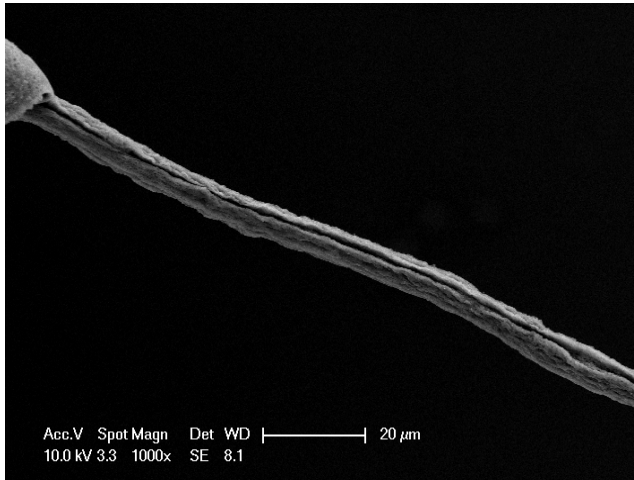


*Fig. 5 - Fibre opening induced by G flakes - PVDF+G fibre*

G flakes (Fig. 4a) tend to act as a discontinuity since they are not fully embedded into the fibre and this leads to a fibre opening, which is extended along the fibre (Fig. 5). This phenomenon is certainly reducing the resistant cross-section of the fibres. Conversely, GO flakes are well encapsulated into the continuous fibre, although there are bulges in coexistence of larger flakes or aggregates (Fig. 4b).

Compared to the work of Achaby et al. [23] on nanocomposite thin films with PVDF+GO, the values of Young's modulus that we report are lower: 67% for PVDF and 73% for the GO composite (at the same weight concentrations). However, going from thin films to microfibres, it emerges that the deformation capabilities of the materials are boosted. The strain at break of PVDF fibres is 13 times higher than PVDF thin films and 8-fold for PVDF+GO (Fig. 3b). Similarly, the toughness modulus is improved by 5.1x for PVDF and 3.4x for PVDF+GO (Fig. 3c). Strength is lowered by a factor of 2 for PVDF and 2.5 for PVDF+GO (Fig. 3a). The distributions present a Weibull modulus and intrinsic strength of 2.8 and 21 MPa for PVDF, 3.4 and 15 MPa for PVDF+G, 4.0 and 23 MPa for PVDF+GO. For both PVDF+G and PVDF+GO composites no premature failures are detected as all fibres fail in the plastic field. This unexpected reduction in strength might be related to an overestimation of the real cross-section of fibres, i.e. indicating a possible non-full cross-section.

## 2.6. Toughening mechanisms and microcracking

In this section, the mechanisms involved in the deformation of thin polymeric and composite electrospun fibres will be investigated. In particular, it can be observed that a localized plastic deformation of multiple necking regions propagates along a sample of PVDF+G (Fig. 6) before failure. The necking propagation is a primary contribution to energy dissipation.

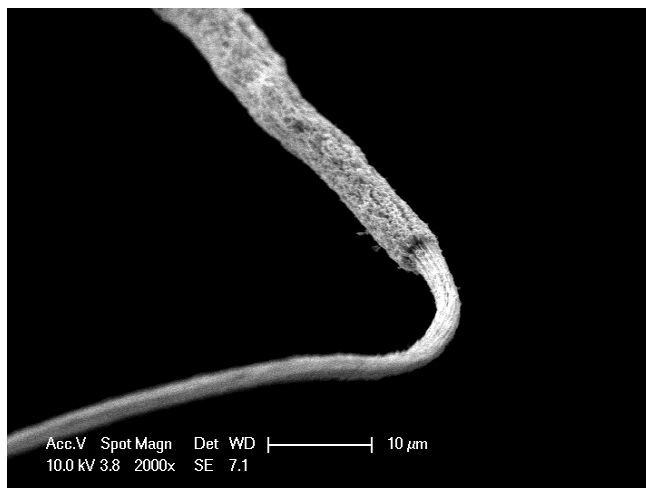


*Fig. 6 – Propagation of the necking region*

Thus, the fibres at this scale have a highly ductile behaviour [38] as very high values of strain at break were found. The average values for all nanocomposites are over 200%, meaning that fibres reached more than 3 times their initial length before failure. For pristine PVDF the ductility is even higher, as confirmed by a direct observation of fracture surface (Fig. 7), and reaches an impressive maximum of 544%. On the contrary, Macroscopic PVDF fibres [22] have a strain at break of 59%. So, the average strain at break of our microfibrils is 7-fold.

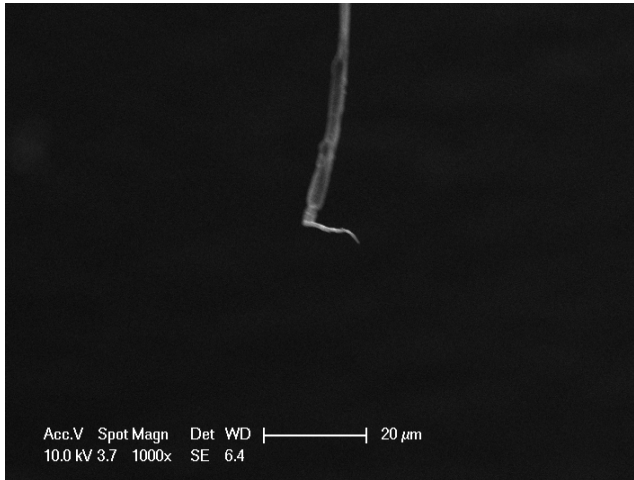


*Fig. 7 - Fracture surface of PVDF fibres*

The great performance, both in terms of strain at break and toughness modulus, of the fibres produced does not benefit from any external toughening mechanisms that could be cleverly exploited to enhance fibres' toughness, i.e. through the introduction of slip knots that create sliding friction [39, 40] or through an higher-order organization like yarns and coils, inside which fibres can slide and uncoil upon loading generating friction [41]. Instead, the performance of our fibres resides only in the internal capabilities of the material and its peculiar structure. The formation of multiple necking is caused by instability phenomena [42] that are supposedly increased by the presence of embedded fillers, which reshape the distribution of stresses in the fibres. Nanofibres and very slender structures [43] have high aspect ratio [42] and thus can accommodate more perturbation wavelengths. The spacing between consecutive neckings is shorter than the length of the fibres, thus electrospun fibres can display multiple necking in the same sample. In addition, we found that the same applies to polymeric straws, which are taken as a comparison in this paper.

Indeed, as it is shown in Fig. 7 and Fig. 8, multiple necks coexist in the electrospun fibres of this study. In literature there are several evidences of the formation of multiple necking in electrospun fibres [42, 44] but they are considered as weak points (loci of failure) of electrospun fibres. Conversely, in this work we will show that multiple necking (Fig. 7; Fig. 8) can represent a beneficial toughening mechanism. The phenomenon of the formation of multiple necking in electrospun fibres was observed by Zussman et al. [42] for PEO nanofibres deposited on a rotating wheel. The authors consider multiple necking as the defect

that caused the failure. Conversely, in our work we show that multiple necks can coexist and propagate in a stable manner. The propagation can extend to most of the fibre's length. In our experiments, the propagation was significantly higher for pure PVDF fibres, which have higher strain to failure. Therefore, necks are beneficial to the deformation capabilities of microfibrils upon loading and act as a toughening mechanism.

A possible explanation for the formation of multiple necks in electrospun fibres can be detailed as follows: a first neck is nucleated where there is a strong overlap in the stress field [38]. It propagates along the fibre up to a critical strain until when a predominant stress concentration rises somewhere else and a new neck starts to propagate. This mechanism iterates up to when the neck encounters a discontinuity during the propagation and the fibre fails. Stopping and restarting of a new neck could explain the jumps in the stress-strain curves observed in Fig. 3.

Differently from the work of Kim et al. on nanocomposite fibres [38], the fibres in this work do not have superficial macroscopic pores and they neither were formed during tensile testing (Fig. 4b,6,8,9).

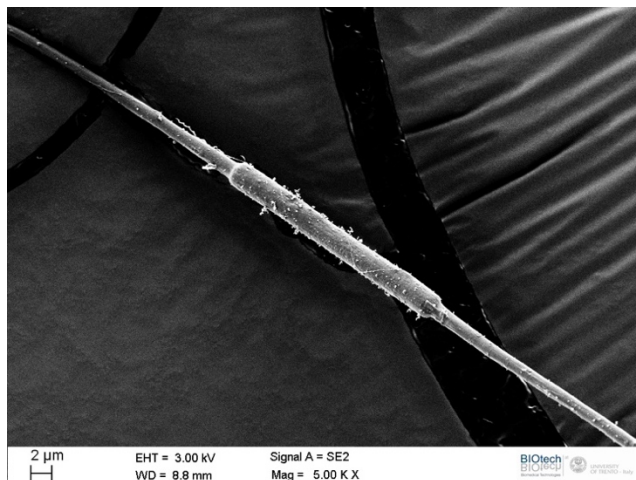


*Fig. 8 - PVDF+GO multiple necking*

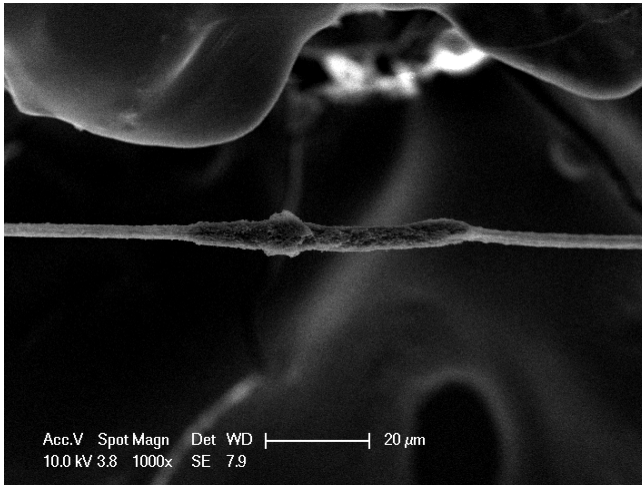


*Fig. 9 - Stiffer region in PVDF+G composite fibres*

Therefore, even if PVDF composite fibres still exhibit surface roughness, there are no points where necking is strongly favoured to form. As documented in Figs. 4b,8, there are some bulged regions where larger flakes are located. These zones can be called “stiff zones” because they are either intrinsically stiffer or thicker in diameter. In these zones, fillers are likely to generate multiaxial stresses. As highlighted in Fig. 4b and Fig. 9, necking formation is specifically triggered in the proximity of a stiff zone, where a strong multiaxial stress is predominant. This evidence is in full agreement with the mechanism of stopping and restarting of multiple necks propagation that was previously hypothesized. The propagation of a neck might stop in close proximity to a stiff zone, which is statistically distributed along the fibre, and then propagation restarts somewhere else.

When fillers are added, nanocomposite fibres have a higher number of stiff zones compared to the pristine polymeric fibres. This is likely to be the microstructural reason behind the decreased strain at break in the nanocomposite fibres. In fact, stiff zones will not be subjected to necking and nanocomposite fibres will have a lower overall volume that can undergo plastic deformation.

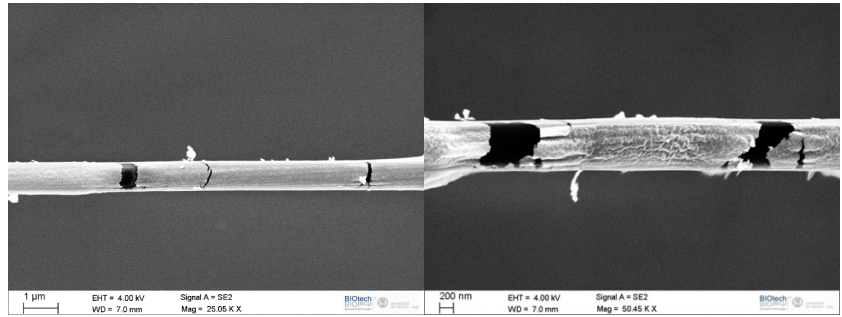


*Fig. 10 - Microcracking occurs in the regions that already underwent plastic deformation (necked region) in PVDF fibres*

Another phenomenon was observed only in PVDF samples (Fig. 10): microcracking.

It is not totally clear why this mechanism was not observed also in the nanocomposite fibres. It manifests only in those samples where the plastic capabilities of the fibres were fully exploited, i.e. the pristine polymeric fibres where ductility reaches its maximum extent.

Several microcracks can coexist in a single sample (Fig. 10) and have limited propagation meaning that the formation of microcracks do not account as the critical defect that leads to failure. Moreover, the propagation of microcracks can provide a small additional contribution to energy dissipation. In addition to this, microcracking (Fig. 10) reveals the hollow nature of the electrospun fibres. It might be then possible to estimate the wall thickness, which could give a more realistic value of cross section and thus a rise in the values of stress in the  $\sigma$ - $\varepsilon$  curves, bringing stresses back to the intervals reported in literature (Fig. 3a). However, even if the curves showed a systematic decrease in the stresses (Fig. 3a), it is not possible to measure the exact cross sections for each electrospun fibre since this would conflict with the mechanical characterization. Therefore, all the stress values for the electrospun fibres are intentionally left computed considering a solid cross section with the outer diameter (apparent cross section).

Hollow structures under tensile loads are able to shrink their cross section more than bulk structures because they have no internal physical constraints. This might explain the very high value of strain at break as well as why the values of stresses are lower compared to the study of Achaby et al. [23] and to the literature on PVDF [37]. The high deformation capabilities associated to a hollow tubular structure can be investigated at a macroscopic level on drinking straws tested under tensile loads. They exhibit a strong similarity with electrospun fibres

both in mechanical behaviour under tension and in the morphology of the fibres. When very thin walled structures like straws are pulled, they undergo a tangential instability phenomena that have not been noticed in electrospun fibres.

## 2.7. Mechanical models

This paper focuses on the mechanical and morphological characterization of single electrospun fibres. To extend the considerations of this paper to larger scale applications of electrospun fibres, such as films and bundles of fibres, it would be useful to have a simple mechanical model that describes the constitutive law of the single fibres. The implementation of such model in a FEM environment enables the prediction of the mechanical characteristics of higher hierarchy materials composed that have these electrospun fibres as the main constituent, such as the applications presented by Baniasadi [41].

The classical small-strain linear elastic theory is not suited to be applied at the remarkably high strain to failure of PVDF fibres, the same applies for the standard neo-Hookean models with two parameters,  $\mu$  shear modulus and  $\kappa$  bulk modulus.

However, there is a two-parameter model known under the name of Mooney-Rivlin equation (Equation 2) [45], which has far reaching applications for its simplicity. Indeed, it can expand the fit region but the shape of the function cannot approximate the polymeric stiffening at higher deformations [46].

$$\sigma(\lambda) = 2 (\lambda - \lambda^{-2}) \cdot (C_{10} + C_{01} \cdot \lambda^{-1})$$

*Equation 2 - Mooney-Rivlin equation for uniaxial tension. It links the stress to the stretch ratio ( $\lambda=\epsilon+1$ ) by means of the two parameters  $C_{10}$  and  $C_{01}$ .*

Higher order of the Rivlin formulation for rubber-like neo-Hookean solids might be needed to adequately describe the polymer behaviour at high deformations. They are based on the hypothesis of an isotropic elastic and incompressible material. The invariants for this model are formulated in terms of the principal stretches [47], they are denoted by  $\lambda_1$ ,  $\lambda_2$  and  $\lambda_3$ . In this case, the subscript 1 indicates the direction of uniaxial stretching.



$$\begin{cases} I_1 = \lambda_1^2 + \lambda_2^2 + \lambda_3^2 \\ I_2 = \lambda_1^2 \lambda_2^2 + \lambda_1^2 \lambda_3^2 + \lambda_2^2 \lambda_3^2 \\ I_3 = \lambda_1^2 \lambda_2^2 \lambda_3^2 \end{cases}$$

*Equation 3 - Deformation invariants  $I_1, I_2, I_3$  based on the principal stretches*

As a consequence of the hypothesis of incompressibility, i.e. constant volume, the third invariant  $I_3$  will be equal to 1. During uniaxial tension, the three principal stretches are linked as follows:

$$\begin{cases} \lambda_1 = \lambda \\ \lambda_2 = \lambda_3 = \left(\frac{1}{\sqrt{\lambda}}\right) \end{cases}$$

*Equation 4 - Principal stretches in uniaxial tension*

Rivlin suggested the following function for elastic strain energy density [48] that includes the deformation invariants:

$$W = \sum_{i=0, j=0}^{\infty} C_{ij} (I_1 - 3)^i (I_2 - 3)^j$$

*Equation 5 - The elastic strain energy density function formulated by Rivlin. Where  $C_{ij}$  are materials coefficients, and notably the first coefficient  $C_{00}$  is equal to zero as there is no stored strain energy in the undeformed state.*

Merging the previous formulas, the strain energy function can be written in terms of only the first principal stretch  $\lambda_1 = \lambda$  (Equation 6).

$$\begin{aligned} W(\lambda) = & C_{00} + C_{10}(\lambda^2 + 2\lambda^{-1} - 3) + C_{01}(2\lambda + \lambda^{-2} - 3) + C_{11}(\lambda^2 \\ & + 2\lambda^{-1} - 3)(2\lambda + \lambda^{-2} - 3) + C_{20}(\lambda^2 + 2\lambda^{-1} - 3)^2 \\ & + C_{02}(\lambda^{-2} + 2\lambda - 3)^2 \\ & + C_{21}(\lambda^2 + 2\lambda^{-1} - 3)^2(2\lambda + \lambda^{-2} - 3) \\ & + C_{12}(\lambda^2 + 2\lambda^{-1} - 3)(2\lambda + \lambda^{-2} - 3)^2 \\ & + C_{22}(\lambda^2 + 2\lambda^{-1} - 3)^2(2\lambda + \lambda^{-2} - 3)^2 \end{aligned}$$

*Equation 6 - Strain energy density as a function of one variable,  $\lambda$ , and the material coefficients  $C_{ij}$ . Here  $W$  is shown with the first 9 coefficients.*

The partial derivative of strain energy (Equation 7) is the resulting stress in the direction parallel to the applied stretch.

$$\sigma_{ij} = \frac{\partial W}{\partial \lambda_{ij}}$$

*Equation 7 - The partial derivative to obtain the stress from the strain energy density function*

Higher orders forms of the Rivlin's strain energy density function [49] were tested up to 9 coefficients, as shown in Equation 8.

$$\begin{aligned} & \sigma(\lambda) \\ = & 2C_{10}(\lambda - \lambda^{-2}) + 2C_{01}(1 \\ & - \lambda^{-3}) + 6C_{11} \frac{(\lambda - 1)^3(\lambda + 1)(\lambda^2 + \lambda + 1)}{\lambda^4} \\ & + \frac{4C_{20}(\lambda - 1)^3(\lambda + 2)(\lambda^2 + \lambda + 1)}{\lambda^3} \\ & + 4C_{02}(1 - \lambda^{-3})(\lambda^{-2} + 2\lambda - 3) \\ & + \frac{2C_{21}(\lambda - 1)^5(\lambda + 2)(5\lambda + 4)(\lambda^2 + \lambda + 1)}{\lambda^5} \\ & + \frac{2C_{12}(\lambda - 1)^5(2\lambda + 1)(4\lambda + 5)(\lambda^2 + \lambda + 1)}{\lambda^6} \\ & + \frac{12C_{22}(\lambda - 1)^7(\lambda + 1)(\lambda + 2)(2\lambda + 1)(\lambda^2 + \lambda + 1)}{\lambda^7} \end{aligned}$$

*Equation 8 - Stress-stretch relationship calculated from the Rivlin's model of hyper-elastic incompressible material tested in uniaxial tension with 9  $C_{ij}$  material coefficients*

Increasing the number of coefficients, the fit of experimental data, as expected, improves while still not fully appreciating the yielding of electrospun fibres (Fig. 12a). Aside from this, when new  $C_{ij}$  coefficients are added, the fitting curve starts to resemble more each specimen-specific variation rather than the overall trend (Fig. 12a). Another model for uniaxial tension of incompressible materials is the Ogden material model [50].

$$\sigma(\lambda) = \sum_{k=1}^N \frac{\mu_k}{\alpha_k} \left[ \lambda^{\alpha_k} - \left( \frac{1}{\sqrt{\lambda}} \right)^{\alpha_k} \right]$$

*Equation 9 - The stress-stretch relationship as described by the Ogden material model,  $\mu_k$  and  $\alpha_k$  are materials coefficients.*

The Ogden model was tested up to the third order, i.e. 6 coefficients, to fit the experimental data and it performed similarly to Mooney-Rivlin equation (Equation 2) and was very far from a good fit (Fig. 12a).

Coleman and Newman proposed a first order model (Equation 10) with three parameters that well describes necking formation and growth and the stiffening at high deformations of cold drawn necked polymers [51].

$$\sigma(\lambda) = \mu_1(\lambda - \lambda^{-2}) + \mu_2(\lambda^3 - \lambda^{-3}) + \mu_3\lambda(\lambda^2 - 1)e^{-\frac{1}{4}(\lambda^2-1)} + \mu_3\lambda^{-2}(1 - \lambda^{-1})e^{\frac{1}{4}(1-\lambda^{-1})}$$

*Equation 10 - First order of the constitutional law for fibres proposed by Coleman and Newman for incompressible materials. The stress-stretch relationship depends on three materials coefficients  $\mu_1$ ,  $\mu_2$ ,  $\mu_3$*

However, we found that this model is not capable of appreciating abrupt variations [52] in the yielding as it occurs for the electrospun fibres of our experiments (Fig. 12a). Coleman and Newman also offered a further development [51] of this model including the second derivatives of the strain energy of Equation 7 but this would introduce far too many complications towards an easy implementation of a material model for these fibres in FEM environments.

It seems that a model to properly fit the stress-strain characteristics of electrospun fibres should be designed with a different approach, we hereby propose a simple model that is derived from experimental observations. In all our experiments, we have noticed a consistency in both the outer diameter of the necked regions and the diameter of the non-necked regions, as displayed in Figs. 8,9. This finding is the ideal condition to apply a multilinear spring model [53] to describe the plastic behaviour of the fibres. After the yield point, each fibre can be modelled as two springs having different rigidities: i) the so called “un-necked regions” (they have a cross section  $A$  and contribute for a length of  $L$ ) and ii) the necked regions (cross section  $a$  and length  $l$ ), as shown in Fig. 11.

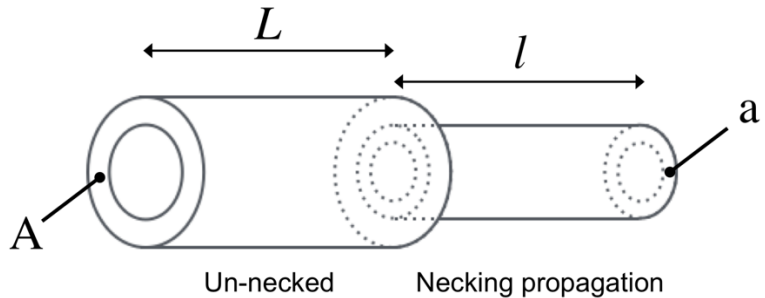


*Fig. 11 - Schematic of the model for the fibre after necking has occurred.*

The rigidity of the two springs is as follows:

$$k_1 = \frac{EA}{L} ; k_2 = \frac{Ea}{l}$$

*Equation 11 -  $k_1$  and  $k_2$  are the rigidities of respectively the un-necked and necked regions.*

When necking is propagating, the stretch ratios in the un-necked regions are very limited [54]. Hence, all the plastic deformation is acknowledged as if it was generated by a linear increase of the necked part, and thus of the value  $l$ , which grows proportionally to the strain (see Equation 15).

This model does not need to be changed when hollow fibres or multiple necking are considered because the lengths  $L$  and  $l$  become the sum of all the different regions having the same cross section. The onset strain for this model is chosen in the plastic region, where necking nucleates (see Fig. 13 for more details).

After the first neck is nucleated, the necked parts of the fibre are in the plastic regions, so the material will behave with a Poisson's ratio approaching 0.5 [55, 56]. It is then reasonable to apply the volume conservation:

$$AL + al = A_0L_0 \cong AL_0$$

*Equation 12 -  $A_0L_0$  is the volume of the fibre. Since yielding, in the electrospun fibres that were tested, occurs below 1% of strain, the cross section of the elastically loaded region ( $A$ ) can be considered to have approximately the same value of the initial cross section ( $A_0$ ), the error made is negligible. Therefore, for the volume of the fibre can be approximated with  $AL_0$ .*

The model of the whole fibre is a series of two springs having an overall rigidity  $k$  of:

$$\frac{1}{k} = \frac{1}{k_1} + \frac{1}{k_2}$$

*Equation 13 -  $k$  is the equivalent rigidity of the entire system*

During the tensile test, both lengths  $L$  and  $l$  change dynamically ( $L$  decreases,  $l$  increases) and thus the related rigidities vary.

Manipulating Equation 2-4 it is possible to derive the following expression:

$$k = \frac{k_0}{1 + \frac{l}{L_0} \left( \frac{A}{a} - \frac{a}{A} \right)}$$

*Equation 14 -  $k_0$  represent the initial rigidity of the unloaded fibre (i.e.  $EA_0/L_0$ ).*

In Equation 14 all the quantities but  $l$ , which will be the variable, are fixed as they depend on the initial geometry of the fibre. Experimental observations (Figs. 6,8,9) show that  $a$  remains constant. However, since the x-axis on the  $\sigma$ - $\varepsilon$  plot is  $\varepsilon$ ,  $l$  can be linked to  $\varepsilon$  using Equation 12 and the definition of engineering strain. It holds:

$$\varepsilon = \frac{\Delta L}{L_0} = \frac{(L + l) - L_0}{L_0} = \frac{l}{L_0} \left( 1 - \frac{a}{A} \right)$$

*Equation 15 - relationship between  $\varepsilon$  and  $l$*

A cleaner expression of the  $\sigma$ - $\varepsilon$  relationship is achieved with the following factoring:

$$\left( \frac{A}{a} - \frac{a}{A} \right) = \left( 1 - \frac{a}{A} \right) \left( 1 + \frac{A}{a} \right)$$

*Equation 16 - algebraic factoring*

Therefore, the relationship between  $\sigma$ - $\varepsilon$  could be represented as follows:

$$\sigma = k \frac{L_0}{A} \varepsilon = \frac{E}{1 + \frac{l}{L_0} \left( 1 - \frac{a}{A} \right) \left( 1 + \frac{A}{a} \right)} \varepsilon = \frac{E}{1 + \varepsilon \left( 1 + \frac{A}{a} \right)} \varepsilon = E(\varepsilon) \varepsilon$$

*Equation 17 - where  $E(\varepsilon)$  is a function of the strain*

From Equation 17 it is necessary to introduce the constant  $\sigma_y$  to ensure the continuity between the elastic part and the plastic regime [57] and an exponent  $\alpha$  to fit the large-deformation stiffening of the curve.

$$\sigma = E(\varepsilon)(\varepsilon - \varepsilon_y)^\alpha + \sigma_y = \frac{E}{1 + (\varepsilon - \varepsilon_y) \left( 1 + \frac{A}{a} \right)} (\varepsilon - \varepsilon_y)^\alpha + \sigma_y$$

*Equation 18 -  $\sigma$ - $\varepsilon$  relationship that describes the fibre's behaviour after the elastic regime. The variable becomes  $(\varepsilon - \varepsilon_y)$  as the relationship is used to fit the experimental data after the nucleation of the first neck.*

The transition between the elastic and the plastic region is sharper in electrospun fibres (Fig. 2) than in straws (Fig. 13), which makes it

reasonable to consider that necking begins immediately after the yield point. The overall stress-strain relation can be described with the aid of a multilinear model, which is commonly used to fit the mechanical response of polymeric and silk fibres [53, 57, 58]. The two fields model have an initial linear elastic part and then a plastic behaviour as formulated in Equation 18. The constitutive behaviour of the fibres can be described as follows:

$$\left\{ \begin{array}{l} \varepsilon \leq \varepsilon_y: \quad \sigma = E_1 \varepsilon \\ \varepsilon > \varepsilon_y: \quad \sigma = \sigma_y + \frac{E_2}{1 + (\varepsilon - \varepsilon_y) \left(1 + \frac{A}{a}\right)} (\varepsilon - \varepsilon_y)^\alpha \end{array} \right.$$

*Equation 19 - The constitutive model that describe the stress strain behaviour of the fibres.*

Fig. 12b shows the application of this model to the experimental data points of a hollow PVDF fibre and the resulting fitting parameters of Equation 19.

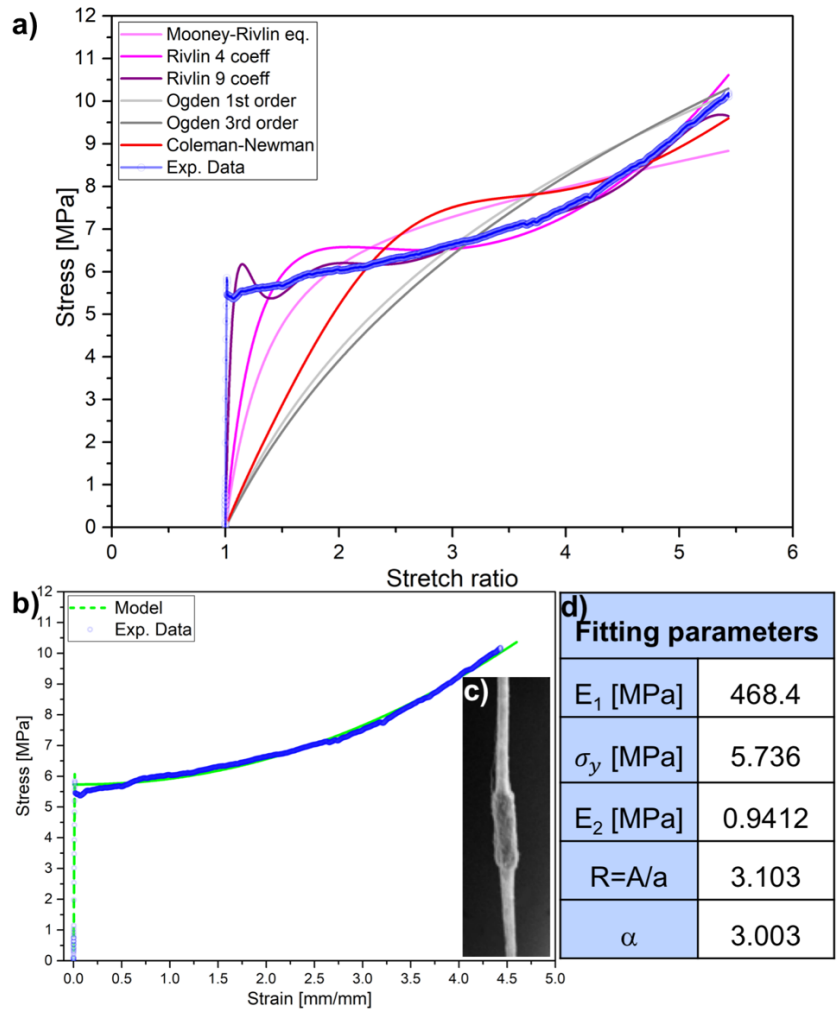


*Fig. 12 - a) Experimental data compared with different fitting models from the literature: Mooney-Rivlin equation, Rivlin with 4 coefficients, Rivlin with 9 coefficients, Ogden 1<sup>st</sup> order, Ogden 3<sup>rd</sup> order, 1<sup>st</sup> order of Coleman-Newman equation. b) The blue dots are the experimental data points of a PVDF hollow fibre. The two green dashed lines represent the fitted constitutive model. c) SEM image showing the un-necked and necked regions. d) The table on the right shows the best-fit of the parameters in Equation 19.*

The model proposed is simple and it is worthwhile to notice that it offers a constitutive description of the mechanical behaviour and toughening mechanisms that is based mostly on geometrical considerations i.e. necking propagation. It can fit with good approximation the strain hardening behaviour in the plastic region and the derived geometrical parameter  $R$  (the ratio between un-necked and necked cross-sections) is in agreement with SEM morphological observations (Fig. 12c). The

$\sigma$ - $\epsilon$  relationship in Eq.10 for single fibres offers a simple three parameters ( $R, \alpha, E_2$ ) model that describe the fibres' performance after yield. These parameters are easily measured experimentally on test fibres. They can be then transferred into the constitutive law to simulate the mechanical response of higher hierarchy structures such as technical textiles.

## 2.8. Comparison with straws

A simple mechanical test of a common macroscopic structure, a drinking straw, can provide unexpected insights on the microscopic phenomena occurring on electrospun fibres. In fact, polypropylene straws are very informative on the morphological aspects discussed above and allowed us to link them to large scale tangible observations. SEM imaging cannot be performed live during the nanotensile test. Moreover, some phenomena go missing i.e. nucleation of the first neck.

This comparison is reported to the reader in order to give a better visual understanding (*Video available by email*) of what happens during the testing of hollow structures. It also helps to support and ease the comprehension of the hypothesis presented in the toughening mechanisms' section, especially as regards the nucleation of the first neck and the stable propagation.

In the following section, mechanical tests of straws are presented. The multiple necking phenomenon consistently occurred in every sample that was tested with at least two necks.

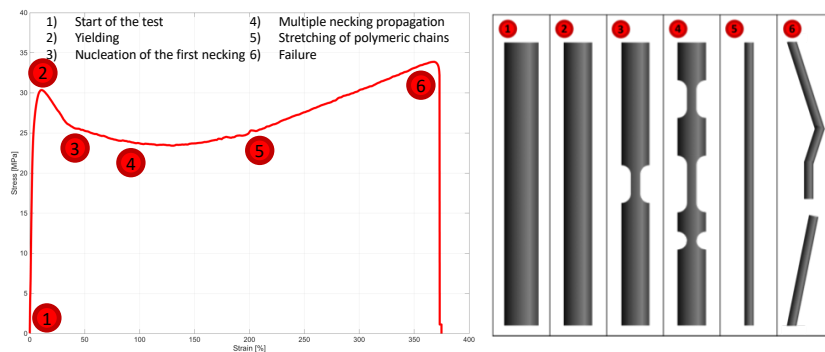
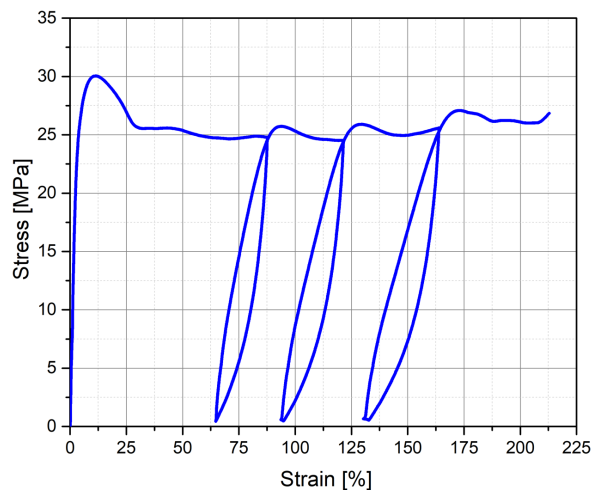


Fig. 13 - Stress-strain curve of PP straw with highlighted all the phenomena occurring during the tensile testing.



Polypropylene straws, recently standardized in ISO 18188:2016 [59], showed an average yield stress of 30.9 MPa, strain at break of 379 % and elastic modulus of 0.75 GPa (considering the real cross-section).

A multi-cyclic test performed on a straw in Fig. 14 can show the dependency of the yielding phenomenon on the strain history. Indeed, the successive yielding shows a smaller difference between yield stress and the average stress of the plateau after yielding. Besides, electrospun fibres display a very sudden transition (Figs. 2,12) around the yield point and the correlated stress difference becomes less evident. This could be due to their strain history. During electrospinning, polymeric fibres are subjected to impressive strain rates, which can reach values of  $10^3 \text{ s}^{-1}$  [60].



*Fig. 14 - Multicycle tensile test on PP straws shows that the stress drop after yielding is decreased if the sample was subjected to previous plastic deformation during its loading history.*

Furthermore, multi-cyclic tensile tests of straws show that the propagation of necking can continue in a stable way even after complete unloading. The tensile test of straws (Fig. 13 and Video) clearly reveals the stiffening regime that occurs after propagation of the necked regions is so high that eats up all the available quota of  $L$ . This regime is caused by the direct stretching of the back-bones forming the polymeric chains [35].

Being easier to test than electrospun fibres, straws were tested also at different strain rates. Straws were tested in their normal conformation and after they were cut along their axis. The yielding phenomena in solids with viscoelastic behaviour is temperature and strain-rate

dependent. Indeed, as described by the Eyring model [61] yielding in straws (Table 2) and cut straws (Table 3) occurs at higher stresses while increasing strain rate.

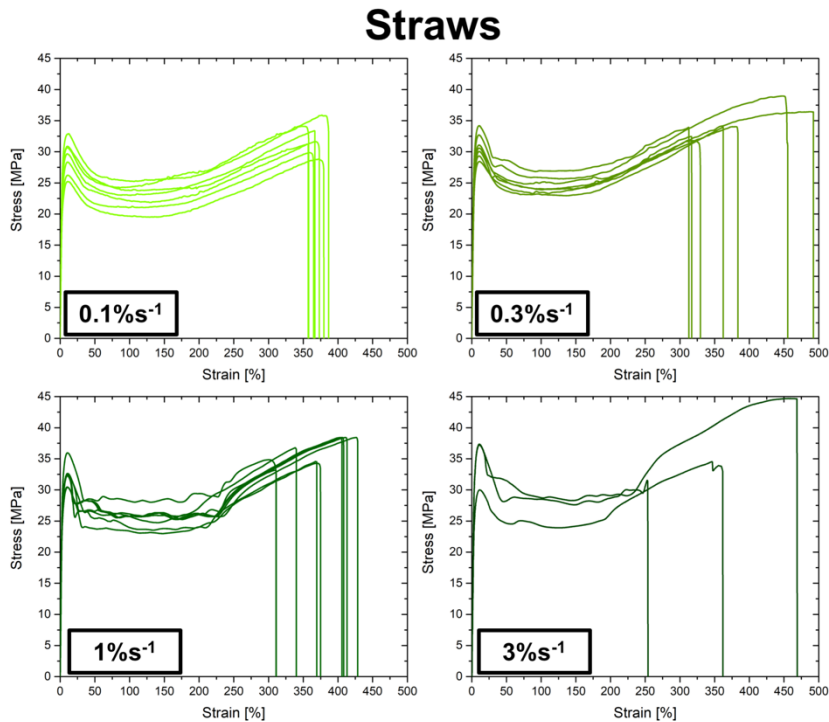


*Fig. 15 - stress-strain curves of the straws tested at 4 strain rates*

Straws				
Strain rate [%s <sup>-1</sup> ]	0.1	0.3	1.0	3.0
Young's Modulus [MPa]	0.68±0.07	0.75±0.06	0.76±0.07	0.92±0.13
Yield Strain [%]	10.7±0.3	10.6±0.3	10.6±0.3	11.2±0.3
Yield Stress [MPa]	29.1±2.7	30.9±2.0	32.3±1.6	34.8±4.2
Strain at break [%]	369±11	379±70	374±44	362±108

*Table 2 - mechanical properties of the 4 sets of straws*

## Staws cut along the axis

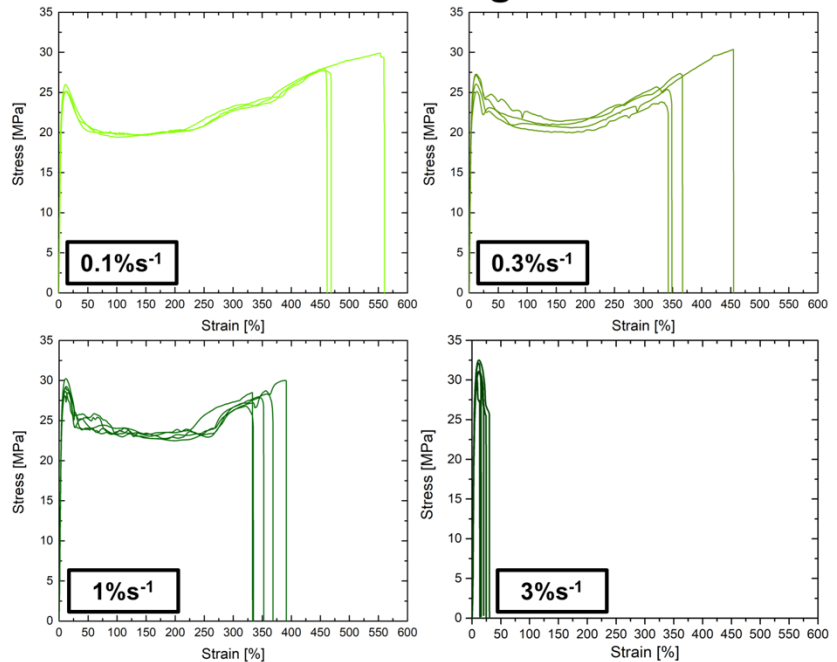


Fig. 16 - stress-strain curves of the staws cut along the axis tested at 4 strain rates

Staws cut along the axis				
Strain rate [%s <sup>-1</sup> ]	0.1	0.3	1.0	3.0
Young's Modulus [MPa]	0.72±0.02	0.72±0.08	0.82±0.06	0.89±0.05
Yield Strain [%]	12.7±1.1	12.4±0.9	11.7±0.7	11.3±1.8
Yield Stress [MPa]	25.3±0.4	26.4±0.9	29.1±0.7	31.3±1.0
Strain at break [%]	497±55	420±91	356±24	21±7

Table 3 - mechanical properties of the 4 sets of staws cut along the axis

Cut staws show a decrease in strain at break while the strain rate is increased. This trend is not present for staws, where the strain at break of the material seems to be rather independent from the strain rate. This might be correlated either to their peculiar structure or to more critical clamping conditions for cylindrical objects. Indeed, the absolute values of strain at break for cut staws are superior to staws. The exception is in the tests of the cut staws at the highest strain rates (3%<sup>s<sup>-1</sup></sup> in Fig. 16) that show premature failure. All the samples failed before 50% strain, in contrast the incidence of premature failures for staws has a much lower extent as the tests in Fig. 15 show. In those tests necking is not

able to fully develop or to have a stable propagation. This unfolds the fact that necking is a more complex phenomenon when moving outside the quasi-static loading conditions. Neck formation depends on time so creep and viscoelastic properties have to be considered [62] for a comprehensive theory of necking.

### **3. Composites from natural structures**

#### **3.1. Brief history of the modification on cellulose-based materials**

Most industrial polymers do not suffice in terms of either stiffness, strength and toughness requirements for load bearing applications. Natural fibres could overcome some of the weaknesses but must be embedded to form a polymer composite. There has been a lot of research on fibres and green composites (i.e. composites that use natural fibres as reinforcing element) but they still see limited applications. Prior to 2018 most of the research on cellulose composites and modified wood for mechanical applications was focused on fibres obtained from wood pulp or from green composites based on natural fibres. To cite some advanced applications, Japanese researchers used wood pulp for the production of lighter car parts and a European joint technology initiative (CLEAN SKY) had the aim to develop innovative bio-based resins for aeronautical applications. The latter focused on a sugar-derived epoxy resin reinforced with jute fibres. Moreover, hemp [63] or kenaf fibres [64] are used in reinforced concrete or to reinforce industrial polymers like PE [65, 66] PLA [67] and PP [68, 69]. Starting from natural cellulose fibres to build up a composite can be a high-cost process with low-volumes. So research recently focused on cellulose fibrils obtained from wood pulp to achieve high-volume low-cost processes that can compete with traditional polymers [70, 71].

However, a raw material like wood pulp is not ideal for mechanical applications as it leads to the disruption of the internal structure of wood, complete removal of the matrix and loss of microfibrils' alignment. The internal wood structure and microfibril angle (MFA) [72] are the two factors contributing to bulk wood properties as an engineering material. Of course, microfibrils' alignment can be rebuilt afterwards as studies have shown [73] but it involves complex and high cost processes.

## 3.2. Natural cellulose fibres & functionalizations

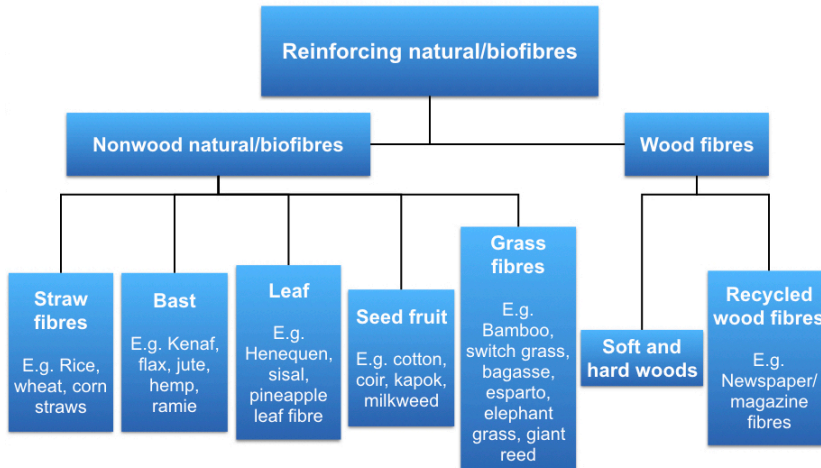


*Fig. 17 - Types of natural fibres*

Cellulose fibres can be derived from wood or plants (Fig. 17). In fact, the same building blocks are found in wood cell walls and natural cellulose fibres. The molecular components are always cellulose, hemicellulose and lignin (Fig. 18). Therefore, building a fibre-reinforced composites derived from aligned cellulose fibres, a transparent paper, or a densified wood beam has far more similarities than the reader might expect.

These building blocks can be assembled in many ways, each determining a specific performance within wide variety of properties available for biological materials (Fig. 31). Indeed, precise correlations exist between stiffness/strength and the assembly parameters such as fibrils alignment and cellulose content (Fig. 18).

Such similarities in chemistry and structures are relevant to understand the more complex architectures of wood, reed and bamboo and provide technical insights on how to exploit their cellulose template to build an engineered composite.

<i>Fibre</i>	<i>Tensile Strength (MPa)</i>	<i>Strain at break (%)</i>	<i>Density (g/cm<sup>3</sup>)</i>	<i>Composition (C=cellulose, H=Hemicellulose, L=Lignin, P=Pectin)</i>
<i>Flax</i>	600-1000; 345-1035; 500-900; 800-1500	1-2; 2.7-3.2; 6-10	1.4-1.5	71%C,19%H,2%P,2%L
<i>Jute</i>	393-773; 400-800; 200-450	8; 1.5-1.8	1.3-1.5	45-72%C,14-21%H,12-26%L
<i>Cotton</i>	287-597; 300-700	7.0-8.0	1.550	85-90%C,0.7-1.6%L
<i>Hemp</i>	690; 550-900; 591-857; 310-750	2-4; 6	1.48-1.5	56%C,20%P,10%H,6%L
<i>Ramie</i>	400- 938;560	8	1.33-1.5	68.6-91%C,5-17%H, 2%P,1%L
<i>Sisal</i>	511-635; 600-700; 80-840; 227-700	10-25; 3-14	1.33-1.5; 1.45	57%C,16%H,11%L
<i>Coir</i>	175; 106-175; 131-175	30-49; 15-40	1.15-1.2	33%C,18%H,36%L
<i>Kenaf</i>	295-1191; 930	1.6	1.2	37-49%C,18-24%H,15-21%L
<i>Pineapple</i>	413-1627	0.52-3; 2.4	1.44	73%C,7%H,11%L

*Table 4 - mechanical properties and chemical composition of natural cellulose fibres. Data were obtained from several references [63, 67, 68, 74-83], where different data are reported, multiple ranges are shown.*

The stiffness and strength of the cellulose-based fibres are determined mostly by two factors: orientation of cellulose microfibrils with respect to the axis [76] (MFA) and cellulose concentration. The empirical formula (Equation 20), which is derived from fitting of a large dataset of experimental data of natural fibres (Fig. 18), links those two factors with the fibres' strength:

$$\sigma = 334.005 - 2.830 * \theta_{fibrils} + 12.22 * (\%cellulose)$$

*Equation 20 - Empirical formula that correlates the stress of natural cellulose fibres with MFA and cellulose content [84]*

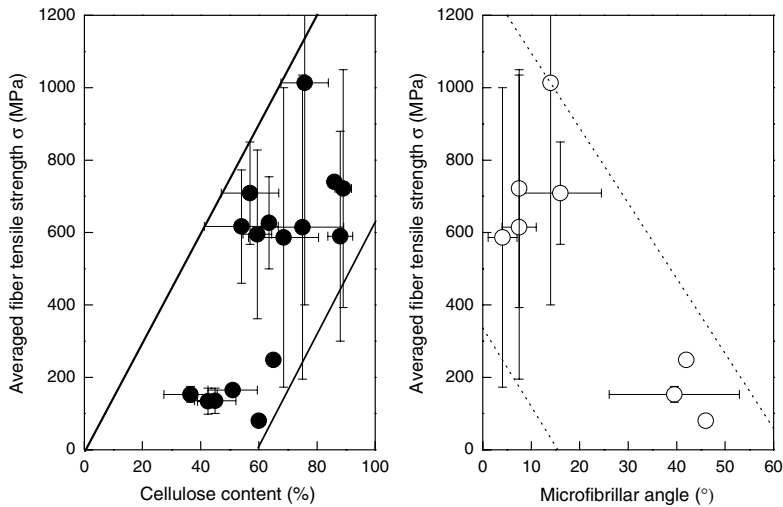


*Fig. 18 - reprinted with permission from [76]*

The failure stress of fibres increases with fibres alignment and cellulose content. Conversely, plants and plant fibres that have lower MFA, i.e. with a more prominent spiral orientations, are more ductile (Equation 21).

$$\varepsilon = 2.78 + 7.28 * 10^{-2}\theta + 7.7 * 10^{-3}\theta^2$$

*Equation 21 - Empirical formula to correlate the strain at break of natural cellulose fibres to MFA [84]*

We can extend this concept to bulk cellulose materials. Reed and bamboo are known to have higher fibril orientation and lower MFA than wood [85, 86]. Indeed, their culms reach superior mechanical and flexural properties [85-88].



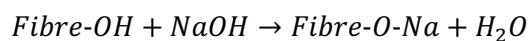
Historically, research on textile industry products has been widely explored, for example by thoroughly studying chemical and physical modification of cellulose-based natural fibres. On the other hand, while bulk cellulose fibrillar materials have far more interest for engineering and structural applications, they are mostly utilized in their natural shape and form.

This means that the knowledge gathered by the textile industry faces a close-to-zero exploitation in this area, as bulk fibrillary materials have a structure which is similar to that of cellulose.

Therefore, we are interested to apply that wide knowledge framework to bulk cellulose-based materials. In fact, treatments like mercerization (mainly utilized on cotton) and TEMPO surface functionalization are especially appealing as they allow the applications of cellulose microfibrils (MCFs) as functional nanomaterials. For example, TEMPO (2,2,6,6-tetramethylpiperidine-1-oxyl) oxidation permits the full conversion of the carboxylic acid at C6 position in the cellulose structure improving chemical affinity with water and metal ions [89].

MCFs can be assembled in a transparent paper and functionalized with a conductive coating [90] for optoelectronic properties. The functionalized paper couples light transmission (76% at 550nm) through the surface with electron transport on top of cellulose with a sheet resistance of 2.5 k $\Omega$ /sq. Transparent and conductive films are used as electrodes in solar cells and organic light emitting diodes that can be applied for flexible displays [91] and can withstand temperatures up to 150-200°C [92]. Flexible, transparent and conductive cellulose paper is becoming a strong alternative to Indium Tin Oxide (ITO), a transparent conductive material widely used as electrode material (e.g. for defrosting airplane windows), which is rigid and fragile and thus not suitable for flexible electronics [90].

Mercerization is a finishing surface treatment commonly used in textile industry on cellulose fabrics. It improves the uptake and/or the chemical affinity with the dye, the strength of the fabrics, their shininess and reduces shrinkage. Mercerization involves a chemo-mechanical treatment. Fibres are immersed in an alkaline environment, usually NaOH solutions are used, and are pre-stressed. This treatment leads to the formation of the so called “alkali cellulose” (Equation 22).



*Equation 22 - alkaline treatment on cellulose fibres, formation of “alkali cellulose” [75]*

Among natural fibres, ramie is the ideal candidate for macroscopic applications as they are characterized by length and strength values competing with synthetic fibres and higher than those of cotton or silk fibres [81]. Ramie fibres subjected to mercerization treatment have an improvement of their tensile strength as well as fracture strain [81].

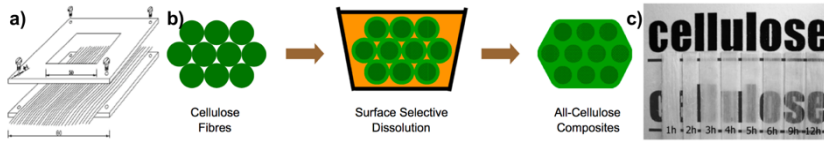


*Fig. 19 - a) aligned ramie fibres b) selective surface dissolution of cellulose fibres c) final all-cellulose composite - reprinted with permission from [93, 94]*

### 3.2.1. All-cellulose composites

Natural composite based just on ramie fibres can be produced. This type of material is called an all-cellulose composite, where the cellulose fibres play both the role of reinforcing fibres and the matrix. They comprise a surface selective dissolution of the fibres that can be achieved with organic solvents. For example, the surface dissolution with LiCl+DMAc of aligned ramie fibres coupled with a final mercerization allowed to obtain a final composite with enhanced strength (540 MPa) [94]. Notably (see Chapter 3.2.3), in composites with high fibre volume fraction like all-cellulose composites with aligned fibres, due to the removal of interfaces, the transparency is improved (Fig. 19c).

### 3.2.2. Transparent cellulose paper

Paper and wood are materials based on the same structural template: cellulose. Transparent paper was first developed in 1846. The process required a selective dissolution of the cellulose fibres after a treatment in sulphuric acid or diluted ammonia [95].

Transmittance [96] and haze [97] of transparent paper can be tailored using different diameters of its constituents: cellulose micro and nano-fibrils. Decreasing diameters, haze is reduced and transmittance is improved, reaching transparency higher than plastics with cellulose fibrils of 10 nm diameter subsequently TEMPO treatment [96].

The current state of the art of transparent cellulose composites is characterized by ultrahigh transparency (96%) and ultrahigh haze (60%) [98]. With a high haze the incoming light rays are spread on a large cone after they have interacted with the optical medium as in Fig. 20b. Conversely, glass is a material with high transparency but

extremely low haze. These two properties are a synonym of optical clarity. However, more than glass, highly transparent and high haze materials can have positive outcomes for solar cells applications as the light will have longer residence time within silicon medium and better efficiency of the solar cell [98].

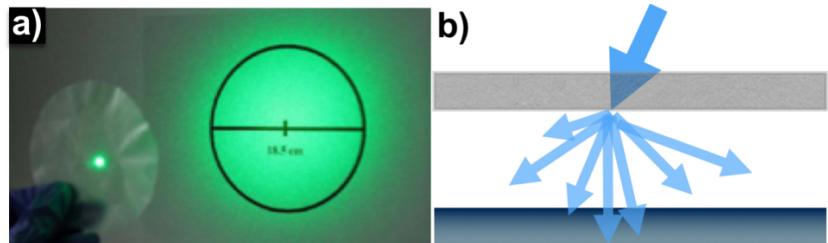


*Fig. 20 - a) Cellulose transparent paper with high transparency and high haze - reprinted with permission from [98], Copyright 2014 American Chemical Society. b) Schematic depiction of the interaction of light with such a film for solar cells applications.*

### 3.2.3. Transparency in wood

As seen in the previous section, scientific research took almost 150 years to go from transparent paper to truly transparent wood. Indeed, turning wood into an optically transparent material presents many challenges and a chemical treatment is not enough. Fink's original idea for a transparent wood was published in 1992 [99]. Wood was chemically bleached to reduce its light absorption and two resins were infiltrated into the so obtained structure in order to achieve optical transparency. Fink reported an overall refractive index  $n=1.56$  after chemical bleaching.

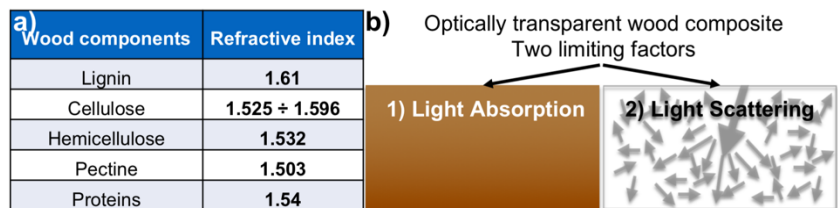


*Fig. 21 - a) Wood components and their refractive indexes b) the two factors that are limiting wood transparency.*

Transparency requirements are related to the limiting factors shown in Fig. 21b: i) light absorption and ii) light scattering. The former is mostly caused by lignin which has a strong absorption in the visible range and

contributes to 80–95% of the overall light absorption in wood [100]. The latter generates a series of refractions and reflections that occur at every minuscule interface between air and wood cell walls, such as air-fillings or micro-sized cavities [99], thus reducing optical clarity. In 2016, Berglund's group presented [101] a revision of Fink original work, which was aimed to wood anatomy, to also provide good structural properties to the transparent wood panels. The wood structure was delignified and impregnated with pre-polymerized PMMA through vacuum infiltration [101]. The material had optical transmittance of 85% and haze of 71% and was 10x thicker than previous works on transparent paper. Obviously, optical transmittance is strictly correlated with sample thickness and it goes from 90% at 550nm for 0.7 mm to 40% for 3.7 mm.

The removal of lignin is key to obtain transparent wood [102] as lignin has a dark colour while cellulose is almost colourless. Additionally, polymer infiltration occurs within the natural wood microstructure, forming strong interactions. Indeed, the collective scattering occurring at the polymer–delignified wood interfaces is presented as the probable reason for the high transmittance and high optical haze achieved [102].

After removing lignin, the scattering of light is not eliminated. According to Snell's law of optics the scattering is bigger the higher is the difference of refractive indexes at the interfaces. The voids should be filled with a material that should have: i) low absorption in the visible range and ii) refractive index closely matching that of cellulose (Fig. 21). Therefore, the best polymers for infiltration are those refractive indexes close to that of the cellulose matrix, for example Poly-N-vinyl pyrrolidone (PVP) and Epoxy resin. In order to impregnate a structure with PVP, a solution with high solvent concentrations (85wt%) is needed [103]. Fig. 22 illustrates the results of this process. Yet the solvent will evaporate, leave cavities and create new interfaces. Therefore the same research group, in a second iteration of this approach, presented wood microstructure infiltrated with epoxy [102]. Epoxy resin offers clear advantages. Zero solvent evaporation takes place in the process, the liquid resin cross-links in situ and the shrinking is very limited.

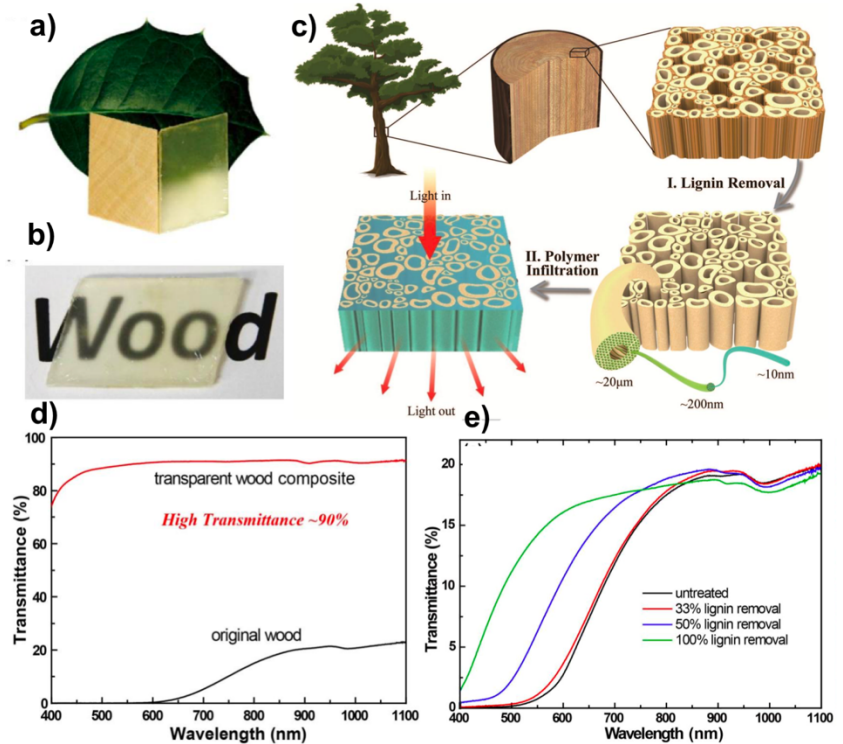


Fig. 22 - a) wood and transparent wood b) optical clarity of wood composite is very good when trying to read a text in close proximity c) schematic of the process to obtain the transparent wood composite, the samples obtained from the cross section of wood, which is called R-wood, are shown d) changes in optical transmittance for different lignin concentrations e) Comparison of the optical transmittance of wood & transparent wood composite in the visible to Near Infrared range - reprinted with permission from [103]

### 3.3. Recent advancements on wood modifications

Wood treatments are crucial to reduce wood intrinsic weaknesses. They range from chemical paints to thermal processes and they can provide fire retardancy or improved dimensional stability. The recently renewed interest for such treatments is related with the architectural stride to build always taller timber housing [104] and the scientific discovery of densification. Densification is a compound treatment that allowed to achieve modified timber with strengths in the order of magnitude of the

common metal alloys used for construction. With respect to processing, densification for wood yields similar structural modifications to those of mercerization for natural cellulose fibres. However, the densification route has still to be scientifically expanded and could allow to achieve superior mechanical or other remarkable properties.

For instance, Glulam (or glue-laminated timber) consists of sawn lumber laminas bonded together. It has controlled and consistent properties, is not affected by the natural growth features of wood and the employed volume of wood is optimized. When reinforced, Glulam changes the mode of failure from brittle to ductile and increases the load-carrying capacity of the beams. Reinforcements with steel plate and carbon fibre reinforced polymer (CFRP) have been tested. [105].

The same applies to CLT timber, which is a multi-layered wood panel. The wood laminas are assembled as modular elements.

While in Glulam the grain of all laminations runs parallel to the length [105], CLT timber's panels are assembled in a stack where each layer of laminas is tilted of 90° respect to the previous layer. CLT timber, usually made from spruce pine, is formed with polyurethane or phenol-resorcinol-formaldehyde resins as adhesive and showed superior durability in the delamination tests, after being subjected to accelerated ageing [106].

Both Glulam and CLT (in a ratio 80-20%) were massively utilized in the Mjostarnet building, by Moelven Limtre, that is currently holding the record height for a modern timber building of 85.4 m (Fig. 23). The volume of high performing timber structures was 2150m<sup>3</sup> of Glulam and 535m<sup>3</sup> of CLT [107]. These two materials can be combined “Lego-like”, as a modular material: cut into shape in the manufacturing plant and then assembled on-site with high geometrical precision and minimal-to-none error correction required [107].



*Fig. 23 - Mjøstårnet 84.5 m tall inaugurated in March 2019*

Architects are not stopping there, they are starting to conceive wood buildings that will compete in height with skyscrapers. An example is project of the Oakwood Timber Tower of London, which is supposed to be higher than 300 meters, as it appears from the concepts of PLP Architecture.

However, the technical path to follow in order to reach these heights is not clear and requires further scientific advancements. Certainly, starting from a stronger and tougher “Lego brick”, the lamina, would boost the potential for structural applications of these materials in extreme architecture. In the next chapter a technological process is presented for exploiting cellulose-based materials in high performance laminas for engineering applications. Since wood is a largely abundant natural resource used for its structural properties, engineers are looking for higher stiffness and strength. To this aim, as seen for cellulose fibres, wood can be modified playing on two factors: alignment, void reduction and cellulose content.

A first set of treatments was developed and can be grouped into thermo-hydro-mechanical treatments. They offer structural compaction to wood, plywood or bamboo [88, 108-112] with an increase in physical properties. They are based on a combination of steam and hot-pressing

at different pressures/temperatures. However, the effects on wood are not entirely permanent and may be reversed, up to a certain extent, when exposed to humidity [109, 113].

Recently, a second group is starting to develop: the chemo-thermo-mechanical treatments [114-116]. They are derived from the alkali processes, like mercerization, used for cellulose fibres and transparent paper. The goal of these treatments is to modify the chemical composition and therefore the relative cellulose content in the wood structure. They yield a more stable structure and surprising mechanical performances were achieved [114].

There are obvious fire-related concerns in tall wood building since wood is a combustible material but, compared to the other construction materials, wood can resist at higher temperatures and maintain the core performance. In fact, it can char externally without preventing the internal structural functions. Additionally, multilaminar structures like CLT have shown that they can be self-extinguishing. [117, 118]. Notwithstanding, regarding the fire issue the small-scale testing are very promising but still large-scale application will require skillful engineering solutions. Hence, the inauguration and technical advancement brought by Mjostarnet and similar projects deserve the attention of the scientific community.

### 3.3.1. Nanoparticles in wood and cellulose-based materials

With the aim of modifying wood properties, nanoparticles could prove significant.

For example, already existing industrial processes could be exploited. Empty-cell is used for impregnating wood under pressure with preservatives [119]. This process was used to introduce nano-silver and borax inside wood structures and resulted in improved fire retardant properties [120]. Similarly, spruce was impregnated with nano-silver and then thermo-compressed at 4h for 150°C with a significant increase in strength and impact resistance [121].

Nano-silver [122] and nano-copper suspensions [123] can increase the thermal conductivity and thus polymerization quality in wood particleboards and reduce press-time. As the permeability of particleboards to gases is decreased, a better bonding in the structure of wood plus nanoparticles is expected.



Also bamboos were subjected to modifications using inorganic oxides and nanoparticles like ZnO, SiO<sub>2</sub>, TiO<sub>2</sub>, and CaCO<sub>3</sub> and in some cases treated with silanes to reduced moisture content, retarded burning, improves resistance to UV radiation and provide super-hydrophobicity (with contact angles up to 161°) [124, 125].

## 4. Nanoparticles in natural cellulose-based composites

Recently, several chemical and physical treatments were developed to improve different properties of wood-like materials. Densification leads the group in terms of mechanical results and comprises a chemical treatment followed by a thermo-compression stage. First, chemicals selectively etch the matrix of lignin and hemicellulose. Then, thermo-compression increases the packing density of cellulose microfibrils boosting mechanical performance. In this paper, we introduce an additional nano-toughening treatment on densified giant reed to further improve the mechanical performance in comparison with the state-of-the-art. The modified nanocomposite materials are stronger and show higher specific toughness moduli. After the addition of nanoparticles, no relevant structural modification is induced as they are located in the gaps between cellulose microfibrils. Their peculiar positioning could increase the interfacial adhesion energy and improve the stress transfer between cellulose microfibrils. The process presented stands as a viable solution to introduce nanoparticles as new functionalities into cellulose-based natural materials.

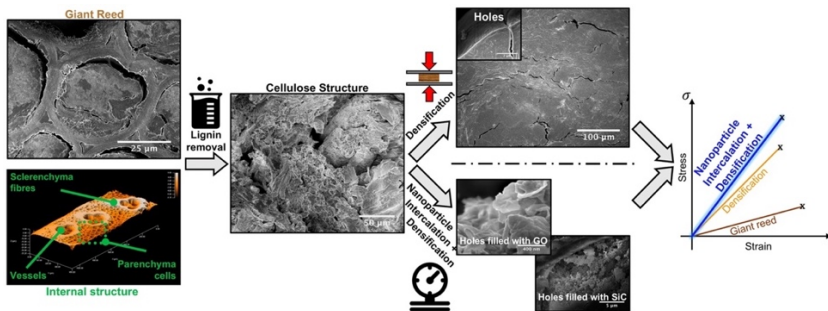


Fig. 24 - graphical abstract that shows the entire process

Nowadays, research on natural materials and their technological optimization play a fundamental role in sustainable socio-economic development [126, 127]. In particular, cellulose-based materials such as wood, bamboo, reed and natural fibres have attracted enormous attention [87, 88, 128-130], given their high versatility suitable for a variety of applications including renewable energy source, fuel, comfort, furniture, construction and recyclable packaging [129, 131-133]. Moreover, chemically treated wood can be turned into a

transparent and conductive substrate for solar cells applications, flexible transistors and electronics display such as LCD and OLEDs [134, 135]. Besides the aforementioned applications, the most extensive utilisation of timber since ancient times has been as a construction material, and it is still nowadays preferred over more modern building materials in a lot of instances due to a better life-cycle assessment, greater energy efficiency, lower costs and near-to-zero waste by-product [136].

Wood, bamboo and reed represent valid alternatives to steel and concrete not exclusively for socio-economic reasons but also for their structural qualities [85, 88, 137-139]. Through a combination of high strength and lightness, wood-like materials are strong competitors to modern construction materials [136]. Natural hollow materials, such as bamboo and reed, have superior tensile and flexural strength than wood [85, 88, 139]. Regarding these distinctive features, the exploitation of the intrinsically superior strength of hollow materials in the creation of larger and complex artefacts can generate a new strong competitor in the roster of construction materials. Nonetheless, the bare mechanical properties of bamboo are superior to those of giant reed and reed is considered being a highly invasive and unwanted species [86, 139-141].

The first historical records of the use of giant reed (*arundo donax*) dates back to Ancient Greece [142]. Nowadays, limited applications use reed, i.e. biofuel [143], industrial cellulose source [142], reed wattle for structural purposes, biomimetic and technical textiles applications [130]. Because of its high biomass productivity [143], it can be exploited as a sustainable fast-growing and low-cost material [142].

The strength of *arundo donax* relies on its structural composition comprising cellulose fibres and hemicellulose embedded in a lignin matrix [86]. The cross-section analysis of reed culm showed a structure with a homogeneous density of fibres, which is increased in the cortical region being more rigid [86], showing mechanical properties superior of most type of woods [85]. Giant reed has developed, similarly to bamboo [87], an optimal stem structure, which is reinforced with internodes to overcome the weakness due to its hollow and slender conformation (i.e. Euler buckling) [141]. In fact, the internodes allow the giant reed to withstand high compressive and flexural loads, which would be impossible without their presence.

This work focuses on a novel chemical and structural modification to turn giant reed into an advanced material with extremely improved mechanical properties and higher stability under challenging

environmental conditions. Giant reed specimens were treated in an alkaline environment to decrease the concentration of lignin and enable densification [114, 144]. The removal of lignin and thermo-compression allowed to achieve a denser material with high structural performance [114]. Porosities occur because of the delignification process. We propose to exploit even these tiny spaces, filling them up with nanoparticles to make the material tougher.

Notwithstanding, several authors investigated the effect of inorganic nanostructured materials on wood or bamboo [121, 124, 125, 145]. In this work we propose to tailor the effects of densification by introducing selected nanostructured materials in the structure of giant reed, i.e. silicon carbide (SiC) and graphene oxide (GO). On the one hand, SiC is a well-known material for its unique mechanical strength, which was exploited to improve the mechanical properties of metals [146] and polymer composites [147]. On the other hand, GO flakes were chosen for its 2D structure with high aspect ratio exposing a high concentration of hydrogen bonds [148] to the cellulose/lignin layers present in the reed. The final yield of this process can further improve the strength and toughness compared to the same densified reed. The analyses carried out highlighted a significant increase in the mechanical properties of densified samples intercalated with nanoparticles, especially regarding stiffness, strength and toughness. The addition of nanoparticles in the densified reed resulted also in a reduced water uptake by the reed, which decreases its bio-deterioration [139, 149] and thus guarantee a longer lifespan. Furthermore, the densified and nanoparticles intercalation treatments strongly increased the fire-retarding properties of the native reed and the “thermo-indentation” resistance, measured by using a custom-developed technique.

## 4.1. Materials

All the specimens were extracted from the culm of giant reed. Their orientation was parallel to sclerenchyma fibres, and they were mechanically polished to a regular geometry (10x2x0.5 cm<sup>3</sup>). The cross-section of samples is perpendicular to the fibres' direction, while the lateral side is parallel to them. Then, the specimens were immersed in a re-fluxed boiling deionized water solution containing NaOH (2.5 M, Sigma-Aldrich) and Na<sub>2</sub>SO<sub>3</sub> (0.4 M, Sigma-Aldrich >98%) to partially remove lignin.

The exposition time was chosen according to the results achieved by Song et al., which showed that a decrease of about 50% in lignin content delivers the best mechanical properties [114]. Chemicals were removed from etched specimens by thoroughly washing samples in several boiling baths of deionized water, followed by washings with running deionized water. Chemically etched samples after delignification were dried overnight at 30°C.

Afterwards, three set of samples were prepared and each of them was subjected to a different treatment. The first reference set (labelled “D”) was immersed in water, the second (“D+SiC”) was intercalated with SiC nanoparticles (3C-SiC, water dispersion, purity > 99%, Tec Star) and the third (“D+GO”) with graphene oxide (GO, water dispersion 4 mg/mL, monolayer content > 95%, Graphenea) flakes. To this aim, giant reed specimens were immersed in SiC and GO aqueous solutions (both at a concentration of 1 mg/mL). Then vacuum was applied to remove trapped air inside samples and the solutions were vigorously stirred for 24 hours at room temperature. An autoclave treatment of 3h at 5 bar pressure followed. Lastly, while being still wet, each set was hot-pressed at 100 °C and 5 MPa of pressure for 3h. A Bench Press (2.5 Tons by Gibitre Instruments, Bergamo, Italy) was used to thermo-compress samples.

Properties of these samples are compared with two other sets: natural reed (labelled “R”) and natural reed subjected only to thermo-compression (“TC”) at 100°C under 5 MPa pressure for 3h, an intermediate treatment useful as a comparison as it is already implemented in the industry [88].

The morphology and chemical composition of specimens were analysed by SEM and Energy Dispersive X-Ray spectroscopy (EDX spectroscopy) techniques, by means of a cold cathode JEOL Microscope, model JSM 7401-F.

Microstructural studies were performed with Scanning Electron Microscope (SEM) and profilometer technique. KLA Tencor 6 profilometer was used to analyse the cross-section of the 5 set of samples and to reconstruct their 3D surface by merging line scans having a distance of 2 µm.

## **4.2. Structural modifications**

Sample morphologies were analysed by Scanning Electron Microscopy (SEM) and scanning profilometry to reveal the effects induced in the

internal structure of giant reed by the treatments applied. To this aim, specimens were embedded in epoxy resin and polished to obtain a macroscopically flat surface for both the cross-section and the lateral side. The profilometry analysis on the lateral face (Fig. 25) is very useful to evaluate the packing density of the internal parenchyma structure. These structures tend to collapse under the effect of the external pressure. The collapse is partial for TC reed (Fig. 25b) and it leads to a reduction in the lateral size of the cellular structure ranging from 65 to 46  $\mu\text{m}$ . Conversely, densified giant reed (Fig. 25c) show an almost complete collapse in parenchyma cells and their lateral size shrinks down to  $\sim 20$   $\mu\text{m}$ . Similarly, the effects of densification are also reflected on the roughness of the cross-section surface. Roughness was calculated with root mean square (RMS) on a wide area. Compressed samples are increasingly denser and more compact (Fig. 25b,c) than untreated reed (Fig. 25a). The roughness, quantified as the root mean square of the height, is reduced by 7-fold, from 2.68 to 0.36  $\mu\text{m}$  after densification. This reduction is mostly due to partial removal of the lignin that accounts for the soft part [150, 151] of the untreated reed matrix while, in the densified samples, stiff CMFs become the predominant component [150, 151]. As already noted for the collapse of parenchyma structures, thermo-compression represents a partial treatment. Indeed, the roughness is slightly reduced, from 2.68 to 2.44  $\mu\text{m}$ .

As just discussed, the different treatments have an effect on the structure of materials, and they involve a density change. The different mass densities are  $0.468 \pm 0.015$ ,  $0.804 \pm 0.086$ ,  $1.259 \pm 0.010$ ,  $1.265 \pm 0.035$ ,  $1.279 \pm 0.031$   $\text{g}/\text{cm}^3$  for untreated reed, TC, D, D+GO and D+SiC specimens, respectively. It is worthy of attention that the density of D sample is still lower than that of cellulose [152], which ideally correspond to a complete densification and lignin removal. In fact, lignin is not completely removed in D and there are still some voids after densification. Moreover, the densification treatment has proven to be very effective in the packing of internal structures since the density of D is 8% higher than single reed fibres [130]. The lower packing density of TC compared to D is due to the lack of the lignin removal process, which does not allow to achieve high levels of compaction during thermo-compression.

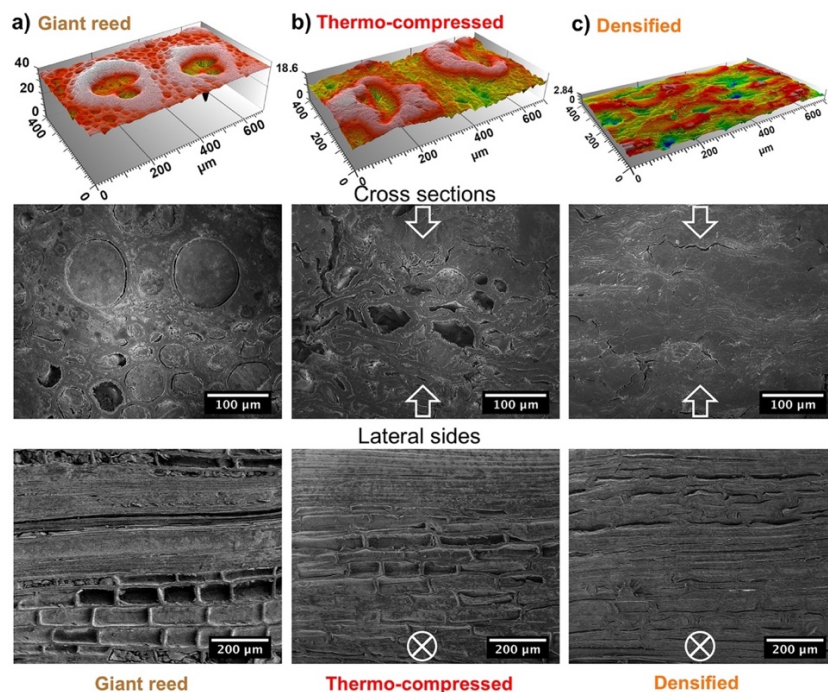


*Fig. 25 - SEM images of the cross sections and the lateral sides of a) R, b) TC, c) D. White arrows in SEM images show the direction of applied pressure in the thermo-compression treatment.*

SEM images (Fig. 25) give a clear focus on the various extents of collapse associated with the different treatments that were performed. The first row of SEM images shows the cross sections, the second row shows the lateral side parallel to CMF. The collapse in the internal structures increases going from left (R) to right (TC, D). We found that the densified reed (Fig. 25c) has a far more compact and ordered structure than natural reed, but there is still a presence of some voids between cellulose microfibrils (CMFs), which are of approximately several microns long and hundreds of nanometres thick. Both the compact structure and the presence of small voids have a crucial importance for the intercalation of the nanoparticles and their cross-linking with the surrounding CMFs.

By comparing SEM micrographs of TC and D (Fig. 25b,c), it can be clearly seen that TC is less dense than D, while TC still maintaining a structure similar to the untreated reed. This resemblance disappears in D, D+GO and D+SiC (Fig. 26) where the structural features of the starting material (R) cannot be distinguished anymore.

This similarity disappears in D, D+GO and D+SiC where the structural characteristics of the source material (R) are no longer observable. Fig. 26 shows cross-section SEM images of the D, D+GO and D+SiC samples, at various magnifications. SiC nanoparticles and GO flakes filled the voids in the D sample (Fig. 26), as initially supposed, forming thin layers at the interface between CMFs.

### 4.3. Nanoparticles inside cellulose-based structures & Chemical analysis

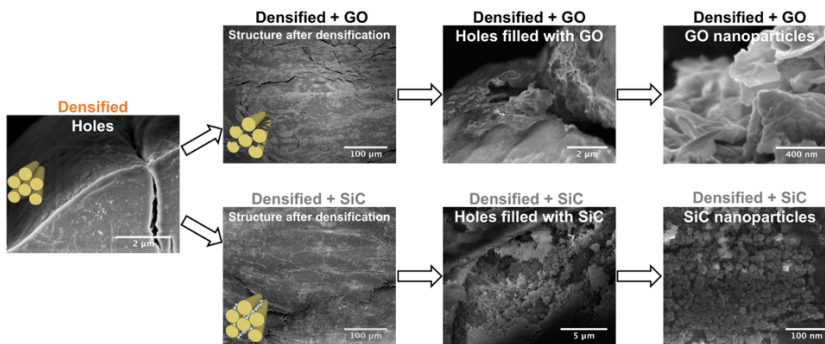


Fig. 26 - SEM images of the cross-section of D, D+GO and D+SiC specimens. The second column displays the D+GO and D+SiC samples after nanoparticles intercalation and densification treatments: there is no evident morphological difference between the two. The third and fourth columns show zoomed details of the location of nanoparticles at the interface of CMFs.

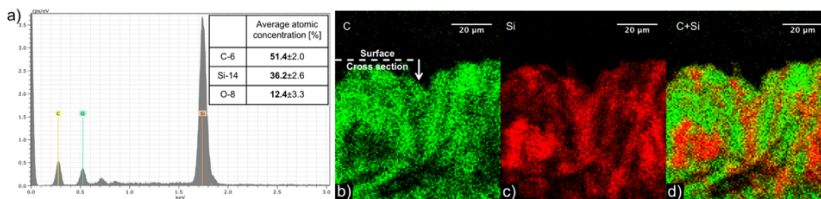
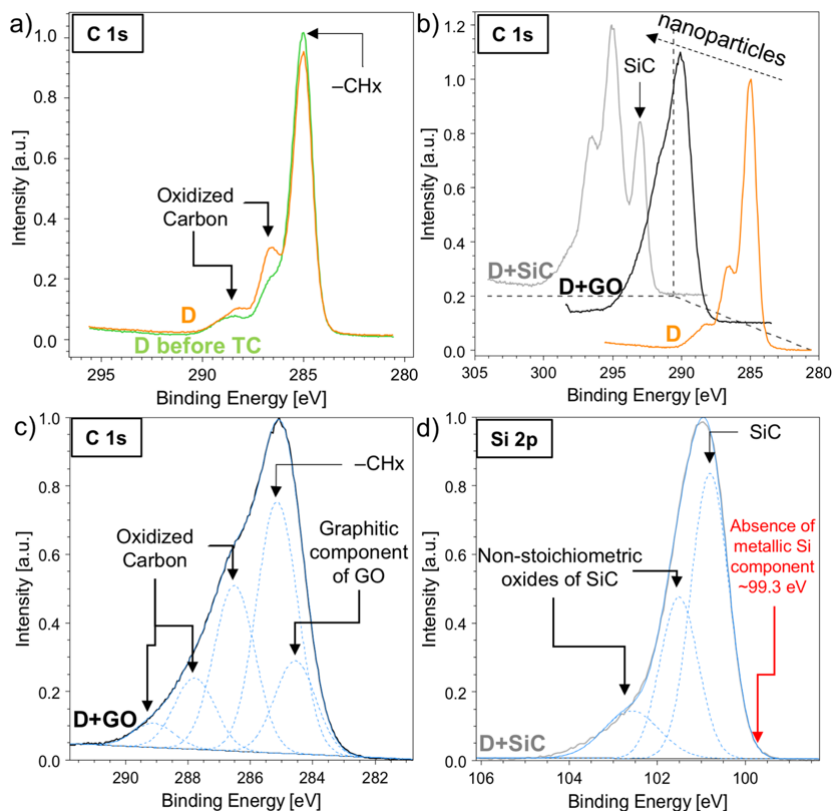


Fig. 27 - EDX analysis: **a)** EDX spectrum performed at 10 keV. The table reports the average quantitative elemental analysis of C,Si,O from three different wide scans sampled next to the surface in SiC-rich regions. Maps of the atomic percentage of the cross-section of D+SiC specimens: **b)** C **c)** Si **d)** C+Si.





*Fig. 28 - XPS analysis of the a) thermo-compression treatment on lignin etched reed, b) nanoparticles intercalation on densified reed; c) GO flakes and d) SiC nanoparticles intercalation in the densified reed.*

Energy Dispersive X-ray (EDX) analysis was carried out to investigate the distribution of Silicon in the D+SiC specimens. Both atomic concentration spectra (Fig. 27a) and atomic distribution maps (Fig. 27b,c,d) have been collected to quantify the percentage of silicon carbide on the specimen surface and its distribution in densified giant reed as a result of SiC intercalation. As it can be seen through EDX signal, the atomic concentration of Si was about 36% at surface (Fig. 27a). SiC nanoparticles penetrated the D+SiC sample through the surface and naturally their concentration at surface is higher than in the bulk (Fig. 27c). Whereas a rough estimate of the concentration of nanoparticles, calculated from density changes, yields  $\sim 0.9$  wt% for both D+GO and D+SiC samples.

For the other samples, EDX analysis cannot provide meaningful insights since they are mostly composed of carbon, oxygen and hydrogen. The sensitivity of EDX technique is not enough to precisely

quantify elements with such low atomic numbers. Therefore, the XPS analysis was carried out to have a broader view of the chemical composition, owing its higher sensitivity than EDX analysis vs C and O atoms and the possibility to investigate chemical bonds.

The chemical composition of the virgin and treated samples was examined also by XPS. The analysis was performed using an Axis DLD Ultra from Kratos (UK-Manchester) and consists the acquisition of a wide spectrum at a pass energy of 160 eV to detect all the chemical elements constituent the sample surface. Then core lines of interest were acquired at a higher energy resolution using a pass energy of 20 eV. Since samples are non-conductive, charge compensation was needed. Optimal conditions of compensation were obtained minimising the full width at half maximum of the core line peaks and maximising their intensity. This leads to an energy resolution of  $\sim 0.3$  eV. Finally, data reduction was performed using a software made in-house based on the R platform [153]. For each core line a linear background subtraction and Gaussian components were used for peak fitting.

Samples after delignification and after densification were compared to evaluate the effect of the thermo-compression treatment on the material (Fig. 28a). Thermo-compression induces a slight conversion of  $-\text{CH}_x$  into epoxy, alkoxy and carbonyl components (Fig. 28a) in the delignified reed. We suspect that alongside delignification, there is a decrease in crystallinity of cellulose (see Fig. 29), owing the alkaline environment [154]. According to delignification treatment optimized by Song et al. [114], which was here applied on giant reed, revealed 12% reduction of the cellulose content, while hemicellulose was decreased 4-fold.

Fig. 28b shows different bonds in densified reed after introducing the GO flakes and SiC nanoparticles. D+GO spectrum shows a graphitic shoulder at binding energies lower than  $-\text{CH}_x$  bonds. As well as, an increase in all the oxidised carbon components (C–O, C=O and O=C–O) can be assumed from Fig. 28c. By adding SiC nanoparticles, a new peak arises at  $\sim 283$  eV, as shown in Fig. 28d for the Si 2p line. Presence of GO flakes, when compared to D spectrum (Fig. 28c), generates a significant increment of all the oxidised carbon components (Fig. 28d) in the overall structure of densified reed. There is also the rise of a graphitic shoulder  $\sim 284.6$  (Fig. 28c) owing to the molecular structure of GO flakes.  $\text{Si}^0$  component, which should fall at  $\sim 99.3$  eV (Fig. 28d), is absent and the narrow peak of SiC (Fig. 28d) demonstrate that SiC nanoparticles are crystalline. In addition, some native oxides are formed on the surface of SiC nanoparticles, as denoted by the presence of the

non-stoichiometric oxide components in the Si 2p XPS spectrum (Fig. 28d).

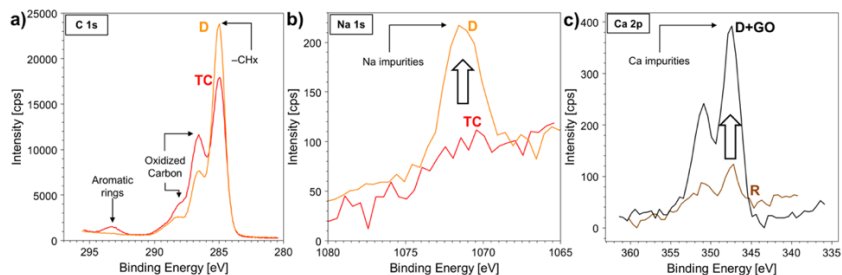


*Fig. 29: a) The difference in XPS spectra between TC and D shows the effects of delignification. TC and D samples differs only for the delignification process. b) presence of Na impurities. They are increased after the chemical etching c) presence of Ca impurities. They are increased from <0.1% to ~0.5% after the chemical etching. Ca impurities have an important effect on the D+GO as they interact with GO during burning.*

The binding energy that is associated with the structure at  $\sim 294.3$  eV in the C1s spectrum of “TC” in Fig. 29 has energies that are too high to justify the bonding of carbon with any element. It could instead be explained with a shake-up structure that is formed due to the presence of aromatic rings. This structure appears only in R and TC, and it disappears in all the other specimens, which were subject to delignification process. Thus, it could arise from the aromatic rings in the molecular structure of lignin [155]. As Fig. 29 shows, delignification took place going from TC to D and this corresponds with the decrease of the structure at  $\sim 294.3$  eV. However, the decrease of this feature is not enough to explain the increase of the component associated with  $-\text{CH}_x$  at 285.5 eV [156] to the detriment of the oxidised carbon that occurs as a result of the chemical delignification process.

A possible concurrent phenomenon is the degradation of hemicellulose and cellulose [81]. Indeed, alkaline treatments on wood-like materials remove part of the lignin and partially depolymerize hemicellulose and cellulose [75]. The subsequent degradation is turned into an extraction of the different sugars forming hemicellulose or the glucose from cellulose. In particular, in solutions with increased alkalinity, the extraction of glucose from the depolymerization of cellulose in natural fibres is increased [157]. This extraction can reduce the overall amount of oxidised carbons.

## 4.4. Mechanical properties

The evaluation of treatments' effect on the mechanical properties are analysed in this section. The stress-strain curves of the uniaxial tension test are reported in Fig. 30a,b. It is worthy of attention that flexural properties follow the same trend of tensile tests, as shown in Fig. 30.

Mechanical properties were measured with a displacement controlled, electromechanical testing machine from Messphysik Materials Testing (MIDI 10). The speed of each test was computed to get the same strain rate in both the tensile tests and the lower fibres of samples under flexural loading.

The Young's Elastic Modulus was calculated for all samples in the same deformation range, from 0.025% to 0.075%, which displays a linear elastic region for all samples. Stress-strain curves are reported until fracture.

Flexural tests were carried out with a three-point bending setup. The span length between the two support cylinders was 19.2 mm, this distance was increased to 50 mm for natural bamboo to fulfil the geometry requirements of the ASTM Standard D790 - 17. The cross-head speed was computed to obtain a suggested 0.01 mm/mm/min of strain rate on the outer fibre of the flexural samples. Flexural stress-strain curves are reported until the maximum load.

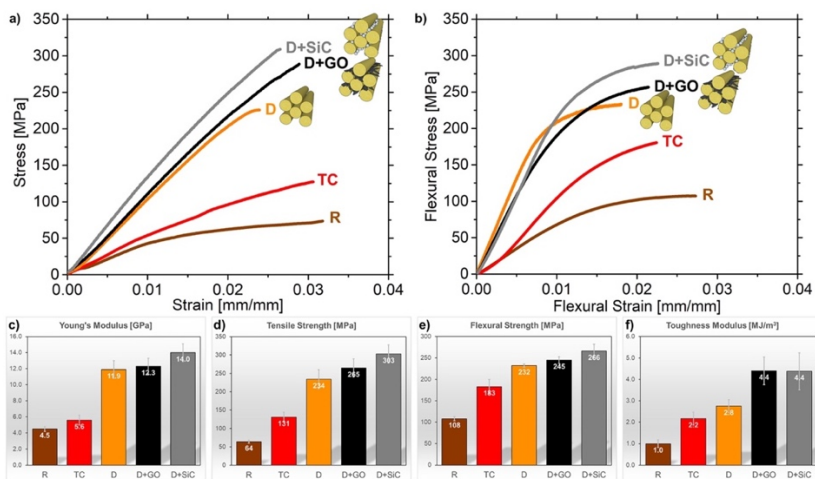
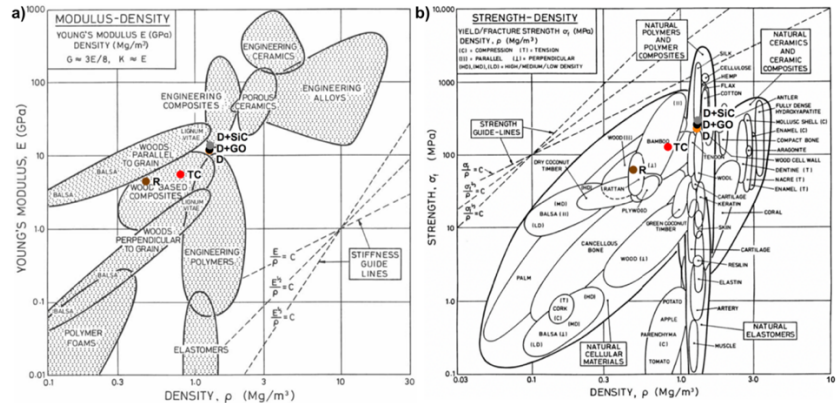


Fig. 30 - Average representative a) stress-strain and b) flexural stress-strain curves. Histograms summarizing the properties of R, TC, D, D+GO and D+SiC samples: c) Young's modulus, d) tensile strength and e) flexural

strength and **f**) toughness modulus, which was calculated from the tensile tests. Error bars represent the standard deviation.



*Fig. 31 - Material properties charts show the 5 materials of this work compared to common engineering materials: **a**) Young's Modulus vs Density chart and **b**) Strength vs Density chart - adapted from [85]. In the Ashby charts, the final densified products sit above the strength and stiffness guidelines traced using reed as the reference point.*

From the stress-strain curves (Fig. 30a) we computed a Young's Modulus for the giant reed of 4.5 GPa (Fig. 30c), which agrees with the measurements of Speck et al [158]. After densification, stiffness rises to 11.9 GPa and likewise the tensile and flexural strengths results in a drastic improvement of 3.66 times for the tensile strength (from 64 MPa in R to 234 MPa in D, Fig. 30d) and 2.15 times for flexural strength (from 108 to 232 MPa, Fig. 30e). Hence, the obtained performance of densified reed is superior to regenerated cellulose films [159] and very similar to both those of isolated reed fibres [130] and cellulose nanopaper [134]. Moreover, the properties achieved through densification are superior to many types of bamboo [88, 139, 160], resulting in a highly competitive construction material (Fig. 31a,b).

Introducing nanomaterials grants an additional boost to the performance of densified reed. Indeed, the Young's Modulus rises to 12.3 for D+GO and 14.0 GPa for D+SiC (Fig. 30c), which are higher than most engineering polymers (Fig. 31a). So, these materials moved from the wood's group in the Ashby chart (Fig. 31a) to engineering composites. Accordingly, both tensile strength (+13% for GO and +30% for SiC) and flexural strength (+5% for GO and +15% for SiC) are improved (Fig. 30d,e). These enhancements in mechanical properties are caused by the addition of nanomaterials, which improves the interfacial adhesion between CMFs. Densified nanocomposites fall into the density category of biological materials designed to work under

tension, like tendons, but they show higher strength. As expected, the upper limit in terms of both density and strength for the nanocomposites is cellulose [73, 85], which is the strongest structural component of reed. However, their strength is superior to wood and plywood (Fig. 31b).

Nanoparticles improved the deformation capabilities in bending (+10% for D+GO and +20% for D+SiC, see Fig. 32). Composite wood-like structures have a predominant deformation by shear, which is concentrated in the soft matrix [161], rather than on the stiffer cellulose fibres. It is clear that, with a partial removal of the lignin and hemicellulose matrix, the deformation capabilities of reed are reduced [162]. Indeed, densified reed exhibits lowered strain to failure in both tensile and flexural tests (see Fig. 32). However, the intercalation of nanoparticles generates a remarkable increase of the materials' toughness modulus (Fig. 30f). It goes from 2.8 MJ/m<sup>3</sup> after densification, which is the current state-of-the-art process, to 4.4 MJ/m<sup>3</sup> for D+GO and D+SiC.

To further compare the mechanical properties of each material, the specific toughness modulus was taken into account. It is calculated by dividing the area under stress-strain curves (i.e. toughness modulus) by the density. As a result of the variations in packing density introduced by the treatments, specific toughness modulus is suitable to evaluate the intrinsic improvements in toughening efficiency rather than toughness modulus. This is due to the increase in the packing density induced by compression, owing a toughness modulus increase while the specific toughness modulus remains the same.

No marked difference in specific toughness modulus (see Fig. 32) surfaces in the three samples of reed, thermo-compressed and densified reed. Instead, the intercalation of nanoparticles acts as a further reinforcement on top of the previous densification treatments as it generates an improvement in the specific toughness moduli of +59% for D+GO and +56% for D+SiC (Fig. 32c). The toughening could be caused by the location of nanoparticles at the interface between CMFs (Fig. 26). Indeed, both SiC nanoparticles and GO flakes were intercalated into the pores of giant reed, which were opened through chemical treatment and then closed by thermo-compression (Fig. 25 and Fig. 26). It can be interpreted in terms of better interfacial adhesion or increased in the chemical cross-linking at the interface driven by the additional hydrogen bonds available from the GO structure [163] and the non-stoichiometric oxides shell (Fig. 28d) on SiC nanostructures [164]. Not to mention that the small amount of Ca impurities, which

was found into all the samples (see Fig. 29), was reported to have a beneficial effect on the chemical cross-linking between GO and cellulose [165], thus effectively enhancing the stiffness and the strength between GO layers [166]. It was also demonstrated that the densification process on wood at moderately high temperatures can lead to the formation of new hydrogen bonds between CMFs [114, 135], which is here favoured by a high degree nanofibres' alignment. The higher level of oxidation emerging from XPS analysis (Fig. 28a) and the formation of new hydrogen bonds leads to a highly densified material that is stronger than same sample compressed at room temperature.

As a result of the intercalation of nanoparticles, we estimated an average improvement of the interfacial fracture energy between CMFs that is  $1.28 \pm 0.33$  for D+GO and  $1.47 \pm 0.36$  for D+SiC, both compared to D sample (see Fig. 33). The fracture energy was calculated according to an analytical model [167] and it is proportional to  $\sigma^2/E \cdot R$ , where  $\sigma$  is the tensile strength,  $E$  is the Young's Modulus of the material and  $R$  is the radius of the CMFs.

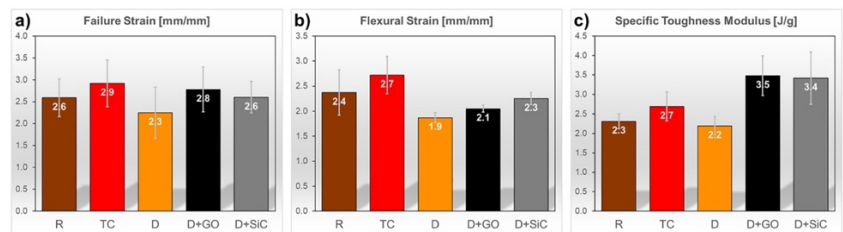


*Fig. 32 - Histograms summarizing the mechanical properties of R, TC, D, D+GO and D+SiC samples: a) failure strain, b) flexural strain and c) specific toughness modulus, which was derived from the toughness modulus as described in the article. Error bars represent the standard deviation.*

As for wood-like structures, the mechanical performance of densified and composite reed is dominated by the shear load transfer between cellulose microfibrils [161]. Thus, failure mechanics is prevalently governed by the shear failure at interfibrillar interface. Griffith linear elastic fracture mechanics have proven to be suitable describing the failure of adhesive joints subjected to complex loading conditions [168, 169]. It was suggested [167] that there is a correlation between the load necessary for the crack to propagate and the fracture energy of the interface joint. This insight could result in a better understanding of the adhesion in our nanocomposite materials. The microscale interactions

between nanoparticles and cellulose microfibrils can be treated within a precise geometrical configuration that is modelled to estimate the increase in toughness reported after the introduction of nanoparticles. We can imagine the interface as an adhesive joint that unbinds when crack propagates. Fig. 33 shows a hypothetical loading setup for a group of fibrils in mutual contact. An isotropic linear elastic behaviour is assumed for the materials involved, i.e. CMFs and interface materials. If the adhesive layer thickness  $h$  tends to zero, then the elastic strain energy absorbed by the layer is negligible. A full analytical derivation was proposed [167] for a similar geometry of concentric tubes joined by an adhesive at their interface and subjected to axial load. The link between critical load for crack propagation, adhesion and geometry holds to be:

$$N_c = \sqrt{4\pi R G_a \frac{E_2 A_2}{E_1 A_1} (E_1 A_1 + E_2 A_2)}$$

*Equation 23 - concentric tubes configuration: critical load for crack propagation [167]*

where  $A_i$  are cross-section areas,  $E_i$  are Young's moduli and their product represent the axial rigidity of tubular elements in tension and the internal element have radius  $R$  (Fig. 33a).  $N_C$  is the critical load for which the critical strain energy release rate  $G_a$  is reached. Equation 23 is applied to bodies #1, #2 in Fig. 33a where the body #2 is cylindrical and it could be extended to a modified configuration shown in Fig. 33b that resembles to the CMFs structure of D, D+GO and D+SiC.

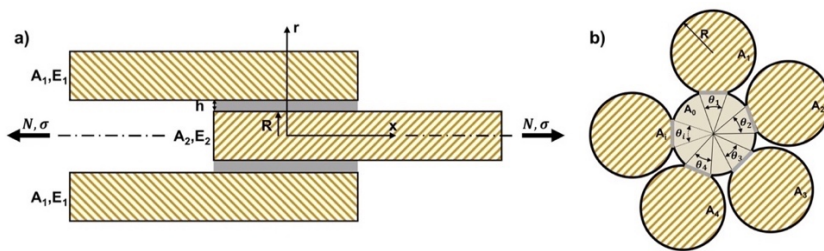


*Fig. 33 - a) Depiction of tubular adhesive joint subjected to axial load, simplified for a tube-cylinder circular and co-axial contact mediated by an adhesive film, in grey. b) Schematic representation of the cross-section of previous joint for the case of several identical aligned microfibrils with partial adhesive contact described by  $\theta_i$ .  $A_i$  are the cross-sections of the CMFs surrounding the central one, they have an Elastic Modulus of  $E_i$ . This configuration is depicting D, D+GO and D+SiC sample.*



D, D+GO and D+SiC have equivalent cellulose microstructures (Fig. 26), thus the only structural differences can be found in the interface layer, where nanoparticles are located. The differences between the concentric tubular configuration presented in [167] and our systems lies in the area of contact between different CMFs that is partial but have multiple areas of contact and does not extend to the entire external surface as for the tubes (Fig. 33).

We propose to estimate if the nanoparticles at the CMF interfaces generate an increase in critical strain energy release at the microscale which could cause the macroscopic enhancements in the stress of failure and toughness modulus in the D+GO and D+SiC samples (Fig. 30). Passing from a discrete analytical to a local model requires to substitute the axial force  $N$  with a constant distributed pressure  $\sigma$  on the  $x$ -axis that is generated as a consequence of the uniaxial tensile load conditions. The two models are linked if a catastrophic failure of the samples is considered. In particular, the bulk material exhibits a stable crack propagation when the applied load  $\sigma$  reaches a critical load  $\sigma_c$ , which is computed as the tensile strength of the mechanical tests.

Taking into account these considerations, Equation 23 can be rewritten to better suit the configuration of CMF in cellulose nanocomposites. The partial contact between CMFs is depicted in Fig. 33b where the central fibril is in contact with multiple fibrils, each for an arc of  $\theta_i R$ . As the nanoparticles are filling vacancies inside the structure, the key in comparing different samples is that the contact area between microfibrils remains unchanged in D, D+GO, D+SiC, hence nanoparticles play a role only in the determination of fracture energy  $G_a$ . Comparing the results with the analytical case in , we can consider crack nucleation to be a statistical phenomenon since the problem is symmetrical. This scrutiny implies that two terms in the ratio between axial rigidities in Equation 23 can indifferently be inverted and thus the ratio can be considered equal to 1 for cellulose nanocomposites. Finally, the following correlation is obtained:

$$\sigma_c \propto \sqrt{\sum_i (\theta_i R) \cdot G_a \cdot [E_0 A_0 + \sum_i (E_i A_i)]}$$

*Equation 24 - microfibrils configuration: proportionality between the critical stress to have crack propagation and structural parameters*

Equation 24 links the failure strength to the critical value of strain energy release rate ( $G_a$ ), i.e. fracture energy of the interface, for which the crack propagates [167].  $E_i$  and  $E_0$  are to be considered identical since

the load bearing structure of the composite is the same, so they can be reduced to  $E$  and extracted from the summation. To compare different sample groups (D, D+GO, D+Si), a second index  $j$  is inserted to label the quantities dependent on the three groups.

$$\sigma_{c,j} \propto \sqrt{\sum_i (\theta_{i,j} R_j)} \cdot \sqrt{\sum_i A_{i,j}} \cdot \sqrt{E_j G_{a,j}}$$

*Equation 25 - microfibrils configuration: proportionality between failure strength and structural parameters*

The first two terms in the product in Equation 25 are identical under the hypothesis of identical configuration and microstructure, therefore the relation can be rewritten as follows:

$$\sigma_{c,j} \propto \sqrt{E_j G_{a,j}}$$

*Equation 26 - tensile strength  $\sigma_c$  as a function of  $E_j$ ,  $G_{a,j}$ , which are sample-related values.  $E_j$  was computed as the elastic modulus measured upon tensile testing for each sample*

Then, the average improvements in interfacial fracture energy for the two set of nanoparticles can be computed:

$$\frac{\bar{G}_{a,D+GO}}{\bar{G}_{a,D}} = \frac{\bar{\sigma}_{c,D+GO}^2}{\bar{\sigma}_{c,D}^2} \cdot \frac{\bar{E}_D}{\bar{E}_{D+GO}}$$

$$\frac{\bar{G}_{a,D+SiC}}{\bar{G}_{a,D}} = \frac{\bar{\sigma}_{c,D+SiC}^2}{\bar{\sigma}_{c,D}^2} \cdot \frac{\bar{E}_D}{\bar{E}_{D+SiC}}$$

*Equation 27 - two ratios  $G_{a,D+GO}/G_{a,D}$  and  $G_{a,D+SiC}/G_{a,D}$  represent the average interfacial fracture energy improvements for the 2 sets of nanocomposite reed.*

The average interfacial fracture energy improvements for D+GO and D+SiC samples are linked with the average failure stress  $\sigma_{c,j}$  and elastic modulus  $E_j$  of each set of samples. The results show that the intercalation of GO the interfacial fracture energy is improved by 28%, and by 47% after SiC intercalation.

<b>Interfacial fracture energy improvements</b>	
$\frac{\bar{G}_{a,D+GO}}{\bar{G}_{a,D}}$	<b>1.28±0.33</b>
$\frac{\bar{G}_{a,D+SiC}}{\bar{G}_{a,D}}$	<b>1.47±0.36</b>

*Table 5 - Interfacial fracture energy improvements for D+GO and D+SiC samples.*

In summary, the estimation of the interfacial fracture energy improvements in Table 5 are in line with the results of the mechanical tests that show a higher tensile and flexural performance after the intercalation of SiC nanoparticles rather than GO. Finally, a linear correlation is obtained between elastic strain energy release rate and toughness modulus reported in Fig. 30f.

## **4.5. Burning, thermo-indentation and water absorption**

Two different tests were performed to evaluate the burning resistance of the samples: a free flame burning test and a thermo-indentation. A modified Taghiyari method [145] was used to perform free flame burning test.

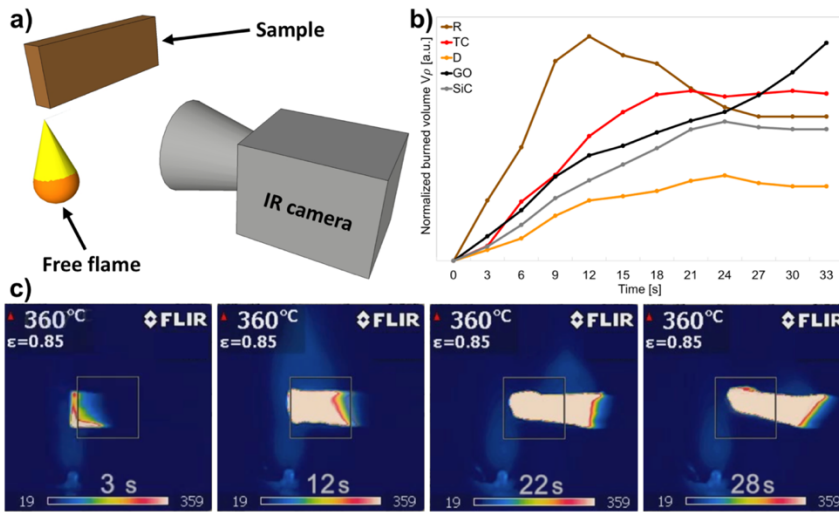


Fig. 34 - a) Schematic representation of the burning test setup. b) Burning test results of all specimen types. c) Time evolution of thermal imaging data from D+GO sample (Complete Videos are available by email).

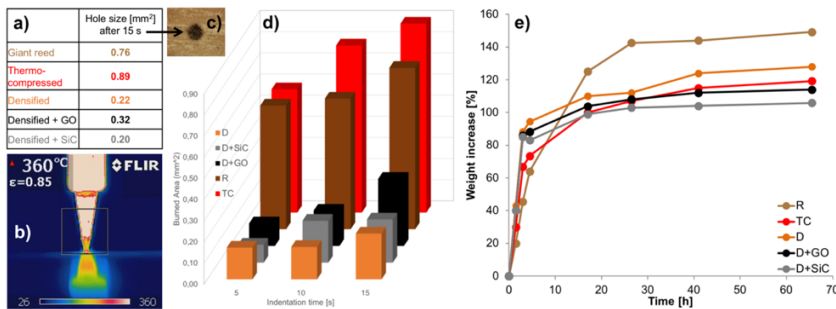


Fig. 35 - a) table showing the burned area after the 15s of thermo-indentation b) thermographic image of the indenter tip c) burned area results of all specimens when subjected to 5, 10 and 15 seconds of thermo-indentation d) burned area vs indentation time e) Accelerated humidity absorption tests carried out on R, TC, D, D+GO and D+SiC specimens. The graph represents the weight increase of samples vs. exposition time at constant 97% of relative humidity.

Fig. 34b shows the comparison between all the samples. Burning test were performed using a modified Taghiyari method [145] and a thermographic camera. The classical Taghiyari method has been modified to better fit the thermographic inspection of the process, and a Bunsen type burner was used to generate the free flame. The wood

samples were placed perpendicularly to the floor, at 90° respect to the flame direction, with the width facing the camera and the thickness directly above the flame. The normalized burned volume was computed according to Equation 28.

$$V_{\rho}(t) = \frac{A \cdot d(t)}{\rho}$$

*Equation 28 -  $V_{\rho}(t)$  is the normalized burned volume,  $A$  and  $\rho$  are the cross-section and density of the sample, and  $d(t)$  is the flame advancement and was computed considering the area having a sample temperature higher than 360°C (Fig. 34b).*

In order to be able to cross compare the calorific value of samples with different microstructure, the burned volume was normalized by the density since the calorific value is related to sample mass, hence to the density if a constant volume is considered.

The normalized burned volume is calculated as reported in the Methods section. During the first half of the test the reed burns faster than its compressed and densified counterparts, then it auto-extinguish itself faster than TC sample. Regarding the overall resistance to free flame, the densification treatment yields the best results as it performs almost twice better than all other samples.

All samples showed fire extinguishing properties, graphs in Fig. 34b. The only exception is D+GO. After about 20s, where all curves start to slow down, the specific burned volume of D+GO accelerates again. This effect cannot be entirely attributed to the high thermal conductivity of GO. In fact, DSC and TGA curves of GO [170] show a strong exothermic reaction at about 200°C, the energy release associated with it can drive flame propagation and accelerate the burning of the sample depicted by the black line in Fig. 34b. Furthermore, the Na impurities that remain into the structure after the delignification process (see XPS spectra in Fig. 29) interact with GO flakes to accelerate the burning mechanism [171]. In general, the introduction of nanoparticles seems to reduce the flame retarding properties that the densified (D) shows compared to untreated reed (R).

Ignition of wood can result from free flame or contact with a hot body. An ad-hoc thermo-indentation test was designed to quantify the resistance of each samples to burn in contact with a hot body.

Thermo-indentation tests were performed using a hot conical tip indenter (17.7° apex angle) at 400°C. The indenter was placed perpendicular to the lateral surface of the surface with an indentation

force of 0.65 N for 5s, 10s and 15s. The burned area was calculated from the images of samples' surfaces.

The thermo-indentation was performed using a hot tip perpendicular to the surface (Fig. 35b). The burned area from the tip was used to evaluate the data (Fig. 35c). These measurements depend both on the specific burning features of the samples and on the elastic modulus of the surface of the indented sample. The thermo-indentation performance can be explained cross comparing the data of the specific burning test with the elastic modulus. In fact, both reed (R) and thermo-compressed reed (TC) have higher indentation area, in particular the TC shows a higher burned area compared to R (Fig. 35d). Furthermore, the densified and nanocomposite reed have a lower burned area than both TC and R, according to both burning test and Young's modulus (Fig. 35d, Fig. 30c). Moreover, also during the thermo-indentation of the densified sample with GO nanoparticles, the burned area saw an upright increment from 10 to 15 s that did not arise in the other samples (Fig. 35d). In conclusion, both graphs of free flame and thermo-indentation show similar trends, apart from D+GO in the burning test due to the aforementioned effect (Fig. 34b,c). All densified samples showed superior resistance to thermo-indentation compared to reed or TC, with D+SiC having the best resistance of all for longer times (Fig. 35d).

The humidity absorption characteristics of the reed samples were calculated by the percentage of weight gain at different times. Accelerated humidity absorption tests were performed in a climatic chamber with controlled humidity  $97 \pm 1\%$  rH. The values of humidity absorption are reported in mass increase from dried state. At every sampling time 5 samples - one per set - were extracted from the chamber, transferred in a closed vial to avoid weight changes due to water evaporation and weighed.

Interestingly, the humidity absorption kinetics differs with the treatments applied (Fig. 35e). The two samples that contain all the lignin (R, TC) have a slower initial growth but have a high final steady state. The presence of lignin has a crucial impact on the water absorption since it is a cross-linked phenolic polymer with few terminal hydroxyl groups and low water solubility [154]. Therefore, when lignin is removed (D, D+GO, D+SiC), the water gain is faster but has a lower final asymptote. This finding is correlated with the higher packing density of cellulose microfibrils in densified samples and with the increased capillarity effect that is induced by the chemical treatment [172].

The asymptotic values, which samples approximately reach after 40 hours, have a maximum value of +150% for R that has the highest moisture absorption whereas they are significantly lower when nanoparticles are added: 114% for D+GO and 106% for D+SiC. The latter ranks as the lowest absorbing specimen (Fig. 35e).

In real-life scenarios the overall absorbed water is the key factor for the survival of wood and reed in critical environments. Less absorbed water will result in lower fungus development [149] and lower degradation in mechanical properties [139]. Thus, densified nanocomposite specimens will perform better under these conditions.

## 5. Wood transparency & conductivity

In this chapter, two experimental routes were followed, the first one towards wood transparency, the second to obtain a conductive wood composite (Fig. 36).

We chemically treated wood samples following the route for densification mentioned in chapter 4. This part of the activity served as to develop the technical skills required to replicate and then expand current state of the art in the literature regarding transparent wood composites [102, 103]. Indeed, the process involves technical difficulties mostly regarding (i) the bleaching treatment, which leaves a fibrillar material with little fibres' cohesion, and (ii) polymer infiltration. As they are mainly procedural and handling matters, they will not be mentioned for the sake of brevity within this thesis.

Then, the samples were subjected to organic solvents and impregnated with carbon nanotubes by vacuum infiltration. SEM observations of the treated samples showed the presence of CNT population throughout the entire cross section and a high local concentration on cellulose microfibrils. In order to achieve better dimensional stability, the modified wood samples were finally infiltrated with a transparent polymer. The holes in the cellulose structure were filled with epoxy resin to reduce the light scattering at the interface of cellulose microfibrils, thus improving the optical transparency of the composite material. Such obtained composite material was tested to measure the conductivity response upon flexural loading. It results that the I-V characteristic is unvaried as no significant resistance change is detected. Hence, the local observation of well distributed CNT population is indeed forming a continuous and stable network inside the material. The connectivity of the network remains stable during bending since stabilized by proper epoxy infiltration (Fig. 41). Finally, these experiments show how embedding conductive nanomaterials inside wood could be used for damage-sensing applications [173].

I have carried out this project during my visiting period at QMUL. The experiments presented in this chapter serve as proof of concepts of the feasibility of the ideas. In fact, I believe that more investigations are required before submitting a full journal paper.



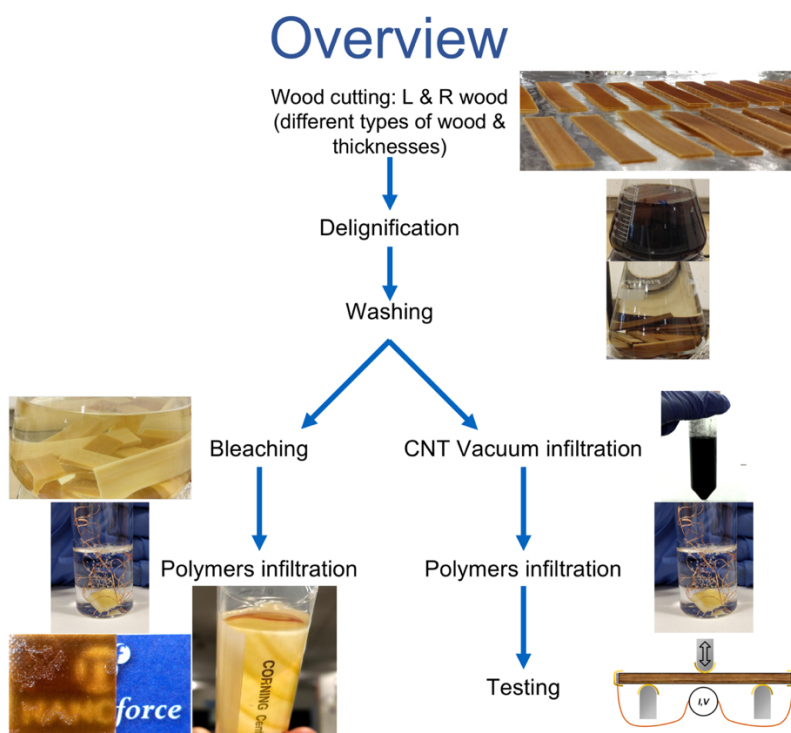


*Fig. 36 - Overview of the two experimental routes followed*

## 5.1. Materials

Several types of wood (Balsa, Basswood, Oak, Pine) were used to test and refine the delignification process, the bleaching and the polymer infiltration.

L-wood and R-wood was used. The notation [102] of L-wood includes samples where wood channels are parallels to sample's length. Whereas, R-wood is the wood cross-section where wood channels are perpendicular to sample's length. As shown in chapter 4.2 (Structural modification), the delignification treatment is needed to open up the internal wood structure and thus allow for CNT or polymer infiltration. All samples were de-lignified for either 7h (partial delignification) or 24h (complete delignification) in a mixture of NaOH (2.5 M, Sigma-Aldrich) and Na<sub>2</sub>SO<sub>3</sub> (0.4 M, Sigma-Aldrich >98%) in de-ionized water kept boiling in a re-fluxed flask. Successively several washing stages with boiling water to remove chemicals and reduce pH to neutral. Successively samples were bleached in a boiling DI water solution with 2.5M of H<sub>2</sub>O<sub>2</sub>. Finally,

samples were carefully rinsed with DI water and stored in ethanol. Experimental findings of the following sections are based on the dataset of basswood samples (L-wood and R-wood). Several solvents (water, ethanol, acetone, dimethylformamide and their mixtures) were used to disperse carbon nanotubes (CNTs) and minimize the use of CNTs required. Best performance both in terms of CNT solution stability and resulting penetration depth was obtained with DMSO. In order to achieve a well dispersed CNT solution, the CNT powder was dispersed into DMSO following a three-stage dilution process. Each stage consisted in a further dilution and energy probe sonication with a 1500J at 50% of magnitude. A final CNT concentration of 0.015mg/mL was achieved. Multi-walled Carbon nanotubes (MWCNTs) used in this study for conductivity purposes were the product NC7000 by Nanocyl (Belgium). The DMSO+CNT solutions were infiltrated with an accelerated vacuum infiltrated either on 1 or on both sides of the sample.

Two polymers were used for infiltration: PVP (1.3MDa, Sigma Aldrich) 15wt% in ethanol solution, as reported in [103], and a low viscosity epoxy resin (IN2 Infusion, Easycomposites, UK). Wood samples were placed in a sealed chamber and covered by epoxy or PVP solution, the pressure was decreased gradually up to 20-30 mbar. Resin curing for epoxy took place in a vented oven for 4h at 80°C.

Morphological studies were carried out using a scanning electron microscopy-SEM (FEI, Inspector-F) with acceleration voltages of 5 or 10 kV. Conductivity was measured with a two-point probe setup and three different configurations for the contacts (two of which yielding the same results for conductivity purposes) were tested as described in Fig. 42. The input voltage (V) was generated by a power supply (Agilent, 6614C) and varied in the range from 0 to 50 V while the current output was being registered by a pico-ammeter (Keithley, 6485).

Three-point bending tests were performed using a quasi-static mechanical tester (Instron 5566). The dimensions for the samples for flexural test were approximately 7.5x1.5x0.15 cm. The span length was 50.8 mm and a constant cross-head speed of 5 mm/min was used for cyclic loading. We investigated the effect of bending on the electrical resistance. The changes were measured with the external power supply while applying a DC voltage of 10 V between the two electrodes on the samples as depicted in Fig. 42.

## 5.2. Wood transparency

### 5.2.1. Bleaching and impregnation with polymers

Transparency in wood can be achieved with a chemical bleaching treatment, which removes lignin and transparent polymer infiltration. Polymer infiltration is not only important to improve transparency, but it is crucial to provide a stable structure for CNT network and sample's conductivity that we are interested in achieving. We found that PVP could only infiltrate depths of some hundreds of microns (Fig. 37a), lower than those reported in [103]. In addition, it yielded sufficient infiltration-quality only for thin samples of R-wood. High molecular weight of PVP was not the only factor in competition with infiltration. Solvent evaporation is not a secondary issue as 85% of the PVP solution will need to evaporate, leading to the creation of interfaces. Epoxy resins overcome this issue as they are not conveyed by means of a solvent and they cross-link on-site while having limited linear shrinkage (<3%) during curing [174]. Indeed, the ellipses in (Fig. 37c) show that there is no interface between cellulose and infiltrated epoxy so great surface finish can be achieved (Fig. 37d). The highest level of optical transmittance was visible for CNT in R-wood samples. Haze measurements [175] are to be performed.

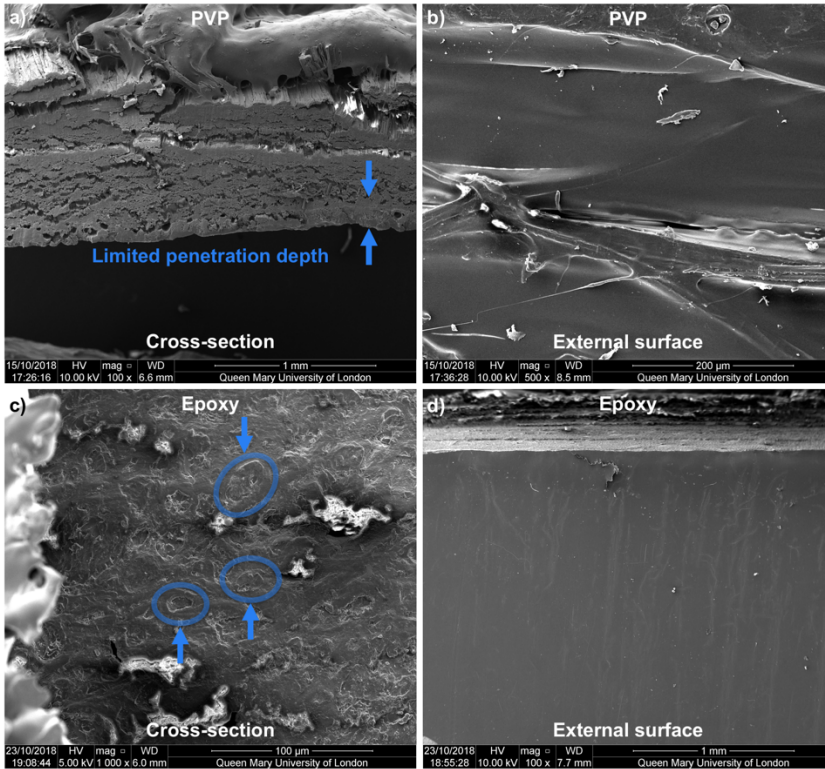


*Fig. 37 - a) PVP penetration depth into modified wood structure b) surface finish after PVP infiltration.*

*c) cross-section of R-wood sample after epoxy infiltration. Perfect adhesion between wood lumina and infiltrated epoxy as highlighted by the ellipses d) high-quality surface finish obtained after epoxy infiltration*

### 5.3. Wood conductivity

#### 5.3.1. Treatment of the internal structure & CNT vacuum impregnation

The best procedure for CNT infiltration was to perform a partial delignification without bleaching (see sample color in Fig. 43) since otherwise samples would gain in terms of transparency but they would become too fragile for the successive treatments (CNT infiltration and polymer infiltration) and handling.

We found that the fastest way to infiltrate wood specimens was through vacuum infiltration. Flat samples were placed on top of Büchner funnel with filter paper connected to a side-arm flask for solvent accumulation and to a vacuum pump. The liquid solutions were dropped from above

with a pipette in order to soak completely the sample. In order to evaluate the treatment-quality of CNT infiltration an experiment was designed where the sample was masked on the lateral sides so that the CNT could penetrate only through the top surface or by volume absorption. DMSO+CNT solution was able to penetrate the sample to a significant depth, results are reported in Fig. 39.

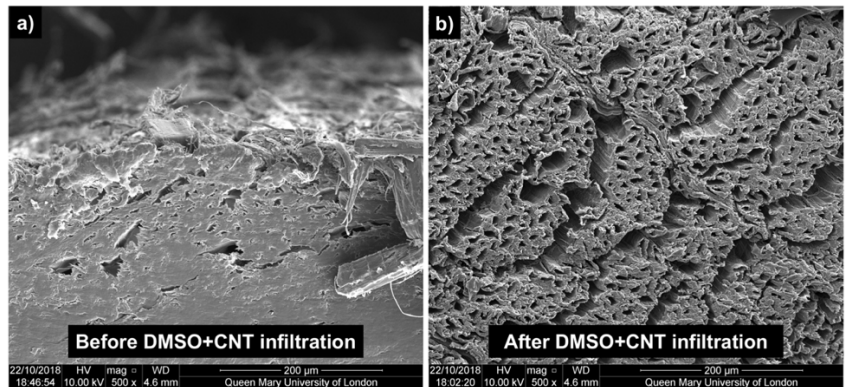


*Fig. 38 - Effects of DMSO treatment on the cellulose structure of wood*

The treatment with DMSO solution has two prominent effects on the wood structure: i) the internal wood porosities open up and cellulose fibrils became more exposed as displayed in Fig. 38 and ii) the depth penetration of CNT through the sample is drastically increased to at least 1 mm thickness inside wood (Fig. 39). On the other side, by handling the samples after this treatment we noticed a decrease in their flexural modulus (Fig. 45).

With a depth profiling after a physical cross sectioning of the sample, we were able to follow the presence of the CNT network as it penetrated the bulk of the treated wood samples (Fig. 39).

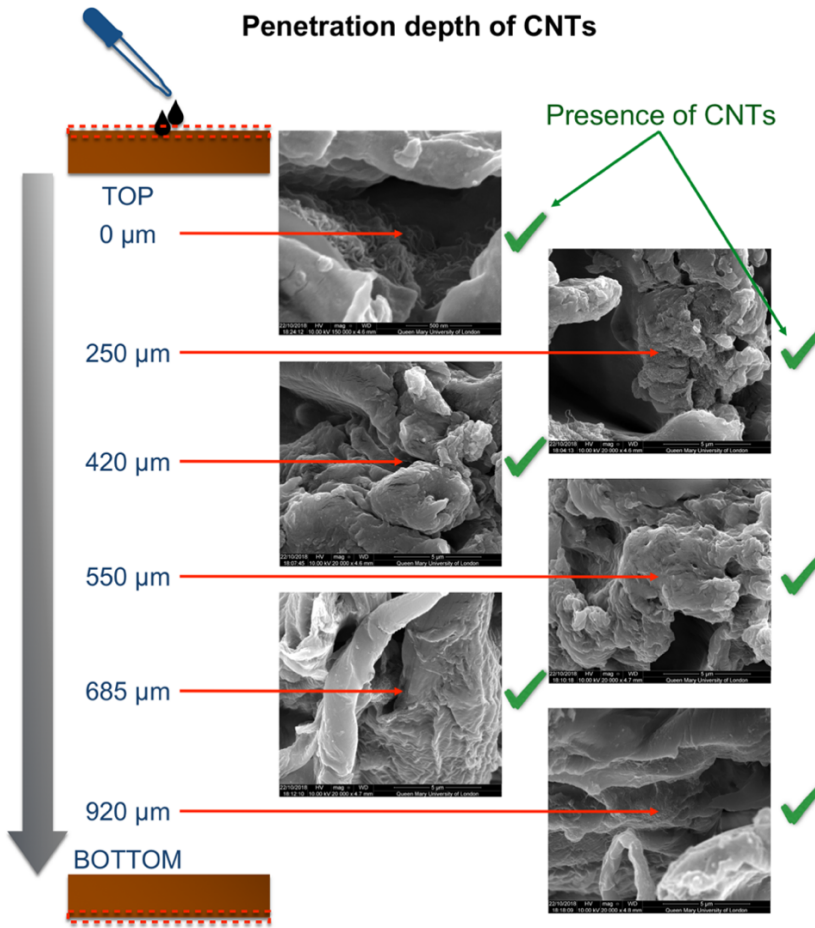


*Fig. 39 - CNT penetration at different depths*

To achieve this goal, in the sample whose tests are shown in Fig. 43 & Fig. 46, 15  $\mu\text{g}$  of CNTs were infiltrated on each of two larger surfaces of the sample, having an exposed area of 11.84  $\text{cm}^2$ . This holds a CNT consumption of 25  $\text{mg}/\text{m}^2$  of product. Considering a price of  $\sim 100$  €/g for high quality CNTs and  $\sim 20$  €/L for DMSO, the manufacturing cost of the vacuum infiltration treatment on both sides results to be 36 €/m<sup>2</sup> and CNTs account just for 7% of the cost. This cost could be even lower if industrial material grades are used instead of high-quality research grades or if the treatment applied just to one of the two surfaces.

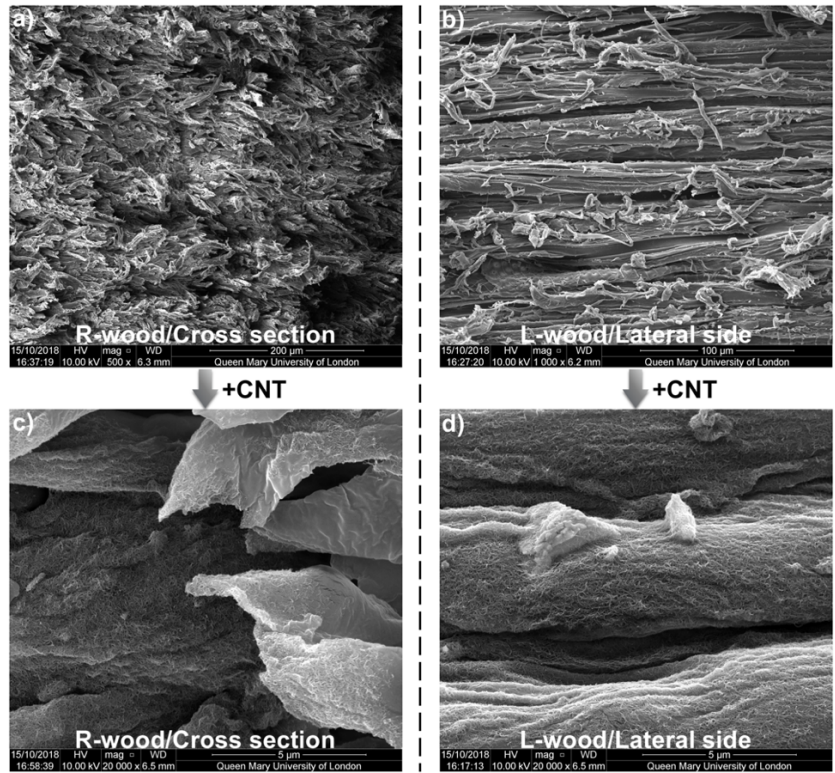


*Fig. 40 - a) microstructure of the cross section of R-wood and b) the lateral side of L-wood. The same structures with a highly dense network of CNTs in c) R-wood and d) L-wood that will act as conductive pathways*

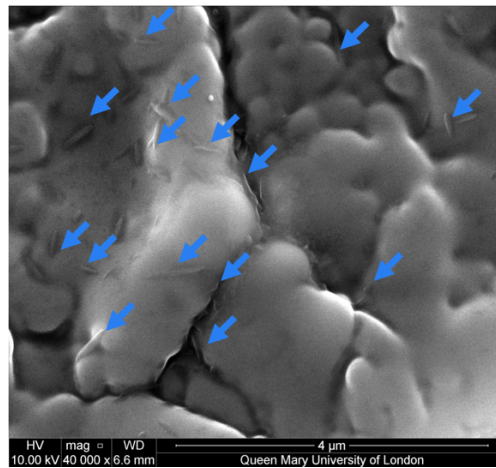


*Fig. 41 - arrows show the CNT network that is revealed under the surface of epoxy in the conductive wood composite*

### 5.3.2. Variation of conductivity during cyclic flexural testing

With a three-point bending setup, tests were performed with different contact positioning: (i) on the cross-section, (ii) on the bottom surface of the sample that is in tensile configurations and (iii) on the top surface of the sample in compression configuration (Fig. 42). These contact placements were chosen to test the changes in measured current, i.e. electrical resistance or conductivity, and some hypothesis on the internal CNT network.

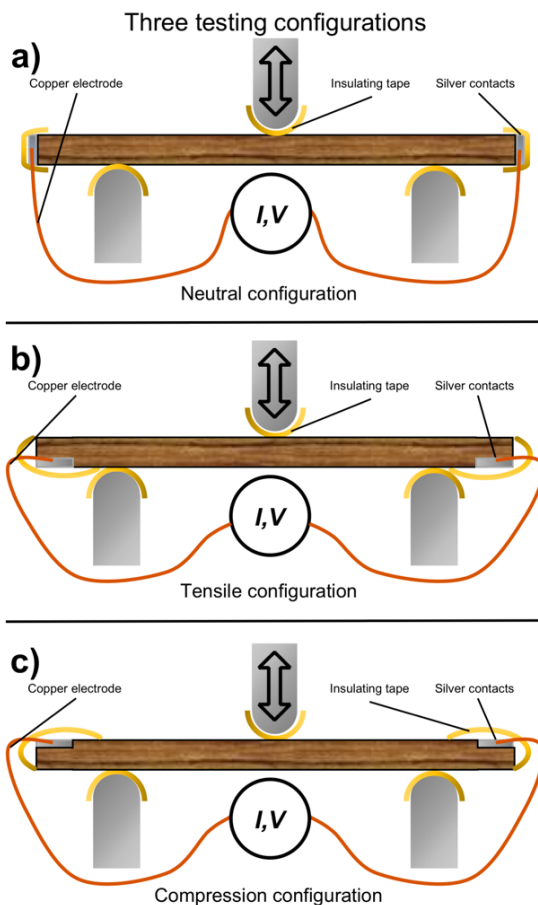


*Fig. 42 - three-point bending conductivity tests. 3 configurations were used. a) Neutral configuration with contacts placed at the median line b) Tensile configuration c) Compression configuration. The only difference between the last two configurations is the upside-down positioning of the sample.*



The linearity of the I-V characteristic of the conductive wood composite is a perfect ohmic conductor within the wide range of applied voltage (from 0 to 50 Volt), so we can write:

$$R = \frac{\partial V(I)}{\partial I}$$

*Equation 29 - The electrical resistance  $R$  is measured as the average slope from the I-V characterisations.*

$$\sigma = \frac{1}{\rho} = R \frac{A}{L}$$

*Equation 30 - The conductivity  $\sigma$  is the inverse of the resistivity  $\rho$ .  $R$  is the resistance,  $A$  is the cross-section of the sample and  $L$  is the distance between contacts.*

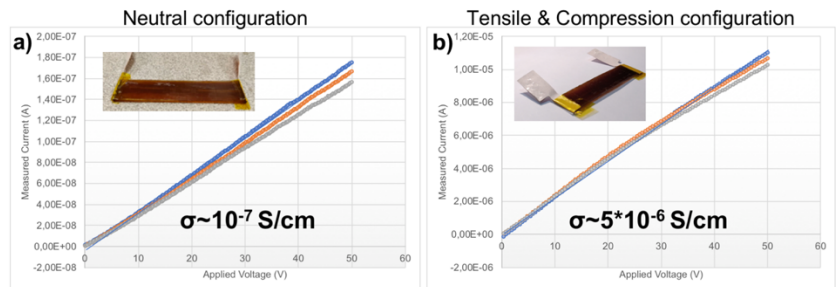


*Fig. 43 - Conductivity measurements of the sample tested in the three loading configurations: a) neutral configuration and b) tensile & compression configurations*

The addition of CNTs improved the epoxy+modified wood without CNTs that was also tested as a reference for conductivity but didn't yield any current (i.e. registered current was below the threshold of minimum detectable current  $< 10^{-10} \text{ A}$ ). Due to a different position of the electrodes, the conductivity improves 50 times between Fig. 43a and Fig. 43b. Indeed, the contact in the Fig. 43b was obtained by slightly grinding and sanding the surface of the resin to expose the internal cellulose & CNTs structure and the silver paste was applied directly. Then, as in Fig. 43a, copper conductive tape and the contacts were secured with insulating Kapton tape (Fig. 43).

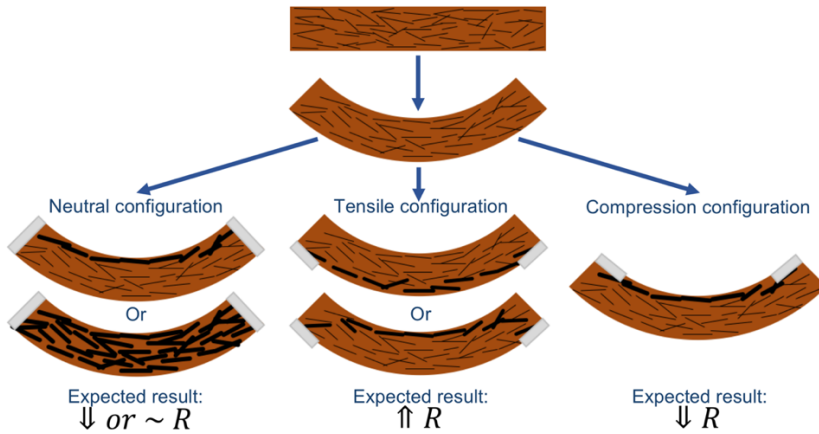


*Fig. 44 - Conductive wood composite beam tested in flexion with a representation of the embedded CNT network. Some logical hypothesis of the conductive pathways followed by the internal current for the three probing configurations and the foreseen changes in resistance,  $R$ , are reported. e.g. Due to compression on the upper surface, if the CNT path is expected to shrink, so should sample's resistance.*

If the CNTs were mixed and dispersed into epoxy and then infiltrated into cellulose-based structure, the percolation theory would apply and the foreseen changes in electrical resistance of Fig. 44 would be the output under bending for epoxy+CNT nanocomposites [176, 177]. These changes should resemble [177] the shape of the stress response in Fig. 46. Instead, an almost constant resistance is registered (Fig. 46) in all three configurations. A very slight decrease in the resistance over time is noticed, but it is independent on the loading configuration and load cycle. The quasi-constant conductivity with values in the range of Fig. 43, which are above those of other studies on epoxy+CNT network [178-181], could hint that the conductive wood composite is above the percolation threshold.

The amount of CNT infiltrated in the sample of Fig. 46 was  $30 \mu\text{g}$  in a total weight of  $1.9 \text{ g}$ , i.e.  $0.0016 \text{ wt}\%$ . Surprisingly, this concentration competes with the lowest percolation thresholds ( $\Phi_C$ ) ever recorded for CNT or graphene polymer composites [182-184]. It is lower than  $0.0025 \text{ wt}\%$  that we believe, to the best of our knowledge, being the current record for CNT+epoxy nanocomposites [179]. However, there are some PVC+MWCNT nanocomposites that score even lower values of  $\Phi_C$  [185]. Contrarily those studies where nanoparticles are mixed with polymers [178-184], our CNTs are not randomly dispersed into a polymer matrix but adhere to cellulose microfibrils. CMFs thus act as a substrate for the CNT network providing the conductive pathways [177]

and ultimately a very high local concentration Fig. 40 c,d. According to these results and the low current needs (Fig. 43), the conductive wood composite could be used as a low-power failure sensor.



*Fig. 45 - highly flexible conductive wood composite*

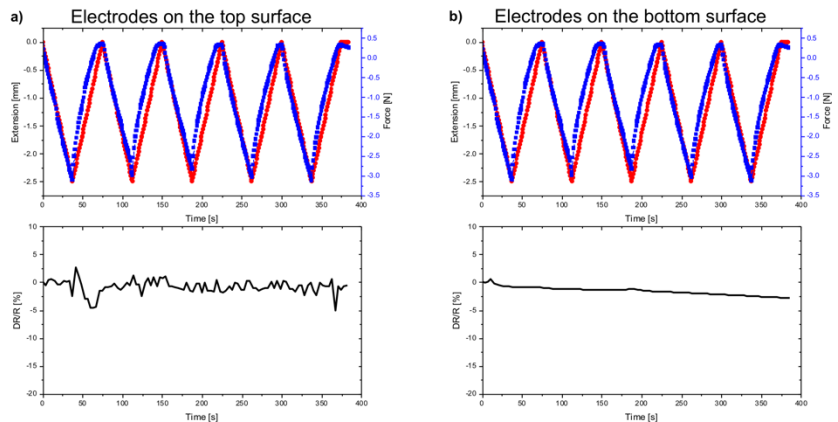


*Fig. 46 - Cyclic flexural loading, the input is the imposed deflection at the midpoint (in red), the output is the recorded load (in blue). The graphs on the below show samples' resistance changes (in black) during cyclic loading. **a)** electrodes on the top surface **b)** electrodes on the bottom surface. Note: the neutral configurations had the same outputs, i.e. no significant variation in resistance. However, during the cyclic loading it showed some sudden variations due to more delicate contacts.*

Furthermore CNT, are embedded into epoxy resin guaranteeing the stability of CNT network onto CMFs, lowering wear and possibility of dispersion of CNTs into the environment.

The CNT network act as an integrated sensing nano-material inside wood and has proven to be suited for structural health monitoring applications such as damage sensing [186]. Clearly, prior to the implementation in for SHM systems, it is required to understand how the failure modes or damage accumulation in this sensory network

affect the sensing performance. To the degree of beam deflections imposed in bending, the associated strain on the top/bottom surfaces is still small. Therefore, further experiments need to be performed at higher strains, e.g. in a tensile test, or bringing samples to failure.

Under the processing perspective, eliminating the separate infiltration process in favour of a direct CNT dispersion into the epoxy resin may result in very poor overall dispersion and the use of higher amount of costly CNTs. Furthermore, it might hinder the coupling with cellulose fibres and the filling of existing microcavities due to the rise in viscosity. The ideal way is to exploit the already present cellulose substrate that enables to create a locally high dense CNT network without the need of higher volumes of CNTs.

## 6. Final Remarks

The aspiration of my PhD activities was that of researching how superior properties can be achieved through processes and treatments embedding carbon-based fillers into engineering composites. Indeed, the analysis of the mechanical properties was at the heart of my activity, with an eye towards practical applications. This concept was developed with different approaches.

My main projects focused on PVDF and PVDF+GO electrospun fibres and nano-toughening treatment for wood-like specimens. The latter includes densification treatments and the structural wood modification that were utilized in a pilot project to study wood conductivity and transparency, which I carried out at Queen Mary University of London.

In the first part of the thesis, mechanical tests on graphene-based single electrospun composite fibres are reported. As it was previously demonstrated for bulk composites, we proved that the adhesion of the fillers has a strong impact on nanocomposite fibres and showed the effects of their addition on the microstructure of the fibres. PVDF and PVDF+GO fibres reached apparent toughness modulus values close to those of Kevlar fibres. Due to a hollow microstructure, which lowered the stress values, the real toughness moduli could be even higher. Furthermore, all the single electrospun fibres had superior deformability compared to previous literature studies, with an average strain at break of more than 400% for pure PVDF. All the investigated electrospun fibres showed high levels of energy dissipation, whose exploitation could be promising in high performance textiles. The mechanism of stable propagation of multiple necks is described. Multiple necking can fuse together and propagate along the entire length of the fibre as shown for drinking straws. A novel mechanical constitutive model is proposed in order to describe the mechanical performance of the electrospun fibres. The derived expression can be easily implemented in a FEM environment as the material constitutive law to simulate the behaviour of macroscopic structures (like ropes, textiles or bulletproof vests) where these fibres constitute its lowest hierarchical component. The small-scale phenomena were studied providing an analogy with macroscopic hollow structures represented by drinking straws. This analogy helped to cover all the missing pieces in the understanding of the deformation mechanics of electrospun fibres.

The other activities reported in this thesis revolve around treatments on cellulose-based materials. Indeed, wood treatments have recently gained new interest due to their potential application in timber housing. Moreover, the discovery of densification treatments has allowed wood to gain strengths comparable to that of metal alloys, hence the interest for densified wood or wood-like specimens. Those treatments can be beneficial also for other properties, such as conductivity, fire retardancy and improved mechanical properties.

In Chapter 4, we presented an innovative nano-toughening treatment for wood-like specimens that involves densification of cellulose fibrils combined with intercalation of GO and SiC nanoparticles. In particular, the process was here tested to improve the mechanical properties of an invasive plant, giant reed, into a stronger and tougher engineering composite.

Morphological and structural characterizations, performed by using profilometer, SEM, EDX and XPS techniques, highlighted that the treatment performed successfully intercalated the nanoparticles inside the densified giant reed. Although, nanoparticles led to no apparent influence on the cellulose structure of the densified reed, their presence and location at the interface of CMFs resulted in a better interfacial adhesion and overall improvement in mechanical performance, both for tensile and flexural properties. Indeed, the mechanical properties of the nanocomposite increase in respect of both the untreated and densified reed. The nanocomposite reed has a 1/15 of the elastic modulus and 1/2 of the strength of mild steel while having just 1/7 of its density. Further analysis highlighted that the nanoparticle intercalation in the densified reed enhanced the specific toughness modulus while this does not occur with the densification treatment alone. This result is due to the role played by nanoparticles during the relative sliding between cellulose microfibrils inside the material. A mechanical effect coupled with an increase in the chemical interaction could be at the root of this phenomenon. Indeed, the densification treatment involves the formation of a high number of hydrogen bonds between CMFs. The amount of these bonds could further increase by adding nanoparticles in the voids of the densified structure, especially with GO, which is rich of hydroxyl and carbonyl groups on its surface. Additionally, an increase in adhesion energy, that was estimated to be higher for SiC nanoparticles than GO, could induce an increased stress transfer between cellulose microfibrils.

Further investigations were performed to evaluate thermo-indentation and burning response of the materials. SiC and GO-densified giant reed have strongly increased fire-retarding and thermo-indentation properties compared to the native reed. Moreover, the addition of nanoparticles in the densified reed resulted in a reduced water uptake, which can decrease its bio-deterioration and thus guarantee a longer lifespan when applied as a structural material. The versatility of this innovative treatment can be exploited to improve the mechanical properties of any kind wood-like structure. In conclusion, the nano-toughening densification treatment proposed in this thesis sheds a new insight into the possible enhancements of timber properties.

Finally, in Chapter 5, wood samples were subjected to structural and chemical modifications to create a conductive composite starting from wood. For this purpose, wood specimens were infiltrated with carbon nanotubes. SEM observations confirm that a wide distribution of CNT is achieved, and a continuous and stable network is formed as a result of the underlying cellulose structural substrate. Additional processes were carried out in order to increase the optical transparency of the wood: the samples were infiltrated with transparent polymers so that all the holes in the cellulose structure were filled. The composite material was therefore tested for conductivity, as strain-sensing or damage-sensing applications may be particularly attractive for this type of wood composite. It resulted that the connectivity and the CNT population network is stable even at high flexural loading, since it is stabilized by proper epoxy infiltration. Remarkably, the percolation threshold for CNTs into the conductive wood composite is lower than the current record for CNT+epoxy nanocomposites.

## 7. Other PhD Projects

The two work in Chapter 1 and Chapter 4 are full articles (Status: under review/under submission).

During my PhD I was also involved in other projects, which include:

Silkworm and spider silk. Silk spinning is regarded to be an optimal material fabrication process and researchers are seeking its replication at lab scale. In a continuous quest to improve mechanical properties of natural materials or add new functionalities, they enabled Bombyx Mori to spin spider silk through gene editing or natural silk was both coloured and strengthened through the addition of dyeing molecules and nanoparticles into the diet. I performed experimental trials on silkworms to evaluate the effect of graphene fillers on the mechanical performance of silk within the Silkene ERC PoC. Previous researches have shown the presence of nanoparticles inside the bulk of silk only with indirect or destructive methods. Therefore, my successive research was focussed to find a direct observation of nanoparticles into dragline spider threads. Several spider alimentation methods were tested. Fluorescent markers were embedded into silica nanoparticles to become the carriers of a fluorescence signature, which was still detectable after the silk assembly process. I was involved with the sample design and preparation, optical and raman microscopy analysis, fluorescence analysis including laser scanning confocal microscopy and mechanical tests. SEM and FIB ablation of the silk threads were carried out by collaborators at CNR (Status: project under completion).

Surface properties, such as friction and adhesion, are crucial aspects to develop graphene nanocomposites. These interface properties were studied in situ on graphene oxide (GO) and reduced-GO coatings over polymers and glass fibre substrates. Regarding the experimental activities I was involved in the sample design and preparation for AFM tests and conducted micro-Raman analysis (Status: published [187]).

On a study about frictionless and electrically conductive graphene oxide paper with integrated carbon nanotubes, I performed some minor analysis (Status: submitted).



## 8. Acknowledgements

First and foremost, I would like to thank my supervisors for giving me the opportunity of pursuing this PhD. In particular, Nicola inspired me into undertaking this PhD project and gave me the chance to experiment on a wide variety of topics, pushing me outside my comfort zone while Giorgio shared with me his wide technical knowledge and taught me new experimental techniques along with his invaluable wise support.

Secondly, I would like to deeply thank Fiorella Pantano, Prof. Pegoretti, Georg Pucker and Roberta Springhetti whose support has been of primary importance throughout my PhD. Besides my advisors, I also thank Prof. Bilotti and Prof. Galiotis for their careful revision of my thesis that will drive the future improvement of my scientific work.

I would also like to thank all the people who supported me in my experimental works, teaching me how to use the machineries or helping to build different setups. Namely, in Mesiano: Diego, Flavio and Ludovic. In Povo: Alfredo, Maria Cristina and Stefano but also Marta, Michele, Ruben and Victor.

My office colleagues with whom I share pleasant memories: Eki, Francesca, Hafeez, Luigi, Manoj, Riccardo, Roberto, Simone and Wei. Some other colleagues whom I have worked directly or shared fruitful discussions: Alice, Andrea Gaiardo, Andrea Pedrielli, Andrea Rodella, Antonino, Erica, Evgeny, Gabriele, Lorenzo, Luca, Nadhira, Rafael, Simone and Venet.

During my stay in London I found a great environment with plenty of great people that I want to thank for their high density of interaction even if in a “relatively short stay”. In particular Giovanni, Maurizio and Kening helped me a lot in the initial integration and assisted me in laboratory activities. I also want to mention Adriana, Arnaud, Elinor, Emiliano, Han, Mike, Theo, Ton, Yunyin, Wei.

I also thank the University of Trento and Foundation Bruno Kessler as well as Nanoforce Ltd. and Queen Mary University of London for lab access. I would like to thank the Collegio Bernardo Clesio, its students/alumni (especially those who reached out to me seeking career advice or personal support) and the College Board.

To my enlarged family & friends, words cannot express how grateful I am.

## 9. References

1. Treacy, M. J.; Ebbesen, T.; Gibson, J., Exceptionally high Young's modulus observed for individual carbon nanotubes. **1996**.
2. Lee, C.; Wei, X.; Kysar, J. W.; Hone, J., Measurement of the elastic properties and intrinsic strength of monolayer graphene. *science* **2008**, *321* (5887), 385-388.
3. Geim, A. K.; Novoselov, K. S., The rise of graphene. *Nat Mater* **2007**, *6* (3), 183-191.
4. Stankovich, S.; Dikin, D. A.; Dommett, G. H.; Kohlhaas, K. M.; Zimney, E. J.; Stach, E. A.; Piner, R. D.; Nguyen, S. T.; Ruoff, R. S., Graphene-based composite materials. *Nature* **2006**, *442* (7100), 282-6.
5. Huang, X.; Qi, X.; Boey, F.; Zhang, H., Graphene-based composites. *Chemical Society Reviews* **2012**, *41* (2), 666-686.
6. Kuilla, T.; Bhadra, S.; Yao, D.; Kim, N. H.; Bose, S.; Lee, J. H., Recent advances in graphene based polymer composites. *Progress in Polymer Science* **2010**, *35* (11), 1350-1375.
7. Xiao, X.; Xie, T.; Cheng, Y.-T., Self-healable graphene polymer composites. *Journal of Materials Chemistry* **2010**, *20* (17), 3508-3514.
8. Compton, O. C.; Kim, S.; Pierre, C.; Torkelson, J. M.; Nguyen, S. T., Crumpled graphene nanosheets as highly effective barrier property enhancers. *Advanced materials* **2010**, *22* (42), 4759-4763.
9. Young, R. J.; Kinloch, I. A.; Gong, L.; Novoselov, K. S., The mechanics of graphene nanocomposites: A review. *Composites Science and Technology* **2012**, *72* (12), 1459-1476.
10. Anagnostopoulos, G.; Androulidakis, C.; Koukaras, E. N.; Tsoukleri, G.; Polyzos, I.; Parthenios, J.; Papagelis, K.; Galiotis, C., Stress Transfer Mechanisms at the Submicron Level for Graphene/Polymer Systems. *ACS applied materials & interfaces* **2015**, *7* (7), 4216-4223.
11. Vallés, C.; Abdelkader, A. M.; Young, R. J.; Kinloch, I. A., The effect of flake diameter on the reinforcement of few-layer graphene-PMMA composites. *Composites Science and Technology* **2015**, *111*, 17-22.
12. Gong, L.; Kinloch, I. A.; Young, R. J.; Riaz, I.; Jalil, R.; Novoselov, K. S., Interfacial stress transfer in a graphene monolayer nanocomposite. *Advanced Materials* **2010**, *22* (24), 2694-2697.

13. Ramanathan, T.; Abdala, A.; Stankovich, S.; Dikin, D.; Herrera-Alonso, M.; Piner, R.; Adamson, D.; Schniepp, H.; Chen, X.; Ruoff, R., Functionalized graphene sheets for polymer nanocomposites. *Nature nanotechnology* **2008**, *3* (6), 327-331.
14. Cranford, S. W.; Pugno, N. M.; Buehler, M. J., Silk and Web Synergy: The Merging of Material and Structural Performance. In *Biotechnology of Silk*, Springer: 2014; pp 219-268.
15. Gautieri, A.; Vesentini, S.; Redaelli, A.; Buehler, M. J., Hierarchical structure and nanomechanics of collagen microfibrils from the atomistic scale up. *Nano letters* **2011**, *11* (2), 757-766.
16. Greiner, A.; Wendorff, J. H., Electrospinning: a fascinating method for the preparation of ultrathin fibers. *Angewandte Chemie International Edition* **2007**, *46* (30), 5670-5703.
17. Ko, F.; Gogotsi, Y.; Ali, A.; Naguib, N.; Ye, H.; Yang, G.; Li, C.; Willis, P., Electrospinning of continuous carbon nanotube-filled nanofiber yarns. *Advanced Materials* **2003**, *15* (14), 1161-1165.
18. Tan, E.; Ng, S.; Lim, C., Tensile testing of a single ultrafine polymeric fiber. *Biomaterials* **2005**, *26* (13), 1453-1456.
19. Fennessey, S. F.; Farris, R. J., Fabrication of aligned and molecularly oriented electrospun polyacrylonitrile nanofibers and the mechanical behavior of their twisted yarns. *Polymer* **2004**, *45* (12), 4217-4225.
20. Wang, M.; Jin, H.-J.; Kaplan, D. L.; Rutledge, G. C., Mechanical Properties of Electrospun Silk Fibers. *Macromolecules* **2004**, *37* (18), 6856-6864.
21. Tan, E.; Lim, C., Physical properties of a single polymeric nanofiber. *Applied Physics Letters* **2004**, *84* (9), 1603-1605.
22. Hadimani, R. L.; Bayramol, D. V.; Sion, N.; Shah, T.; Qian, L.; Shi, S.; Siores, E., Continuous production of piezoelectric PVDF fibre for e-textile applications. *Smart Materials and Structures* **2013**, *22* (7), 075017.
23. El Achaby, M.; Arrakhiz, F. Z.; Vaudreuil, S.; Essassi, E. M.; Qaiss, A., Piezoelectric  $\beta$ -polymorph formation and properties enhancement in graphene oxide – PVDF nanocomposite films. *Applied Surface Science* **2012**, *258* (19), 7668-7677.
24. Ataur Rahman, M.; Chung, G.-S., Synthesis of PVDF-graphene nanocomposites and their properties. *Journal of Alloys and Compounds* **2013**, *581*, 724-730.

25. Li, D.; Xia, Y., Direct fabrication of composite and ceramic hollow nanofibers by electrospinning. *Nano Letters* **2004**, 4 (5), 933-938.
26. Li, D.; McCann, J. T.; Xia, Y., Use of electrospinning to directly fabricate hollow nanofibers with functionalized inner and outer surfaces. *Small* **2005**, 1 (1), 83-86.
27. Wang, D.; Li, K.; Teo, W., Preparation and characterization of polyvinylidene fluoride (PVDF) hollow fiber membranes. *Journal of Membrane Science* **1999**, 163 (2), 211-220.
28. Hongu, T.; Takigami, M.; Phillips, G. O., *New millennium fibers*. Elsevier: **2005**.
29. Bunsell, A. R., *Handbook of tensile properties of textile and technical fibres*. Elsevier: **2009**.
30. Paredes, J. I.; Villar-Rodil, S.; Martinez-Alonso, A.; Tascon, J. M., Graphene oxide dispersions in organic solvents. *Langmuir* **2008**, 24 (19), 10560-4.
31. Merlini, C.; Barra, G.; Araujo, T. M.; Pegoretti, A., Electrically pressure sensitive poly (vinylidene fluoride)/polypyrrole electrospun mats. *RSC Advances* **2014**, 4 (30), 15749-15758.
32. Cozza, E. S.; Monticelli, O.; Marsano, E.; Cebe, P., On the electrospinning of PVDF: influence of the experimental conditions on the nanofiber properties. *Polymer International* **2013**, 62 (1), 41-48.
33. Standard ASTM D638-02 Standard Test Methods for Tensile Properties of Plastic. *America Society for Testing and Material, Philadelphia, USA* **2002**.
34. Keten, S.; Buehler, M. J., Nanostructure and molecular mechanics of spider dragline silk protein assemblies. *Journal of the Royal Society Interface* **2010**, 7 (53), 1709-1721.
35. Giesa, T.; Arslan, M.; Pugno, N. M.; Buehler, M. J., Nanoconfinement of spider silk fibrils begets superior strength, extensibility, and toughness. *Nano letters* **2011**, 11 (11), 5038-5046.
36. Shin, M. K.; Lee, B.; Kim, S. H.; Lee, J. A.; Spinks, G. M.; Gambhir, S.; Wallace, G. G.; Kozlov, M. E.; Baughman, R. H.; Kim, S. J., Synergistic toughening of composite fibres by self-alignment of reduced graphene oxide and carbon nanotubes. *Nat Commun* **2012**, 3, 650.
37. J. Brandrup; E. H. Immergut; E. A. Grulke, *Polymer handbook, Fourth Edition*. Wiley New York: **1999**.
38. Kim, G.; Lach, R.; Michler, G.; Pötschke, P.; Albrecht, K., Relationships between phase morphology and deformation

- mechanisms in polymer nanocomposite nanofibres prepared by an electrospinning process. *Nanotechnology* **2006**, *17* (4), 963.
39. Berardo, A.; Pantano, M. F.; Pugno, N. M., Slip knots and unfastening topologies enhance toughness without reducing strength of silk fibroin fibres. *Interface Focus* **2016**, *6* (1), 20150060.
40. Pugno, N. M.; Buehler, M. J., The “Egg of Columbus” for Making the World’s Toughest Fibres. *PloS one* **2014**, *9* (4), e93079.
41. Baniasadi, M.; Huang, J.; Xu, Z.; Moreno, S.; Yang, X.; Chang, J.; Quevedo-Lopez, M. A.; Naraghi, M.; Minary-Jolandan, M., High-Performance Coils and Yarns of Polymeric Piezoelectric Nanofibers. *ACS Applied Materials & Interfaces* **2015**, *7* (9), 5358-5366.
42. Zussman, E.; Rittel, D.; Yarin, A., Failure modes of electrospun nanofibers. *Applied physics letters* **2003**, *82* (22), 3958-3960.
43. Lourie, O.; Cox, D.; Wagner, H., Buckling and collapse of embedded carbon nanotubes. *Physical Review Letters* **1998**, *81* (8), 1638.
44. Liu, L. Q.; Tasis, D.; Prato, M.; Wagner, H. D., Tensile mechanics of electrospun multiwalled nanotube/poly (methyl methacrylate) nanofibers. *Advanced Materials* **2007**, *19* (9), 1228-1233.
45. Mooney, M., A theory of large elastic deformation. *Journal of applied physics* **1940**, *11* (9), 582-592.
46. Gent, A. N., *Engineering with rubber: how to design rubber components*. Carl Hanser Verlag GmbH Co KG: **2012**.
47. Bergstrom, J. S., *Mechanics of solid polymers: theory and computational modeling*. William Andrew: **2015**.
48. Rivlin, R., *Rheology theory and applications*. FR Eirich, ed **1956**.
49. Boyce, M. C.; Arruda, E. M., Constitutive models of rubber elasticity: a review. *Rubber chemistry and technology* **2000**, *73* (3), 504-523.
50. Ogden, R. W., Large deformation isotropic elasticity—on the correlation of theory and experiment for incompressible rubberlike solids. *Proceedings of the Royal Society of London. A. Mathematical and Physical Sciences* **1972**, *326* (1567), 565-584.
51. Coleman, B. D.; Newman, D. C., Rheology of neck formation in the cold drawing of polymeric fibers. *Journal of applied polymer science* **1992**, *45* (6), 997-1004.

52. Coleman, B. D.; Newman, D. C., On the rheology of cold drawing. I. Elastic materials. *Journal of Polymer Science Part B: Polymer Physics* **1988**, 26 (9), 1801-1822.
53. Nova, A.; Keten, S.; Pugno, N. M.; Redaelli, A.; Buehler, M. J., Molecular and nanostructural mechanisms of deformation, strength and toughness of spider silk fibrils. *Nano Letters* **2010**, 10 (7), 2626-2634.
54. Coleman, B. D., Necking and drawing in polymeric fibers under tension. *Archive for Rational Mechanics and Analysis* **1983**, 83 (2), 115-137.
55. Kurtz, S. M.; Pruitt, L.; Jewett, C. W.; Crawford, R. P.; Crane, D. J.; Eddidin, A. A., The yielding, plastic flow, and fracture behavior of ultra-high molecular weight polyethylene used in total joint replacements. *Biomaterials* **1998**, 19 (21), 1989-2003.
56. Nitta, K.-h.; Yamana, M., *Poisson's ratio and mechanical nonlinearity under tensile deformation in crystalline polymers*. INTECH Open Access Publisher ••: **2012**.
57. Asakura, T.; Miller, T., *Biotechnology of silk*. Springer: **2016**.
58. Cranford, S. W.; Tarakanova, A.; Pugno, N. M.; Buehler, M. J., Nonlinear material behaviour of spider silk yields robust webs. *Nature* **2012**, 482 (7383), 72-76.
59. ISO, S., ISO 18188 Specification of polypropylene drinking straws. *International Organization for Standardization, Geneva, Switzerland* **2016**.
60. Zussman, E.; Burman, M.; Yarin, A.; Khalfin, R.; Cohen, Y., Tensile deformation of electrospun nylon-6, 6 nanofibers. *Journal of Polymer Science Part B: Polymer Physics* **2006**, 44 (10), 1482-1489.
61. Eyring, H., The activated complex in chemical reactions. *The Journal of Chemical Physics* **1935**, 3 (2), 107-115.
62. Coleman, B. D., A phenomenological theory of the mechanics of cold drawing. In *Orienting Polymers*, Springer: 1984; pp 76-142.
63. Sedan, D.; Pagnoux, C.; Smith, A.; Chotard, T., Mechanical properties of hemp fibre reinforced cement: Influence of the fibre/matrix interaction. *Journal of the European Ceramic Society* **2008**, 28 (1), 183-192.
64. Elsaid, A.; Dawood, M.; Seracino, R.; Bobko, C., Mechanical properties of kenaf fiber reinforced concrete. *Construction and Building Materials* **2011**, 25 (4), 1991-2001.
65. Joseph, K.; Thomas, S.; Pavithran, C., Effect of chemical treatment on the tensile properties of short sisal fibre-reinforced polyethylene composites. *Polymer* **1996**, 37 (23), 5139-5149.

66. Torres, F.; Cubillas, M., Study of the interfacial properties of natural fibre reinforced polyethylene. *Polymer Testing* **2005**, 24 (6), 694-698.
67. Oksman, K.; Skrifvars, M.; Selin, J.-F., Natural fibres as reinforcement in polylactic acid (PLA) composites. *Composites science and technology* **2003**, 63 (9), 1317-1324.
68. Espert, A.; Vilaplana, F.; Karlsson, S., Comparison of water absorption in natural cellulosic fibres from wood and one-year crops in polypropylene composites and its influence on their mechanical properties. *Composites Part A: Applied science and manufacturing* **2004**, 35 (11), 1267-1276.
69. Ribot, N.; Ahmad, Z.; Mustafa, N., Mechanical Propertise of Kenaf Fiber Composite Using Co-Cured in-Line Fiber Joint. *International Journal of Engineering science and technology* **2011**, 3 (4), 3526-34.
70. Berglund, L. A.; Peijs, T., Cellulose biocomposites—from bulk moldings to nanostructured systems. *MRS bulletin* **2010**, 35 (3), 201-207.
71. Holbery, J.; Houston, D., Natural-fiber-reinforced polymer composites in automotive applications. *Jom* **2006**, 58 (11), 80-86.
72. Reiterer, A.; Lichtenegger, H.; Tschegg, S.; Fratzl, P., Experimental evidence for a mechanical function of the cellulose microfibril angle in wood cell walls. *Philosophical Magazine A* **1999**, 79 (9), 2173-2184.
73. Mittal, N.; Ansari, F.; Gowda, V. K.; Brouzet, C.; Chen, P.; Larsson, P. T.; Roth, S. V.; Lundell, F.; Wågberg, L.; Kotov, N. A., Multiscale Control of Nanocellulose Assembly: Transferring Remarkable Nanoscale Fibril Mechanics to Macroscale Fibers. *ACS nano* **2018**.
74. Baillie, C., *Green composites: polymer composites and the environment*. CRC Press: **2005**.
75. Li, X.; Tabil, L. G.; Panigrahi, S., Chemical treatments of natural fiber for use in natural fiber-reinforced composites: a review. *Journal of Polymers and the Environment* **2007**, 15 (1), 25-33.
76. Mohanty, A. K.; Misra, M.; Drzal, L. T., *Natural fibers, biopolymers, and biocomposites*. CRC press: **2005**.
77. Khalil, H. S. A.; Alwani, M. S.; Omar, A. K. M., Chemical composition, anatomy, lignin distribution, and cell wall structure of Malaysian plant waste fibers. *BioResources* **2007**, 1 (2), 220-232.

78. Ochi, S., Mechanical properties of kenaf fibers and kenaf/PLA composites. *Mechanics of materials* **2008**, 40 (4-5), 446-452.
79. Wambua, P.; Ivens, J.; Verpoest, I., Natural fibres: can they replace glass in fibre reinforced plastics? *composites science and technology* **2003**, 63 (9), 1259-1264.
80. Mahjoub, R.; Yatim, J. M.; Sam, A. R. M.; Hashemi, S. H., Tensile properties of kenaf fiber due to various conditions of chemical fiber surface modifications. *Construction and Building Materials* **2014**, 55, 103-113.
81. Goda, K.; Sreekala, M.; Gomes, A.; Kaji, T.; Ohgi, J., Improvement of plant based natural fibers for toughening green composites—Effect of load application during mercerization of ramie fibers. *Composites Part A: Applied science and manufacturing* **2006**, 37 (12), 2213-2220.
82. Prasad, A. R.; Rao, K. M., Mechanical properties of natural fibre reinforced polyester composites: Jowar, sisal and bamboo. *Materials & Design* **2011**, 32 (8-9), 4658-4663.
83. Gassan, J.; Bledzki, A. K., Possibilities for improving the mechanical properties of jute/epoxy composites by alkali treatment of fibres. *Composites Science and Technology* **1999**, 59 (9), 1303-1309.
84. Satyanarayana, K.; Pai, B.; Sukumaran, K.; Pillai, S., Fabrication and properties of lignocellulosic fiber-incorporated polyester composites. *Hand book of ceramic and composite* **1990**, 1, 339-386.
85. Wegst, U.; Ashby, M., The mechanical efficiency of natural materials. *Philosophical Magazine* **2004**, 84 (21), 2167-2186.
86. Rüggeberg, M.; Burgert, I.; Speck, T., Structural and mechanical design of tissue interfaces in the giant reed *Arundo donax*. *Journal of the Royal Society Interface* **2009**, rsif20090273.
87. Yu, W.; Chung, K.; Chan, S., Column buckling of structural bamboo. *Engineering Structures* **2003**, 25 (6), 755-768.
88. Mahdavi, M.; Clouston, P.; Arwade, S., Development of laminated bamboo lumber: review of processing, performance, and economical considerations. *Journal of Materials in Civil Engineering* **2010**, 23 (7), 1036-1042.
89. Okita, Y.; Saito, T.; Isogai, A., Entire surface oxidation of various cellulose microfibrils by TEMPO-mediated oxidation. *Biomacromolecules* **2010**, 11 (6), 1696-1700.



90. Gao, K.; Shao, Z.; Wu, X.; Wang, X.; Li, J.; Zhang, Y.; Wang, W.; Wang, F., Cellulose nanofibers/reduced graphene oxide flexible transparent conductive paper. *Carbohydrate polymers* **2013**, *97* (1), 243-251.
91. Okahisa, Y.; Yoshida, A.; Miyaguchi, S.; Yano, H., Optically transparent wood–cellulose nanocomposite as a base substrate for flexible organic light-emitting diode displays. *Composites Science and Technology* **2009**, *69* (11-12), 1958-1961.
92. Nogi, M.; Kim, C.; Sugahara, T.; Inui, T.; Takahashi, T.; Sugauma, K., High thermal stability of optical transparency in cellulose nanofiber paper. *Applied Physics Letters* **2013**, *102* (18), 181911.
93. Soykeabkaew, N.; Arimoto, N.; Nishino, T.; Peijs, T., All-cellulose composites by surface selective dissolution of aligned ligno-cellulosic fibres. *Composites Science and Technology* **2008**, *68* (10-11), 2201-2207.
94. Qin, C.; Soykeabkaew, N.; Xiuyuan, N.; Peijs, T., The effect of fibre volume fraction and mercerization on the properties of all-cellulose composites. *Carbohydrate Polymers* **2008**, *71* (3), 458-467.
95. Zhu, H.; Fang, Z.; Preston, C.; Li, Y.; Hu, L., Transparent paper: fabrications, properties, and device applications. *Energy & Environmental Science* **2014**, *7* (1), 269-287.
96. Zhu, H.; Parvinian, S.; Preston, C.; Vaaland, O.; Ruan, Z.; Hu, L., Transparent nanopaper with tailored optical properties. *Nanoscale* **2013**, *5* (9), 3787-3792.
97. Fang, Z.; Zhu, H.; Bao, W.; Preston, C.; Liu, Z.; Dai, J.; Li, Y.; Hu, L., Highly transparent paper with tunable haze for green electronics. *Energy & Environmental Science* **2014**, *7* (10), 3313-3319.
98. Fang, Z.; Zhu, H.; Yuan, Y.; Ha, D.; Zhu, S.; Preston, C.; Chen, Q.; Li, Y.; Han, X.; Lee, S., Novel nanostructured paper with ultrahigh transparency and ultrahigh haze for solar cells. *Nano letters* **2014**, *14* (2), 765-773.
99. Fink, S., Transparent wood—a new approach in the functional study of wood structure. *Holzforschung-International Journal of the Biology, Chemistry, Physics and Technology of Wood* **1992**, *46* (5), 403-408.
100. Andradý, A. L.; Hamid, S.; Hu, X.; Torikai, A., Effects of increased solar ultraviolet radiation on materials. *Journal of Photochemistry and Photobiology B: Biology* **1998**, *46* (1-3), 96-103.

101. Li, Y.; Fu, Q.; Yu, S.; Yan, M.; Berglund, L., Optically transparent wood from a nanoporous cellulosic template: combining functional and structural performance. *Biomacromolecules* **2016**, *17* (4), 1358-1364.
102. Zhu, M.; Song, J.; Li, T.; Gong, A.; Wang, Y.; Dai, J.; Yao, Y.; Luo, W.; Henderson, D.; Hu, L., Highly anisotropic, highly transparent wood composites. *Advanced materials* **2016**, *28* (26), 5181-5187.
103. Zhu, M.; Li, T.; Davis, C. S.; Yao, Y.; Dai, J.; Wang, Y.; AlQatari, F.; Gilman, J. W.; Hu, L., Transparent and haze wood composites for highly efficient broadband light management in solar cells. *Nano Energy* **2016**, *26*, 332-339.
104. Abrahamsen, R.; AS, M. L., Mjøstårnet-18 storey timber building completed.
105. Issa, C. A.; Kmeid, Z., Advanced wood engineering: glulam beams. *Construction and Building Materials* **2005**, *19* (2), 99-106.
106. Sikora, K. S.; McPolin, D. O.; Harte, A. M., Shear strength and durability testing of adhesive bonds in cross-laminated timber. *The Journal of Adhesion* **2016**, *92* (7-9), 758-777.
107. Abrahamsen, R.; AS, M. L. In *Mjøstårnet - 18 storey timber building completed*, Internationales Holzbau-Forum IHF, 2018.
108. Kutnar, A.; Kamke, F. A., Compression of wood under saturated steam, superheated steam, and transient conditions at 150 C, 160 C, and 170 C. *Wood science and technology* **2012**, *46* (1-3), 73-88.
109. Navi, P.; Heger, F., Combined densification and thermo-hydro-mechanical processing of wood. *MRS bulletin* **2004**, *29* (5), 332-336.
110. Pařil, P.; Brabec, M.; Maňák, O.; Rousek, R.; Rademacher, P.; Āermák, P.; Dejmal, A., Comparison of selected physical and mechanical properties of densified beech wood plasticized by ammonia and saturated steam. *European journal of wood and wood products* **2014**, *72* (5), 583-591.
111. Fang, C.-H.; Mariotti, N.; Cloutier, A.; Koubaa, A.; Blanchet, P., Densification of wood veneers by compression combined with heat and steam. *European Journal of Wood and Wood Products* **2012**, *70* (1-3), 155-163.
112. Bekhta, P.; Hiziroglu, S.; Shepelyuk, O., Properties of plywood manufactured from compressed veneer as building material. *Materials & Design* **2009**, *30* (4), 947-953.
113. Laine, K.; Belt, T.; Rautkari, L.; Ramsay, J.; Hill, C. A.; Hughes, M., Measuring the thickness swelling and set-recovery

- of densified and thermally modified Scots pine solid wood. *Journal of materials science* **2013**, *48* (24), 8530-8538.
114. Song, J.; Chen, C.; Zhu, S.; Zhu, M.; Dai, J.; Ray, U.; Li, Y.; Kuang, Y.; Li, Y.; Quispe, N., Processing bulk natural wood into a high-performance structural material. *Nature* **2018**, *554* (7691), 224.
115. Frey, M.; Widner, D.; Segmehl, J. S.; Casdorff, K.; Keplinger, T.; Burgert, I., Delignified and densified cellulose bulk materials with excellent tensile properties for sustainable engineering. *ACS applied materials & interfaces* **2018**, *10* (5), 5030-5037.
116. Salvati, E.; Brandt, L.; Uzun, F.; Zhang, H.; Papadaki, C.; Korsunsky, A., Multiscale Analysis of Bamboo Deformation Mechanisms Following NaOH Treatment Using X-ray and Correlative Microscopy. *Acta Biomaterialia* **2018**.
117. Crielaard, R.; van de Kuilen, J.-W.; Terwel, K.; Ravenshorst, G.; Steenbakkens, P., Self-extinguishment of cross-laminated timber. *Fire Safety Journal* **2019**.
118. Emberley, R.; Putynska, C. G.; Bolanos, A.; Lucherini, A.; Solarte, A.; Soriguer, D.; Gonzalez, M. G.; Humphreys, K.; Hidalgo, J. P.; Maluk, C., Description of small and large-scale cross laminated timber fire tests. *Fire Safety Journal* **2017**, *91*, 327-335.
119. Richardson, B. A., *Wood preservation*. Routledge: **2002**.
120. Rangavar, H.; Taghiyari, H. R.; Abdollahi, A., Effects of nanosilver in improving fire-retarding properties of Borax in solid woods. *International Journal of Bio-Inorganic Hybrid Nanomaterial* **2012**, *1* (3), 159-167.
121. Rassam, G.; Ghofrani, M.; Taghiyari, H. R.; Jamnani, B.; Khajeh, M. A., Mechanical performance and dimensional stability of nano-silver impregnated densified spruce wood. *European Journal of Wood and Wood Products* **2012**, *70* (5), 595-600.
122. Taghiyari, H. R., Study on the effect of nano-silver impregnation on mechanical properties of heat-treated *Populus nigra*. *Wood science and technology* **2011**, *45* (2), 399-404.
123. Taghiyari, H. R.; Bibalan, O. F., Effect of copper nanoparticles on permeability, physical, and mechanical properties of particleboard. *European Journal of Wood and Wood Products* **2013**, *71* (1), 69-77.
124. Li, J.; Zheng, H.; Sun, Q.; Han, S.; Fan, B.; Yao, Q.; Yan, C.; Jin, C., Fabrication of superhydrophobic bamboo timber based on an anatase TiO<sub>2</sub> film for acid rain protection and flame retardancy. *RSC Advances* **2015**, *5* (76), 62265-62272.

125. Li, J.; Sun, Q.; Yao, Q.; Wang, J.; Han, S.; Jin, C., Fabrication of robust superhydrophobic bamboo based on ZnO nanosheet networks with improved water-, UV-, and fire-resistant properties. *Journal of Nanomaterials* **2015**, *2015*, 1.
126. Huo, X.; Yu, A. T., Analytical review of green building development studies. *Journal of Green Building* **2017**, *12* (2), 130-148.
127. Wang, L.; Toppinen, A.; Juslin, H., Use of wood in green building: a study of expert perspectives from the UK. *Journal of cleaner production* **2014**, *65*, 350-361.
128. Kalia, S.; Kaith, B.; Kaur, I., Pretreatments of natural fibers and their application as reinforcing material in polymer composites—a review. *Polymer Engineering & Science* **2009**, *49* (7), 1253-1272.
129. Fridley, K. J., Wood and wood-based materials: Current status and future of a structural material. *Journal of materials in civil engineering* **2002**, *14* (2), 91-96.
130. Fiore, V.; Scalici, T.; Valenza, A., Characterization of a new natural fiber from *Arundo donax* L. as potential reinforcement of polymer composites. *Carbohydrate polymers* **2014**, *106*, 77-83.
131. Simonson, C. J.; Salonvaara, M.; Ojanen, T., The effect of structures on indoor humidity - Possibility to improve comfort and perceived air quality. *Indoor Air* **2002**, *12* (4), 243-251.
132. González-García, S.; Silva, F. J.; Moreira, M. T.; Pascual, R. C.; Lozano, R. G.; Gabarrell, X.; i Pons, J. R.; Feijoo, G., Combined application of LCA and eco-design for the sustainable production of wood boxes for wine bottles storage. *The International Journal of Life Cycle Assessment* **2011**, *16* (3), 224-237.
133. Hillring, B., World trade in forest products and wood fuel. *Biomass and Bioenergy* **2006**, *30* (10), 815-825.
134. Zhu, H.; Xiao, Z.; Liu, D.; Li, Y.; Weadock, N. J.; Fang, Z.; Huang, J.; Hu, L., Biodegradable transparent substrates for flexible organic-light-emitting diodes. *Energy & Environmental Science* **2013**, *6* (7), 2105-2111.
135. Huang, J.; Zhu, H.; Chen, Y.; Preston, C.; Rohrbach, K.; Cumings, J.; Hu, L., Highly transparent and flexible nanopaper transistors. *Acs Nano* **2013**, *7* (3), 2106-2113.
136. Ramage, M. H.; Burrige, H.; Busse-Wicher, M.; Fereday, G.; Reynolds, T.; Shah, D. U.; Wu, G.; Yu, L.; Fleming, P.; Densley-Tingley, D., The wood from the trees: The use of timber in construction. *Renewable and Sustainable Energy Reviews* **2017**, *68*, 333-359.

137. Joseph, P.; Tretsiakova-McNally, S., Sustainable non-metallic building materials. *Sustainability* **2010**, 2 (2), 400-427.
138. Ghavami, K., Bamboo as reinforcement in structural concrete elements. *Cement and concrete composites* **2005**, 27 (6), 637-649.
139. Sharma, B.; Gatóo, A.; Bock, M.; Ramage, M., Engineered bamboo for structural applications. *Construction and Building Materials* **2015**, 81, 66-73.
140. Coffman, G. C. Factors influencing invasion of giant reed (*Arundo donax*) in riparian ecosystems of Mediterranean-type climate regions. University of California, Los Angeles, **2007**.
141. Spatz, H.-C.; Beismann, H.; Brüchert, F.; Emanns, A.; Speck, T., Biomechanics of the giant reed *Arundo donax*. *Philosophical Transactions of the Royal Society of London B: Biological Sciences* **1997**, 352 (1349), 1-10.
142. Perdue, R. E., *Arundo donax*—source of musical reeds and industrial cellulose. *Economic Botany* **1958**, 12 (4), 368-404.
143. Angelini, L. G.; Ceccarini, L.; Bonari, E., Biomass yield and energy balance of giant reed (*Arundo donax* L.) cropped in central Italy as related to different management practices. *European journal of agronomy* **2005**, 22 (4), 375-389.
144. Salvati, E.; Brandt, L. R.; Uzun, F.; Zhang, H.; Papadaki, C.; Korsunsky, A. M., Multiscale analysis of bamboo deformation mechanisms following NaOH treatment using X-ray and correlative microscopy. *Acta Biomaterialia* **2018**, 72, 329-341.
145. Taghiyari, H. R.; Rangavar, H.; Nouri, P., Fire-retarding properties of nanowollastonite in MDF. *European Journal of Wood and Wood Products* **2013**, 71 (5), 573-581.
146. Tjong, S. C., Novel nanoparticle-reinforced metal matrix composites with enhanced mechanical properties. *Advanced engineering materials* **2007**, 9 (8), 639-652.
147. Rodgers, R. M.; Mahfuz, H.; Rangari, V. K.; Chisholm, N.; Jeelani, S., Infusion of SiC nanoparticles into SC-15 epoxy: an investigation of thermal and mechanical response. *Macromolecular Materials and Engineering* **2005**, 290 (5), 423-429.
148. Gao, W., The chemistry of graphene oxide. In *Graphene oxide*, Springer: 2015; pp 61-95.
149. Zhang, X.; Yu, H.; Huang, H.; Liu, Y., Evaluation of biological pretreatment with white rot fungi for the enzymatic hydrolysis of bamboo culms. *International Biodeterioration & Biodegradation* **2007**, 60 (3), 159-164.
150. Hepworth, D.; Vincent, J., Modelling the mechanical properties of xylem tissue from tobacco plants (*Nicotiana*

- tabacum 'Samsun') by considering the importance of molecular and micromechanisms. *Annals of Botany* **1998**, 81 (6), 761-770.
151. Jin, K.; Qin, Z.; Buehler, M. J., Molecular deformation mechanisms of the wood cell wall material. *Journal of the mechanical behavior of biomedical materials* **2015**, 42, 198-206.
152. Meredith, R., Mechanical Properties of Textile Fibres. **1956**.
153. R Core Team, R: A language and environment for statistical computing. <https://www.r-project.org>, **2014**.
154. Hon, D.-S., *Chemical modification of lignocellulosic materials*. Routledge: **2017**.
155. Gargulak, J. D.; Lebo, S. E.; McNally, T. J., Lignin. *Kirk-Othmer encyclopedia of chemical technology* **2001**.
156. Beamson, G.; Briggs, D., High resolution XPS of organic polymers: The Scienta ESCA 300 database. *Surface and Interface Analysis* **1992**, 20 (3), 267-267.
157. Li, Y.; Ruan, R.; Chen, P. L.; Liu, Z.; Pan, X.; Lin, X.; Liu, Y.; Mok, C.; Yang, T., Enzymatic hydrolysis of corn stover pretreated by combined dilute alkaline treatment and homogenization. *Transactions of the ASAE* **2004**, 47 (3), 821.
158. Speck, O.; Spatz, H. C., Damped oscillations of the giant reed *Arundo donax* (Poaceae). *American journal of botany* **2004**, 91 (6), 789-796.
159. Yang, Q.; Fukuzumi, H.; Saito, T.; Isogai, A.; Zhang, L., Transparent cellulose films with high gas barrier properties fabricated from aqueous alkali/urea solutions. *Biomacromolecules* **2011**, 12 (7), 2766-2771.
160. Dixon, P. G.; Gibson, L. J., The structure and mechanics of Moso bamboo material. *Journal of the Royal Society Interface* **2014**, 11 (99), 20140321.
161. Fratzl, P.; Burgert, I.; Gupta, H. S., On the role of interface polymers for the mechanics of natural polymeric composites. *Physical Chemistry Chemical Physics* **2004**, 6 (24), 5575-5579.
162. Fratzl, P.; Burgert, I.; Keckes, J., Mechanical model for the deformation of the wood cell wall: Dedicated to Professor Dr. Dr. hc Franz Jęglitsch on the occasion of his 70th birthday. *Zeitschrift für Metallkunde* **2004**, 95 (7), 579-584.
163. Compton, O. C.; Cranford, S. W.; Putz, K. W.; An, Z.; Brinson, L. C.; Buehler, M. J.; Nguyen, S. T., Tuning the mechanical properties of graphene oxide paper and its associated polymer nanocomposites by controlling cooperative intersheet hydrogen bonding. *ACS nano* **2012**, 6 (3), 2008-2019.
164. Önneby, C.; Pantano, C., Silicon oxycarbide formation on SiC surfaces and at the SiC/SiO<sub>2</sub> interface. *Journal of Vacuum*

*Science & Technology A: Vacuum, Surfaces, and Films* **1997**, 15 (3), 1597-1602.

165. Liu, Y.-T.; Feng, Q.-P.; Xie, X.-M.; Ye, X.-Y., The production of flexible and transparent conductive films of carbon nanotube/graphene networks coordinated by divalent metal (Cu, Ca or Mg) ions. *Carbon* **2011**, 49 (10), 3371-3375.

166. Park, S.; Lee, K.-S.; Bozoklu, G.; Cai, W.; Nguyen, S. T.; Ruoff, R. S., Graphene oxide papers modified by divalent ions—enhancing mechanical properties via chemical cross-linking. *ACS nano* **2008**, 2 (3), 572-578.

167. Pugno, N.; Carpinteri, A., Tubular adhesive joints under axial load. *Journal of applied mechanics* **2003**, 70 (6), 832-839.

168. Gent, A.; Yeoh, O., Failure loads for model adhesive joints subjected to tension, compression or torsion. *Journal of Materials Science* **1982**, 17 (6), 1713-1722.

169. Pugno, N.; Carpinteri, A., Strength, stability and size effects in the brittle behaviour of bonded joints under torsion: theory and experimental assessment. *Fatigue & Fracture of Engineering Materials & Structures* **2002**, 25 (1), 55-62.

170. McAllister, M. J.; Li, J.-L.; Adamson, D. H.; Schniepp, H. C.; Abdala, A. A.; Liu, J.; Herrera-Alonso, M.; Milius, D. L.; Car, R.; Prud'homme, R. K., Single sheet functionalized graphene by oxidation and thermal expansion of graphite. *Chemistry of materials* **2007**, 19 (18), 4396-4404.

171. Shi, Y.; Li, L.-J., Chemically modified graphene: flame retardant or fuel for combustion? *Journal of Materials Chemistry* **2011**, 21 (10), 3277-3279.

172. Pejic, B. M.; Kostic, M. M.; Skundric, P. D.; Praskalo, J. Z., The effects of hemicelluloses and lignin removal on water uptake behavior of hemp fibers. *Bioresource Technology* **2008**, 99 (15), 7152-7159.

173. Zhang, H.; Liu, Y.; Kuwata, M.; Bilotti, E.; Peijs, T., Improved fracture toughness and integrated damage sensing capability by spray coated CNTs on carbon fibre prepreg. *Composites Part A: Applied Science and Manufacturing* **2015**, 70, 102-110.

174. Schoch Jr, K. F.; Panackal, P. A.; Frank, P. P., Real-time measurement of resin shrinkage during cure. *Thermochimica acta* **2004**, 417 (1), 115-118.

175. ASTM, D., 1003-00," Standard Test Method for Haze and Luminous Transmittance of Transparent Plastics. *ASTM International*," *ASTM International*, West Conshohocken, PA **2000**.

176. Kernin, A.; Wan, K.; Liu, Y.; Shi, X.; Kong, J.; Bilotti, E.; Peijs, T.; Zhang, H., The effect of graphene network formation on the electrical, mechanical, and multifunctional properties of graphene/epoxy nanocomposites. *Composites Science and Technology* **2019**, *169*, 224-231.
177. Wichmann, M. H.; Buschhorn, S. T.; Böger, L.; Adelung, R.; Schulte, K., Direction sensitive bending sensors based on multi-wall carbon nanotube/epoxy nanocomposites. *Nanotechnology* **2008**, *19* (47), 475503.
178. Xie, X.-L.; Mai, Y.-W.; Zhou, X.-P., Dispersion and alignment of carbon nanotubes in polymer matrix: a review. *Materials science and engineering: R: Reports* **2005**, *49* (4), 89-112.
179. Sandler, J.; Kirk, J.; Kinloch, I.; Shaffer, M.; Windle, A., Ultra-low electrical percolation threshold in carbon-nanotube-epoxy composites. *Polymer* **2003**, *44* (19), 5893-5899.
180. Bauhofer, W.; Kovacs, J. Z., A review and analysis of electrical percolation in carbon nanotube polymer composites. *Composites Science and Technology* **2009**, *69* (10), 1486-1498.
181. Ma, P. C.; Kim, J.-K.; Tang, B. Z., Effects of silane functionalization on the properties of carbon nanotube/epoxy nanocomposites. *Composites Science and Technology* **2007**, *67* (14), 2965-2972.
182. Spitalsky, Z.; Tasis, D.; Papagelis, K.; Galiotis, C., Carbon nanotube–polymer composites: chemistry, processing, mechanical and electrical properties. *Progress in polymer science* **2010**, *35* (3), 357-401.
183. Sahoo, N. G.; Rana, S.; Cho, J. W.; Li, L.; Chan, S. H., Polymer nanocomposites based on functionalized carbon nanotubes. *Progress in polymer science* **2010**, *35* (7), 837-867.
184. Wang, Z.; Shen, X.; Han, N. M.; Liu, X.; Wu, Y.; Ye, W.; Kim, J.-K., Ultralow electrical percolation in graphene aerogel/epoxy composites. *Chemistry of Materials* **2016**, *28* (18), 6731-6741.
185. Mamunya, Y.; Boudenne, A.; Lebovka, N.; Ibos, L.; Candau, Y.; Lisunova, M., Electrical and thermophysical behaviour of PVC-MWCNT nanocomposites. *Composites Science and Technology* **2008**, *68* (9), 1981-1988.
186. Zhang, H.; Bilotti, E.; Peijs, T., The use of carbon nanotubes for damage sensing and structural health monitoring in laminated composites: a review. *Nanocomposites* **2015**, *1* (4), 167-184.
187. Tripathi, M.; Mahmood, H.; Novel, D.; Iacob, E.; Vanzetti, L.; Bartali, R.; Speranza, G.; Pegoretti, A.; Pugno, N., Nanoscale



friction of graphene oxide over glass-fibre and polystyrene.  
*Composites Part B: Engineering* **2018**, 148, 272-280.









During my PhD activities, I studied the introduction of carbon-based nanofillers in materials at different scales, while focusing primarily on fibres and fibrillar materials. Several production techniques were exploited.

Little is known about the interaction of graphene with electrospun polymeric fibres. Manufacturing composite fibres is complex since fillers have lateral sizes nearing that of the embedding fibre. Indeed, graphene has a direct effect in both the assembly of the electrospun composite fibres and their mechanical performance. Moreover, the tensile behaviour of hollow micrometric electrospun fibres was compared with macroscopic hollow structures such as drinking straws. The acquired insights helped to explain the toughening mechanisms at the micro-scale and develop a model capable of predicting the stress-strain response of such structures.

Among natural materials, wood has the most relevant structural applications even at large scales. Its main structural component is cellulose that has a high resistance and a low light absorption. Several structural modifications of wood derived materials were recently investigated in order to enhance the mechanical and optical properties of cellulose. These enhancements can take place after the internal structure is chemically modified with the removal of lignin and after a structural densification. Potentially, any type of wood-like materials, such as giant reed (that is a fast-growing and invasive species), can be turned into a strong structural composite. Such modifications lead to an open and interconnected internal structure that is the ideal scaffold for nanoparticle intercalation. Graphene oxide and silicon carbide nanoparticles were intercalated into densified reed. They produced an even stiffer, stronger and tougher composite compared to the best up-to-date process available. Moreover, its capabilities to resist fire and water-absorption were tested.

Finally, the previous process was further developed on wood to achieve a combination of improved transparency and electrical conductivity. Graphene and carbon nanotubes were introduced into the structure of wood to foster conductivity and explore the viability of its application as a self-strain sensor.

**David Novel** received M.S. in Materials Engineering in 2015. PhD researcher in the Department of Civil, Environmental and Mechanical Engineering at the University of Trento and in Fondazione Bruno Kessler (Italy). Member of the Board of Directors for the Collegio Bernardo Clesio. Worked as a teaching assistant for the solid and structural mechanics group. Research focuses on fibres, nanomaterials and wood-like materials. Studies comprise a wide variety of applications ranging from production and testing of micro/nanofibres to graphene-based nanocomposites and biological materials, such as silkworm and spider silk. During his PhD visited Nanoforce Ltd. at Queen Mary University of London to carry out a research activity regarding wood transparency and wood conductivity.